INVESTIGATION OF HEAT TRANSFER
THROUGH POROUS MEDIA

by

Ihor Stephan Diakunchak

Thesis submitted in partial fulfillment
of the requirements for the degree of
Master of Engineering
in
Mechanical Engineering

Department of Mechanical Engineering
McGill University
Montreal

August 1961

TABLE OF CONTENTS

	Page
TABLE OF CONTENTS	i
ACKNOWLEDGEMENTS	ii
LIST OF ILLUSTRATIONS	iii
LIST OF SYMBOLS	vii
SUMMARY	1
INTRODUCTION	2
REVIEW OF PREVIOUS WORK	9
THEORETICAL CONSIDERATIONS	20
DESCRIPTION OF APPARATUS	35
EXPERIMENTAL PROCEDURE	39
DISCUSSION OF EXPERIMENTAL RESULTS	41
CONCLUSIONS	50
BIBLIOGRAPHY	51
APPENDICES	57
ILLUSTRATIONS	I

ACKNOWLEDGEMENTS

The author wishes to express his gratitude to Professor J. Stachiewicz for his advice and assistance and to Professor J. Swithenbank and Mr. J. Gravel for their helpful suggestions.

The use of Canadian Pratt and Whitney Aircraft Company electronic computer is greatly appreciated.

The financial assistance provided by the National Research Council and the Defence Research Board is gratefully acknowledged.

Thanks is extended to Miss D. Watamaniuk for typing this thesis.

LIST OF ILLUSTRATIONS

		Page
Figure 1	Kinetic Heating Effect.	I
Figure 2	Comparison of Cooling Methods in Cooling Combustion Chamber Liner.	II
Figure 3	Temperature Distribution in a Transpiration Cooled Wall.	III
Figure 4	Boundary Layer on a Transpiration Cooled Porous Wall.	IV
Figure 5	Schematic Diagram of Heat Transfer Rig.	V
Figure 6	Heat Transfer Rig.	VI
Figure 7	Propane Line.	VII
Figure 8	Burner Nozzle.	VIII
Figure 9	Combustion Chamber	IX
Figure 10	Cross-Section of Test Duct	X
Figure 11	Porous Wall	XI
Figure 12	Shielded Thermocouple Probe	XII
Figure 13	Pitot-Thermocouple Probe.	XIII
Figure 14	Instrument Pannel.	XIV
Figure 15	Side View of Test Duct.	XV
Figure 16	Instruments Used with Ardonox.	XVI
Figure 17	Cross-Section of Bellmouth and Settling Chamber of Pressure Drop Rig.	XVII
Figure 18	Porous Bronze Plug Surface. f = 22.4%	XVIII
Figure 19	Porous Bronze Plug Surface. f = 25.3%	XIX
Figure 20	Porous Bronze Plug Surface. f = 30.9%	XX

		Page
Figure 21	Porous Bronze Plug Surface. f = 36.9%	XXI
Figure 22	Porous Bronze Plug Surface. f = 40.8%	XXII
Figure 23	Porous Bronze Plug Surface. f = 46.6%	XXIII
Figure 24	Internal Heat Transfer Correlation for Porous Bronze.	XXIV
Figure 25	Temperature Distribution in Porous Wall. Run No. 21	XXV
Figure 26	Calculated Temperature Distribution in Porous Wall. Run No. 10	XXVI
Figure 27	Calculated Temperature Distribution in Porous Wall. Run No. 23	XXVII
Figure 28	Calculated Temperature Distribution in Porous Wall. Run No. 38	XXVIII
Figure 29	Cooling Efficiency.	XXIX
Figure 30	Cooling Efficiency.	XXX
Figure 31	Combined Thermal Conductivity.	XXXI
Figure 32	Combined Thermal Conductivity.	XXXII
Figure 33	Heat Transfer Coefficient.	XXXIII
Figure 34	Non-Dimensional Boundary Layer Thickness vs. Non-Dimensional Length in Direction of Flow.	XXXIV
Figure 35	Non-Dimensional Boundary Layer Thickness vs. Non-Dimensional Length in Direction of Flow.	XXXV
Figure 36	Velocity Profiles Against $\frac{v_0 y}{\nu_1}$ at Different Location Along the Plate.	XXXVI
Figure 37	Velocity Profiles vs. $\frac{y u}{\nu_1}$ for Different Mach Numbers.	XXXVII

		Page
Figure 38	Temperature Profiles vs. $\frac{yu}{y_1}$ for Various Injection Rates.	XXXVIII
Figure 39	Velocity Profiles vs. $\frac{yu}{y_1}$ for Different Mach Numbers.	XXXIX
Figure 40	Theoretical Laminar-Boundary-Layer Profiles with Suction and Blowing.	XXXX
Figure 41	Cooling Efficiency Against $\left(\frac{\rho_0 v_0}{\rho_1 u_1}\right)^2 R_e$	XXXXI
Figure 42	Velocity Profile. Run No. 10	XXXXII
Figure 43	Velocity Profile. Run No. 19	XXXXIII
Figure 44	Velocity Profile. Run No. 39	XXXXIV
Figure 45	Velocity Profile. Run No. 3	XXXXV
Figure 46	Velocity Profile. Run No. 5 & 59	XXXXVI
Figure 47	Velocity Profile. Run No. 13	XXXXVII
Figure 48	Velocity Profile. Run No. 20	XXXXVIII
Figure 49	Velocity Profile. Run No. 23	XXXXIX
Figure 50	Velocity Profile. Run No. 29	L
Figure 51	Velocity Profile. Run No. 31	LI
Figure 52	Velocity Profile. Run No. 44	LII
Figure 53	Velocity Profile. Run No. 46	LIII
Figure 54	Velocity Profile. Run No. 50	LIV

		Page
Figure 55	Temperature Profile. Run No. 3	LV
Figure 56	Temperature Profile. Run No. 13	LVI
Figure 57	Temperature Profile. Run No. 23	LVII
Figure 58	Temperature Profile. Run No. 27	LVIII
Figure 59	Temperature Profile. Run No. 29	LIX
Figure 60	Temperature Profile. Run No. 31	LX
Figure 61	Temperature Profile. Run No. 46	LXI
Figure 62	Temperature Profile. Run No. 47	LXII
Figure 63	Temperature Profile. Run No. 50	LXIII
Figure 64	Pressure Drop Against Mass Flow. f = 22.4%	LXIV
Figure 65	Pressure Drop Against Mass Flow. f = 25.3%	LXV
Figure 66	Pressure Drop Against Mass Flow. f = 30.9%	LXVI
Figure 67	Pressure Drop Against Mass Flow. f = 36.9%	LXVII
Figure 68	Pressure Drop Against Mass Flow. f = 40.8 %	LXVIII

LIST OF SYMBOLS

A	- area.	ft.^{2}
C_p	- specific heat at constant pressure.	Btu/lb. °F
D, d	- diameter.	ft.
f	- porosity.	
G_c	- coolant mass flow per unit area.	lb./hr.ft.^{2}
h	- film heat transfer coefficient.	Btu/hr.ft.^{2} °F
h_c	- calculated film heat transfer coefficient.	Btu/hr.ft.^{2} °F
h'	- internal heat transfer coefficient per unit volume.	Btu/hr.ft.^{2} °F/ft.^{3}
k	- fluid conductivity.	Btu/hr.ft. °F
k_s	- solid conductivity.	Btu/hr.ft. °F
k_m	- combined conductivity.	Btu/hr.ft. °F
l	- length.	ft.
m	- hydraulic radius.	ft.
M	- Mach Number.	
N_u'	- Nusselt Number based on h'.	
N_{ux}	- Nusselt Number based on distance along plate.	
p	- pressrure.	lb./ft.^{2}
Q	- volumetric flow.	ft.^{3}/hr.
R_e	- Reynolds Number based on diameter.	
R_{ex}	- Reynolds Number based on distance along plate.	
S	- wetted surface.	ft.^{2}/ft.^{3}
T, t	- temperature.	°R
T_c	- coolant inlet temperature.	°R
T_s	- coolant temperature at hot surface.	°R

T_1	- main stream temperature.	°R
t_o	- coolant side porous wall surface temperature.	°R
t_s	- hot surface temperature.	°R
u	- velocity, parallel to wall.	ft/sec.
U_1	- main stream velocity.	ft/sec.
v	- velocity, perpendicular to wall.	ft/sec.
v_o	- coolant injection velocity.	ft/sec.
V	- volume.	ft^3
w	- coolant mass flow.	lb/hr.
x	- distance.	ft.
y	- distance.	ft.
z	- distance.	ft.
γ	- ratio of specific heats.	
δ	- boundary layer thickness.	ft.
ρ	- density.	lb/ft^3
μ	- dynamic viscosity.	lb/sec. ft.

SUMMARY

The effect of cold air injection on the heat transfer through a porous bronze wall and the turbulent boundary layer in subsonic flow has been investigated experimentally.

The air was injected through a wall of 41.4 per cent porosity at varying rates into the main stream, whose temperature varied from 580 to 1000 $^{\circ}R$ and whose velocity ranged from 60 to 110ft./sec. The internal heat transfer coefficient per unit volume of porous wall, and the combined thermal conductivity of the matrix and the coolant were determined. The film heat transfer coefficient through turbulent boundary layer with coolant injection was calculated. A qualitative analysis of the boundary-layer temperature and velocity profiles was made.

An investigation of the pressure drop through porous bronze plugs was made.

INTRODUCTION

An effective method of cooling materials subjected to high temperatures is required. Transpiration cooling, which is cooling by forcing a fluid through a porous wall in a direction opposite to that of the heat flow, is best suited for cooling blades and casings in gas turbines, combustion chamber liners, rocket motors and nozzles, and skin of rockets and supersonic airplanes. A thorough knowledge and understanding of the mechanism of heat and mass transfer through porous media is required for the successful application of transpiration cooling, for the extraction of heat from nuclear reactors composed of a porous matrix made up of a mixture of uranium and a moderator, and for other similar processes.

Although substantial increases in power and economy of most types of propulsion engines can be achieved by the improvements in the flow capacity and the efficiency, the largest and most significant benefits may be obtained by increasing the temperature up to 4000°R; however, present materials have insufficient strength at these higher temperatures to withstand the strains imposed. New "exotic" fuels will increase the operating temperatures. Application of transpiration cooling will make possible operation of propulsion engines at much higher temperatures and thus result in enhanced performance.

Capacity of nuclear reactors is limited by the rate of heat extraction. Should the reactor become supercritical, the increased heat production will cause the melting of uranium rods, aluminum sheathing, and the coolant coils. A porous matrix of uranium and a moderator offers an immense heat transfer area. A coolant forced through the matrix will pick up the heat produced by nuclear fission much more efficiently than the present methods.

When an object travels at speeds greater than $M = 1$, the air in the shock wave that precedes the object becomes partially dissociated and ionized. The shock layer, which is the region between the shock front and the surface boundary layer, radiates heat to the surface. In addition to heat transfer to the surface by forced convection and radiation, in partially dissociated gas the surface is heated by direct transfer of Kinetic Energy as well as by transfer of Potential Energy, which is converted to Kinetic Energy by secondary collision at the surface. At hypersonic speed the heat transferred to the surface may be sufficient to cause evaporation, sublimation, oxidation, sputtering, secondary electron emission, or other deleterious surface effects.

Assuming isentropic compression, wall temperature resulting from kinetic heating is given by:

$$T = \left[1 - \left(\frac{\gamma - 1}{2}\right) M^2 \right] T_{amb}$$

where γ = ratio of specific heats

T_{amb} = Ambient temperature

For non-isentropic condition, the above temperature will not be achieved. The equilibrium temperature that would exist in an ideal insulated surface having zero radiative heat exchange is given by:

$$T = \left[1 - r \left(\frac{\gamma - 1}{2}\right) M^2 \right] T_{amb}$$

r = temperature recovery factor

= .85 in laminar boundary layer

= .88 to .9 in turbulent region

(these values are for air only)

Figure 1 shows effect of Mach Number, altitude, and surface emissivity on the surface temperature.

To make hypersonic flight possible, methods to cool and protect aircraft and rocket surfaces must be perfected. There are many possible solutions to the problem of kinetic heating. The missile itself may have sufficiently high heat capacity to absorb the heat. The object may move more slowly at low altitude, where the heat transfer rate is large because of the higher atmospheric density. The skin of missiles and aircraft can be made of materials with very high emissivity to radiate away the heat. The skin may be insulated to reduce heat transfer to the structural members and delay high temperatures in transient heating. The insulation can be accomplished by coating the surface with a thin layer of aluminum oxide. The skin can be constructed of a non-structural high melting outer shell with high emissivity on the outside and low emissivity on the inside. Insulation and a radiation shield is then placed between the outer shell and the inside load-carrying skin. Cooling is achieved by having part of the surface melt. The surface may be cooled by circulating a coolant close to the surface. And finally the kinetic heating restriction on hypersonic flight may be removed by transpiration cooling.

To eliminate the effects of kinetic heating transpiration cooling is the best of the direct cooling methods (see fig. 2). The mechanism by which transpiration cooling works is as follows. A fluid is forced through a porous material in a direction opposite to the heat flow. As the coolant passes through the matrix, it picks up the heat from the wall and lowers its temperature. This heat transfer is very effective because of the very large surface area available in the porous medium. The coolant emerges at the exposed surface in small streams from the numerous pores in the material. If the pores are very small, the streams will coalesce almost immediately on leaving the surface. Thus a continuous coolant stream flows from the surface in a direction opposite to the heat flow from the main stream. The heat transfer to the surface is mainly by conduction through the coolant layer. If this coolant film remains continuous for even a small distance from the surface, almost no heat will be conducted to it. This is particularly true if air is used as a coolant because of its low thermal conductivity.

The injection of the coolant in a direction at right angles to the main stream has two effects: 1) it energises the boundary layer and thickens it, thus decreasing the velocity and temperature gradients; 2) it absorbs the heat which would otherwise be conducted to the wall. The first effect applies to a case where the main flow is such as to create a substantially laminar boundary layer near the surface. The boundary layer thickening by injecting the coolant will result in a decreased heat transfer to the surface. The second effect applies to the region very close to the wall and is not affected by the flow conditions of the main stream to any great extent.

Cooling a surface by blowing a fluid through it requires a porous skin to which the coolant may be led through channels. The porous skin can be made of sintered stainless steel, Stellite, Nimonic, Mowel, bronze, Inconel, Haymes Alloy 5, and other heat resistant metals. Almost any metal, which lends itself to breaking down into a fine powder, can be used. The powdered metal is put in a die, compressed, and sintered at a temperature slightly below the melting point. Grain growth and bonding occur where the particles are sufficiently close together, but a network of fine channels is left throughout the matrix. The size and distribution of these passages, expressed as the permeability of the matrix to the flow of fluids, is controlled by the size of the powder grains and the pressure applied in compacting. Permeability can also be controlled by introducing into the matrix low-melting-point metal wires, which are evaporated out during sintering, and by mixing with the metal powder non-metallic volatile filler, such as ammonium carbonate, which gasifies during sintering and results in passages, which connect the initial voids. The variation in permeability of the matrix gives the desired rate of effusion of the coolant at the surface to take care of the variation in the surface heat protection required. To obtain the best cooling efficiency, the size and distribution of the apertures at the surface should be such that the coolant emerges from the surface to form a continuous insulating layer at the surface, and not as a series of discrete jets which mix with the hot gases resulting in the loss of the insulating effect. The openings of the pores should be divergent outwards. A coating, which will melt at some predetermined temperature, can be applied to the surface of the porous material. Thus the cooling will start only after this temperature is reached. Although the strength and fatigue properties of porous media are not reduced by the porous structure as much as it may appear at first, for high stress application the skin can be bonded to solid load-carrying members.

Another method for making porous walls is by bonding several layers of woven metal gauze. The permeability of such a structure may be reduced by cold rolling. The permeability is controlled by a suitable choice of the mesh size and wire diameter of the individual layers. This type of porous wall has a superior strength to that of a sintered porous wall. Porous walls can also be made by mechanical perforation of a solid sheet and by electrodeposition. Metal and glass fibres as well as ceramics may also be used.

Many coolants may be used for transpiration cooling. Air is cheap and has a very low coefficient of thermal conductivity. The skin friction and heat transfer can be reduced considerably with the injection of only about 20 per cent as much hydrogen or about 40 per cent as much helium as the injection of air (see ref. 29). Liquid coolants have one advantage, which is the absorption of the latent heat of evaporation. Water is very effective in absorbing radiation.

Porous media clog very easily. Thus impurities in the coolant down to diameters of a few microns must be filtered out. The coolant flow may also be restricted by formation of oxides and the adsorption of the coolant molecules to the wall passages. A knowledge of the mechanics of flow of fluids through porous media is necessary to design a proper transpiration cooling system.

Since transpiration cooling has so many important applications, a study of the heat transfer through porous media was undertaken. There is an urgent need for experimental investigation of details of the actual boundary layer subjected to homogenous injection. As originally conceived, this investigation was to deal primarily with cooling at hypersonic speeds. But, limitations in the air supply and its pressure and maximum temperature available, made experimental investigations possible only for low speed and temperature. Because of the cost and availability in Canada, porous bronze was used.

In this investigation the injection velocity distribution will be varied as the inverse of the square root of the distance along the plate, in order to keep the hot surface temperature constant, and the boundary-layer thickness at the leading edge of the porous plate will be made zero by boundary-layer suction. To obtain a range of conditions the coolant flow, main-stream flow and main-stream temperature, and the position along the plate will be varied. The coolant wall temperatures on the hot and the cold side of the porous wall and the coolant mass flow will be substituted into the solution to the equation of heat transfer through porous wall to calculate the temperature distribution inside the wall and the internal heat transfer coefficient of the porous wall. The calculation of the overall thermal conductivity is to be made from the coolant and wall temperatures and the coolant mass flow. Traverses of the boundary-layer velocity and temperature profiles for the transpiration cooled plate will be made to see the effect of injection of coolant into a hot stream. From the main-stream temperature, hot surface temperature, coolant mass flow, and the coolant temperature drop, the hot side film heat transfer coefficient will be determined.

The pressure drop through porous bronze plugs of different porosities will be investigated to see if the results can be correlated with the existing equations for the flow of fluids through porous media.

REVIEW OF PREVIOUS WORK

In 1929 Oberth (see ref. 29) was the first to propose transpiration cooling for the cooling of rocket engines. The first experimental work in this field was carried out by Goddard (see ref. 29) in 1930. He burned a mixture of gasoline and oxygen in a 4 inch diameter rocket motor fitted with a porous ceramic liner and throat. Oxygen was used as the coolant. Although the experiment lasted only 11 seconds, the feasability of transpiration cooling was clearly demonstrated.

Jakob and Fieldhouse (see ref. 36) experimented with water and nitrogen as coolants. The hot air was discharged from a chamber through a nozzle in a 2 inch wide, $\frac{1}{2}$ inch thick, and 10 inch long, well-insulated Transite (asbestos fabricate) channel, in the wall of which a porous brass (70% C_u-30% Z_n) disk, 1 inch in diameter and $\frac{1}{2}$ inch thick, was imbedded. Experiments with water were also made with a solid copper disk in place of the porous plug. The water was circulated to the cold side of the solid disk in order to cool it. This was done to compare transpiration cooling with the direct cooling method. The test conditions were such that the boundary layer of the hot air on the test disk was in the turbulent range. The maximum main stream velocity was 600 ft./sec., and the maximum temperature was 692 °F. The tests showed that h, the coefficient of heat transfer at the exposed surface, increased with the main stream velocity and decreased with main stream temperature with both the solid and the porous plates. The time rate of the heat transferred from the hot gas by convection, the coefficient h of convective heat exchange, and the mass flow of water per unit time, were much larger for the solid plate than for the porous plate if the exposed surface was to kept at the same temperature, although inlet water temperature for the solid disk tests was lower. Much more water was required to keep the porous plate surface temperature slightly below water saturation temperature than to keep it slightly above the saturation temperature. This illustrated the added cooling effect provided by extraction of heat equal to the latent heat of evaporation of water. The coefficient h was almost imdependent of the coolant used, provided that the surface temperature was the same. The mass flows of the different coolants were quite different for the same h. Jakob (see ref. 36) also proved by a theoretical derivation that heat transferred from the hot gas by convection is independent of the kind of coolant used. The experiment showed that the weight of nitrogen needed to obtain the same surface temperature was five times that of water, and that of evaporating water about 1/40 that of water kept below the saturation temperature.

Duncombe (see ref. 15) investigated sweat cooling using a bronze filter as the porous medium and air as the coolant. The porous bronze was in form of a cylinder with I.D. = 4 inches and O.D. = $4\frac{1}{2}$ inches. Its porosity was 40 per cent and pore size was 0.001 to 0.002 inch. The test section was composed of 1 19/32 inch long upstream plain section, 6 3/16 inch long middle porous section, and 3 19/32 long downstream plain section. The maximum gas temperature was 932°F, main-stream mass velocity was 0.316 lb/sec/in^2, coolant mass velocity was 0.002 lb/sec/in^2, and the pressure was atmospheric. The hot gas from the combustion chamber was passed through an accelerator and then through the porous cylinder, which was surrounded by a larger cylinder with compressed cooling air. The tests were conducted for three different main air flows, three fuel flows, and a range of coolant flows. The temperature of the sweat cooled surface was found to be dependent on, and itself had, an effect on, the temperature of the adjacent non-porous sections. Correlation with theory was found to be best for points on the porous cylinder furthest downstream. The prediction of relation between the coolant flow and the temperature drop on basis of fully developed turbulent pipe flow was found to be reliable for distances two or three diameters downstream. Before this downstream distance was reached, the coolant flow required for a given temperature drop fell off from a large value at the beginning of the porous section. The coolant flow required rose to five times the fully developed turbulent pipe flow requirements after a non-porous length of 0.91 diameters, which followed the porous section.

Grootenhuis et al (see ref. 30) forced cooling air through Porosint (bronze) disks of five different porosities. Before entering the porous medium, the coolant passed through a water-cooled pipe to prevent the heating up of the apparatus. The porous specimen was fitted in a wall and a source of radiant heat was directed at it. A shield around the outlet face of the specimen and heater prevented the outside air currents from disturbing the flow of air near the specimen. The temperature measurements with a number of thermocouples at various radii on the specimen indicated that at low heat inputs no radial heat flow occurred and only at the highest values of heat input was there a slight outward radial flow of heat. This heat flow diminished as soon as the coolant was introduced. The surface temperature did not exceed 392°F because of severe oxidation of the porous surface at higher temperatures, which altered the conductivity of the material. The correlation of results obtained in these tests with previously obtained results was unsatisfactory, probably due to the deformation of the spherical particles which caused a loss of effective internal surface area.

Investigation of transpiration cooling for a turbulent boundary layer in subsonic flow using air as the coolant was conducted by Brunk (see ref. 6). The main stream air emptied from a large plenum chamber into a 4 inch wide by 10 inch high continuous-flow wind tunnel. One of the vertical walls was made of $\frac{1}{2}$ inch thick porous bronze plate, the inside face of which had an average surface roughness of 0.0005 inch and an emissivity of 54 ± 5 per cent up to 350°F. The coolant was introduced to the test section by a series of coolant ducts. The width of individual ducts was designed so that the coolant could be injected to give a constant wall temperature. The amount of air flowing from the coolant manifold into each duct was controlled by an electrically operated butterfly valve. To insure uniform flow of coolant two screens were installed in each duct, one at the entrance and the other at the end of the diffusing section. There was a knife-edge contact between the edges of the ducts and the porous plate to prevent air leakage from one duct to another. The coolant temperatures were -15 to -5°F, while the main-stream stagnation temperature was 215°F. In order to control the size of the boundary layer on the test wall at the upstream edge of the porous plate, a boundary-layer-bleed system was installed immediately upstream of the test specimen. Just upstream of the porous wall, a slit, which was covered by a Lektromesh screen, in the test wall was connected by a duct to a suction pump. These tests showed that the boundary-layer thickness at the upstream edge of the plate was 0.4 inches without suction and 0.01 inch with maximum suction. For maximum suction it was assumed that the boundary layer had zero thickness at the beginning of the porous plate. Orifices on the wall opposite the porous plate gave the static pressure distribution along the tunnel. The temperatures on each side of the porous plate were measured by thermocouples imbedded in small grooves on the surface of the plate. The grooves were vertical and the thermocouple wires were led for some distance along the groove to reduce errors due to conduction on the plate surface. The leads on the thermocouples mounted on the stream side of the porous plate were passed through a small hole drilled in the end of the groove and led directly away from the coolant side of the plate.

Brunk made two types of tests: 1) the temperature along the stream side of the porous plate was kept constant, and; 2) the amount of coolant mass injected per unit area along the porous plate was kept constant. The main stream Mach Number ranged from 0.53 to 0.65. With the wall temperature kept constant runs were made with no boundary-layer bleed, and with maximum boundary-layer bleed. Contrary to theoretical predictions, the coolant flow increased slightly downstream. This was due to the variation in the permeability of the porous plate covering a single duct. In the runs with constant coolant mass flow per unit area, the mass-flow rate was actually not constant.

Although the curves for constant length Reynolds Numbers agreed qualitatively with theoretical curves, there was no quantitative agreement, since the theory was based on the assumptions of constant mainstream velocity and a varying mass-flow rate to result in a constant temperature along the test specimen. The above requirements were not met in the experiments conducted by Brunk. The constant-area channel had a favorable pressure gradient, resulting in a velocity increase at the downstream stations. Also, it was impossible to obtain the correct variation of the coolant flow for a constant wall temperature. The porous plate used in these tests became plugged with dirt and the permeability of the plate varied. Thus the effectiveness of porous bronze as a material for transpiration cooling depended greatly on the lack of dirt in the coolant. By injecting the coolant through a series of ducts it was possible to vary the temperature along the wall. The injection of the coolant had a large effect on the temperature of the hot surface of the porous wall. The results demonstrated a correlation between the wall temperature and local coolant-flow rate. For the majority of the runs, the correlation was the same for runs with constant wall temperature and constant coolant mass flow.

Duwez and Wheeler (see ref. 16) experimented with a cylindrical porous duct 1 inch in diameter and $1\frac{1}{2}$ inches long. The test specimen was clamped between two sections of a stainless-steel holder, and thermally insulated from the holder by Transite gaskets. The coolant was forced through the walls of the test specimen from a small annular space between the holder and the specimen. Heat was supplied by: 1) oxyhydrogen flame with a maximum temperature of 4200°F and a maximum velocity of 300ft/sec.; 2) gasoline-air flame with a maximum temperature of 2000°F and a Mach Number of unity. With the oxyhydrogen flame as the source of heat, the specimen surface temperature was recorded as a function of coolant mass flow. Using water as the coolant, there was a critical mass flow, above which the specimen surface temperature stayed close to the boiling point of water, and below which the surface temperature increased rapidly with decreasing flow. With a gas as the coolant, the graph of surface temperature against the coolant flow is continuous, because the coolant does not experience a change of phase. The quantity of the gas required to achieve a given surface temperature was dependent on the nature of the coolant. The flow rate of Nitrogen was found to be five times that of Hydrogen. The nature of porous material had some effect on sweat cooling. With the same main-stream temperature and the same coolant flow, the surface temperature of porous copper was several hundred degrees Fahrenheit higher than that of nickel or stainless steel. In the gasoline-air burner tests the specimen surface temperature was measured as a function of coolant mass flow, for different main stream velocities and temperatures. The higher the main stream temperature and velocity the higher coolant mass flow was required to keep the surface temperature constant.

Libby, Kaufman, and Harrington (see ref. 42) conducted an experimental investigation to obtain data on the characteristics of the isothermal laminar boundary layer on a porous flat plate subjected to injection of the same fluid as that of the main stream, and to compare these characteristics with the predictions of the laminar boundary layer theory. The test duct was a 30 inch by 2 inch channel, with a porous bronze plate, 3/4 inch thick, 14 inches wide, and 60 inches long, mounted flush with the inner surface along the centerline of one of the vertical walls immediately downstream of the inlet bell. On the coolant side the test specimen was attached to an injection air bell, which was connected to a supercharger. By changing the connections to the supercharger inlet and exhaust, either suction or injection through the porous wall could be applied. A hot wire anemometer was used to make the velocity measurements. Suction stabilized the boundary layer, while injection reduced its stability and caused earlier transition. The results agreed with Yuan's theory (see ref. 69). Following conclusions were drawn from the experiment: 1) Porous plates, which provided continuous normal velocities at the wall, could be realized. The microstructure of such a plate was complex and the pressure drop was proportional to the velocity at low flow rates; 2) Regions of laminar flow with injections could exist despite the inherent roughness and the finite number of pores in real porous plates. The laminar boundary-layer stability theory predicted qualitatively the effect of suction and injection on the transition Reynolds Number; 3) The isothermal laminar boundary layer on a flat plate could be stabilized to a indefinitely high Reynolds Number if suction corresponding to $(-\frac{v_o}{U_1}) = 10^{-4}$ was applied (v_o = coolant injection velocity, U_1 = main-stream velocity). This was in good agreement with the predictions of laminar boundary-layer stability theory of Libby, Lew, and Romano (see ref. 72); 4) The laminar boundary-layer stability analysis of Yuan (see ref. 67) for flow over a partially porous flat plate could be verified experimentally. The heat-transfer data of Yuan (see ref. 67) was verified at low heat transfer rates.

Mickley, Ross, Squyers, and Stewart (see ref. 46) conducted an experimental and theoretical study of the effect on the boundary layer of sucking or blowing air through a porous wall into or out of a main air stream flowing parallel to the test wall. They used the laminar-boundary-layer theory to calculate velocity, temperature, and concentration profiles as well as the friction, heat, and mass transfer rate for the laminar flow with the mass transfer rate varying as $1/\sqrt{x}$ (x = axial distance from the leading edge of the porous specimen). They expanded the turbulent flow film theory to provide a prediction of the effect of mass transfer on the friction, heat, and mass transfer coefficients. For the experiments the test duct, 9 inches long, 13.5 inches wide, and 144 inches long, was supplied with air through a convergent nozzle. Immediately upstream of the test section, suction pannels in the walls removed the initial boundary layer to give the effect of a sharp leading edge. Small suction pannels in the bottom wall also prevented the buildup of undesirable boundary layers. The width of the test section converged to 12 inches at the exit. The bottom wall was made flexible and mounted on a ladderlike support manipulated by four screw jacks. This modification was made to provide a uniform velocity along the lengh of the tunnel. The test section was made of 80-mesh Jelliff Lektromesh screen 0.004 inch thick. A provision was made for direct observation of the boundary-layer density profiles by means of a Mach-Zehnder interferometer through two windows. The space behind the test wall was divided into 15 compartments, to provide a control of mass transfer distribution and energy input. A woven Nichrome heating element was mounted immediately behind the test wall and insulated from it by a Fiberglass sheet. A second heating element was mounted 2 inches behind the wall. To minimize radiation, the interior surfaces of the tunnel were gold-plated and gold-plated reflector plates were mounted behind the side suction screens.

In the above experiment, the measurements of velocity and temperature profiles and of friction and heat transfer coefficients were made over a main-stream velocity range of 5 to 60ft/sec, and a length Reynolds Number range of 6500 to 3300000. The mass transfer velocity range was -0.3 to 0.26ft/sec, and included constant axial mass transfer velocity, and $\frac{1}{\sqrt{x}}$ and $\frac{1}{x^{.2}}$ distributions. The boundary layer velocities were measured by pitot probes made from 0.019 inch outside diameter hypodermic needle. The temperature of the mainstream air was about 80°F and the temperature of the injected air was about 25°F higher. The measured laminar-boundary-layer velocity and temperature profiles, and the laminar region friction coefficients showed good agreement with theory. The results indicated that suction decreased the boundary -layer thickness, increased the friction and heat transfer coefficients, and retarded transition from laminar to turbulent flow, while blowing did the opposite. The largest deviations between laminar-boundary-layer theory and experimental results were observed when blowing occurred. The measured turbulent velocity and temperature boundary-layer profiles were similar when constant mass transfer rate was used or when it varied as $\frac{1}{x^{.2}}$.

The experiments of Mickley et al (see ref. 46) did not simulate the assumptions used in developing the theory of heat transfer through a boundary layer on a flat plate with injection, since the "coolant" was heated and blown through the porous wall into a cooler main stream. After completing the experiment, the authors found that the woven Fiberglass-Nichrome wire heater cloth, attached directly to the back side of the porous test wall, became separated from the test wall while the tunnel was being moved. Although the wall was only 0.04 inch thick and the air space between the heater cloth and the test wall was less than 0.03 inch, sufficient longitudinal flow behind the porous wall invalidated the test results obtained after the tunnel was moved.

Locke (see ref. 43) investigated heat transfer and flow friction characteristics of porous solids. He carried out tests with a range of Reynolds Numbers from 32 to 600. The transition region started at a Reynolds Number of 1200.

Green (see ref. 26) investigated heat transfer in porous media. A hollow porous graphite cylinder was heated to incandescence by the passage of direct current, and cold nitrogen entered at one end and flowed radially inward through the specimen. Norton et al (see ref. 50) measured the thermal conductivity of porous refractry materials. It was found that the conductivity of Alumina decreased linearly with porosity.

Schneider (see ref. 57), Green and Lemke (see ref. 28), Weinbaum and Wheeler (see ref. 61), and Grootenhuis (see ref. 29) solved the equation for the heat transfer through a porous wall with a fluid flowing in a direction opposite to that of the direction of heat flow. Ness (see ref. 48) proposed equations for the temperature distribution along a semi-infinite sweat-cooled plate. Yuan (see ref. 69) solved the equations for heat transfer in laminar compressible boundary layer on a porous flat plate with fluid injection.

Coppage (see ref. 9), Yates (see ref. 64), and Eisenklam and Hargreaves (see ref. 20) conducted experiments on flow of fluids through porous media. Kay (see ref. 38), Scheidegger (see ref. 56), and Carman (see ref. 7) presented the equations governing flow of fluids through porous media.

THEORETICAL CONSIDERATIONS

Equation for Heat Transfer in a Porous Material

Figure 3 shows the temperature distribution with effusion through a porous wall. The heat flow is assumed to be one-dimensional and is in a direction opposite to the coolant flow. The heat is conducted through the solid and is picked up by the coolant. The porous medium is assumed to be constructed of channels, which are separated from each other by thin walls.

Writing a heat balance on element dx:

Heat conducted along the matrix per unit area = $k_s \frac{d^2t}{dx^2}$

Heat absorbed by the coolant per unit area = $h'(t-T) = G_c C_p \frac{dT}{dx}$

or $$k_s \frac{d^2t}{dx^2} = h'(t-T) = G_c C_p \frac{dT}{dx} \qquad \ldots (1)$$

where

k_s = thermal conductivity of the porous matrix

h' = internal heat transfer coefficient per unit volume of porous material

C_p = specific heat of coolant

G_c = mass flow per unit frontal area

t = wall temperature

T = coolant temperature

From (1):

$$t = T + \frac{G_c C_p}{h'} \frac{dT}{dx} \qquad \ldots (1a)$$

and

$$k_s \frac{d^2}{dx^2}\left(T + \frac{G_c C_p}{h'} \frac{dT}{dx}\right) = G_c C_p \frac{dT}{dx}$$

$$\frac{G_c C_p}{h'} \frac{d^3T}{dx^3} + \frac{d^2T}{dx^2} - \frac{G_c C_p}{k_s} \frac{dT}{dx} = 0$$

dividing by $\frac{G_c C_p}{h'}$ we obtain

$$\frac{d^3T}{dx^3} + \frac{h'}{G_c C_p} \frac{d^2T}{dx^2} - \frac{h'}{k_s} \frac{dT}{dx} = 0 \qquad \ldots (2)$$

The solution to (2) is given by:

$$T = C_1 + C_2 e^{(B - \frac{A}{2})x} + C_3 e^{-(B + \frac{A}{2})x} \qquad \ldots (3)$$

and combining (3) and (1a)

$$t = C_1 + \left(\frac{1}{2} + \frac{B}{A}\right) C_2 e^{(B - \frac{A}{2})x} + \left(\frac{1}{2} - \frac{B}{A}\right) C_3 e^{-(B + \frac{A}{2})x} \ldots (4)$$

or

$$T = C_1 + C_2 e^{L_2 x} + C_3{}^{L_3 x} \qquad \ldots (3a)$$

and

$$t = C_1 + M C_2 e^{L_2 x} + N C_3 e^{L_3 x} \qquad \ldots (4a)$$

where

$$A = \frac{h'}{G_c C_p}$$

$$B = \sqrt{\frac{h'}{K_s} + \left(\frac{A}{2}\right)^2}$$

$$L_2 = \left(B - \frac{A}{2}\right)$$

$$L_3 = -\left(B + \frac{A}{2}\right)$$

$$M = \left(\frac{1}{2} + \frac{B}{A}\right)$$

$$N = \left(\frac{1}{2} - \frac{B}{A}\right)$$

The boundary conditions are as follows:

at $x = 0$, $t = t_o$, and $T = Tc$

$x = 1$, $t = ts$, and $T = Ts$

Although ts and Ts are treated as different quantities, they are equal. The heat transfer inside the porous wall is from the matrix to the coolant and therefore the matrix temperature is higher than the coolant temperature. At the surface $ts \geqslant Ts$. Outside the surface, the heat transfer is from the hot fluid to the wall and therefore $ts \leqslant Ts$. At the surface both of the above conditions must be satisfied. Therefore, at the hot surface $ts = Ts$.

Applying the boundary conditions to (4a)

at $x = 0$, $t_o = C_1 + MC_2 + NC_3 \qquad \ldots (5)$

at $\quad x = 1, \quad ts = C_1 + MC_2e^{L_2l} - NC_3e^{L_3l}$ ... (6)

From (1):

$$T = t - \frac{ks}{h'}\frac{d^2t}{dx^2} \qquad \text{... (1b)}$$

Differentiating (4a) twice

$$\frac{d^2t}{dx^2} = L_2^2 MC_2 e^{L_2x} + L_3^2 NC_3 e^{L_3x}$$

Substituting into (1b) and rearranging

$$T = C_1 + MC_2(1 - K'L_2^2)e^{L_2x} + NC_3(1 - K'L_3^2)e^{L_3x}$$

where $\quad K' = \frac{ks}{h'}$

Introducing the boundary condition at x = 1 we have

$$Ts = C_1 + MC_2(1 - K'L_2^2)e^{L_2l} + NC_3(1 - K'L_3^2)e^{L_3l}$$

Now (5), (6), and (7) must be solved for C_1, C_2, and C_3 ... (7)

From (5):

$$C_1 = to - MC_2 - NC_3 \qquad \text{... (5a)}$$

Substituting the above into (6)

$$t_s = to - MC_2 - NC_3 + MC_2e^{L_2l} + NC_3e^{L_3l}$$

or

$$t_s = to + MC_2(e^{L_2l} - 1) + NC_3(e^{L_3l} - 1) \qquad \text{... (8)}$$

Substituting for C_1 in (7)

$$T_s = to - MC_2 - NC_3 + MC_2(1 - K'L_2^2)e^{L_2l} + NC_3(1 - K'L_3^2)e^{L_3l}$$

or

$$T_s = to + MC_2[(1 - K'L_2^2)e^{L_2l} - 1] + NC_3[(1 - K'L_3^2)e^{L_3l} - 1] \qquad \text{... (9)}$$

Solving (9) for C_2

$$C_2 = \frac{T_s - t_o - NC_3[(1-k'L_3^2)e^{L_3\ell} - 1]}{M[(1-k'L_2^2)e^{L_2\ell} - 1]} \qquad \ldots (10)$$

Substituting C_2 into (8)

$$t_s = t_o + M\left\{\frac{T_s - t_o - NC_3[(1-k'L_3^2)e^{L_3\ell} - 1]}{M[(1-k'L_2^2)e^{L_2\ell} - 1]}\right\}(e^{L_2\ell} - 1) + NC_3(e^{L_3\ell} - 1)$$

and therefore C_3 is given by

$$C_3 = \frac{t_s - t_o - \dfrac{(T_s - t_o)(e^{L_2\ell} - 1)}{[(1-k'L_2^2)e^{L_2\ell} - 1]}}{N(e^{L_3\ell} - 1) - \dfrac{N(e^{L_2\ell} - 1)[(1-k'L_3^2)e^{L_3\ell} - 1]}{[(1-k'L_2^2)e^{L_2\ell} - 1]}}$$

or

$$C_3 = \frac{t_s - t_o - (T_s - t_o)X}{Y} \qquad \ldots (11)$$

Substituting for C_3 in (10) gives

$$C_2 = \frac{T_s - t_o - \dfrac{N[t_s - t_o - (T_s - t_o)X]}{Y}[(1-k'L_3^2)e^{L_3\ell} - 1]}{M[(1-k'L_2^2)e^{L_2\ell} - 1]}$$

and from (5a) C_1 is determined. ... (12)

Thus applying the experimentally obtained values to equations for C_1, C_2, and C_3, the temperature distributions of the coolant or the wall may be obtained from equations (3a) and (4a).

If the assumption is made that the matrix and the coolant temperatures are the same, (1) becomes a second order differential equation. The solution to this simplified equation is:

$$T = \frac{T_s\left(e^{-bx} - e^{-bl}\right) + T_c\left(1 - e^{-bx}\right)}{1 - e^{-bl}}$$

where $\quad b = \dfrac{G_c C_p}{k_s}$

The overal thermal conductivity of the matrix and the coolant in it is defined as:

$$k_m = \frac{G_c C_p (T_s - T_c)\, l}{(t_s - t_o)}$$

where $\quad l$ = width of the porous wall

The Reynolds and Nusselt Numbers inside the matrix are given by:

$$Re = \frac{G_c d}{\mu f} \qquad \text{and} \qquad Nu' = \frac{h' d^2}{6(1-f)k}$$

where $\quad d$ = particle size or pore diameter

f = porosity

μ = dynamic viscosity of coolant

k = thermal conductivity of coolant

The cooling efficiency is expressed as:

$$\eta = \frac{T_1 - t_s}{T_1 - T_c}$$

where $\quad T_1$ = hot gas temperature

Heat Transfer Through the Boundary Layer on a Porous Plate with Injection

When laminar flow occurs in systems of very simple geometry, laminar boundary-layer theory may be applied to calculate the velocity and temperature profiles, and the corresponding heat transfer coefficients. Although the laminar boundary-layer theory introduces an idealization of the flow process, the theory gives a close approximation to the actual physical situation. In actual practice turbulent boundary layer occurs, and a smaller reduction in heat flow will occur than calculated by the laminar boundary-layer theory. Also, since the isolating effect of the coolant film is better in the case of a laminar boundary layer, the laminar boundary-layer solution will give an upper limit for the decrease of the heat transfer coefficient by transpiration cooling.

In the application of the laminar boundary-layer theory the physical model is the flow of fluid over a flat plate through which coolant is injected at right angles to the main stream (see fig.4). Following assumptions are made:

1. The Prandtl Number is equal to unity.
2. The flow is laminar.
3. The two-dimensional flat plate is parallel to the main stream.
4. The coolant injection starts at the commencement of boundary-layer growth.
5. The fluid flowing along the plate and the coolant flowing through the pores are the same homogenous fluid.
6. The coolant is injected uniformly at right angles to the main stream.
7. The cooled surface is at a uniform temperature.
8. No heat is transferred in a direction perpendicular to the coolant flow.
9. The inverse proportion between mass density and temperature inside the boundary layer is used.
10. The viscosity is proportional to the square root of the temperature.
11. The velocity profile is expressed by a polynomial of the fourth degree.

12. The temperature is expressed by a parabolic function of the velocity only.

13. No pressure gradient exists across the boundary layer.

The equation of motion in the boundary layer of a flat plate in steady compressible flow is given by:

$$\rho u \frac{\partial u}{\partial x} + \rho v \frac{\partial u}{\partial x} = \frac{\partial}{\partial y}\left(\mu \frac{\partial u}{\partial y}\right) \qquad \text{... (a)}$$

where the x-axis and the y-axis are chosen as shown in Figure 4, and u and v are the "x" and "y" components of the velocity at any point.

The equation of continuity is:

$$\frac{\partial}{\partial x}(\rho u) + \frac{\partial}{\partial y}(\rho v) = 0 \qquad \text{... (b)}$$

The equation expressing the energy balance between the heat produced by viscous dissipation and the heat transferred by conduction and convection is given by:

$$\rho u \frac{\partial}{\partial x}(c_p T) + \rho v \frac{\partial}{\partial y}(c_p T) = \frac{\partial}{\partial y}\left(k \frac{\partial T}{\partial y}\right) + \mu\left(\frac{\partial u}{\partial y}\right)^2 \qquad \text{... (c)}$$

where $k =$ conductivity of the fluid

Applying boundary conditions and solving equations (a) and (c), the relationship between T and U is obtained

$$\frac{T}{T_1} = \frac{T_s}{T_1} - \left(\frac{T_s}{T_1} - 1\right)\frac{u}{u_1} + \frac{\gamma - 1}{\gamma} M^2 \frac{u}{u_1}\left(1 - \frac{u}{u_1}\right) \qquad \text{... (d)}$$

where $U =$ the velocity outside the boundary layer

$T_s =$ temperature of the plate surface

$T_1 =$ temperature of the main stream

For zero pressure gradient, the perfect gas equation of state gives:

$$\frac{\rho}{\rho_1} = \frac{T_1}{T} \qquad \dots (e)$$

The viscosity variation with temperature is given by

$$\frac{\mu}{\mu_1} = \left(\frac{T}{T_1}\right)^{1/2} \qquad \dots (f)$$

Integrating the equation of motion between the limits $y = 0$ and $y = \delta$, and using the equation of continuity and the following boundary conditions:

$$y = 0 : \quad u = 0 , \quad v = v_0$$
$$y = \delta : \quad u = U_1 , \quad v = v(\delta)$$

we obtain

$$\frac{\partial}{\partial x}\int_0^\delta \rho u^2 dy - U_1 \frac{d}{dx}\int_0^\delta \rho u dy + \rho_0 v_0 U_1 = \left[\mu \frac{\partial u}{\partial y}\right]_0^\delta \qquad \dots (g)$$

where δ = boundary layer thickness

v_0 = coolant injection velocity

ρ_0 = density of the coolant

The velocity profile is:

$$\frac{u}{U_1} = a(\eta) + b(\eta)^2 + c(\eta)^3 + d(\eta)^4 \qquad \dots (h)$$

where $\eta = \frac{y}{\delta}$

with the following boundary conditions:

$$y = \delta : \quad u = U_1 , \quad \frac{\partial^2 u}{\partial y^2} = 0, \quad \frac{\partial u}{\partial y} = 0$$
$$y = 0 : \quad u = 0 , \quad v = v_0 , \quad \rho_0 v_0 \left(\frac{\partial u}{\partial y}\right)_s = \mu_s\left(\frac{\partial^2 u}{\partial y^2}\right)_s + \left(\frac{\partial \mu}{\partial y}\right)_s\left(\frac{\partial u}{\partial y}\right)_s$$

The constants a, b, c, and d are given by:

$$a = \frac{2}{1+\lambda}, \quad b = \frac{6\lambda}{1+\lambda}, \quad c = -\frac{2+8\lambda}{1+\lambda}, \quad d = \frac{1+3\lambda}{1+\lambda}$$

where $\lambda = \frac{\rho_0 v_0 \delta}{6\mu_s} - T_f$ and $T_f = \frac{n_T - 1}{12} + \frac{n_T}{12}\frac{\gamma-1}{2}M^2$ for $\mu \sim T^{1/2}$

$T_f = \frac{n_T - 1}{8} + \frac{n_T}{8}\frac{\gamma-1}{2}M^2$ for $\mu \sim T^{3/4}$ ... (i)

$n_T = T_1/T_s$

The velocity distribution is then given by:

$$\frac{u}{U_1} = \frac{2}{1+\lambda}\eta + \frac{6\lambda}{1+\lambda}\eta^2 - \frac{2+8\lambda}{1+\lambda}\eta^3 + \frac{1+3\lambda}{1+\lambda}\eta^4 \quad \text{... (j)}$$

and the density and viscosity by:

$$\rho = \rho_1\left[\frac{T_s}{T_1} - \left(\frac{T_s}{T_1} - 1\right)\eta + \frac{\gamma-1}{2}M^2\eta(1-\eta)\right]^{-1} \quad \text{... (k)}$$

and:

$$\mu = \mu_1\left[\frac{T_s}{T_1} - \left(\frac{T_s}{T_1} - 1\right)\eta + \frac{\gamma-1}{2}M^2\eta(1-\eta)\right]^{n} \quad \text{... (l)}$$

where $n = \frac{1}{2}$ or $\frac{3}{4}$

Equations (j), (k), and (l) are substituted into the first two terms of equation (g), which are then differentiated. The result of the two differentiations is substituted back into equation (g) , which is then a linear equation and can be solved by direct integration. The constant of integration is solved from the boundary conditions. This equation gives an expression for the non-dimensional length $\xi = \left(\frac{\rho_0 v_0}{\rho_1 U_1}\right)\frac{U_1 x}{\gamma_1}$ in terms of the main-stream temperature, boundary-layer temperature, wall temperature, coolant mass flow, wall and main-stream viscosities, and the main-stream Mach Number. This equation is not valid for M = 0, and the equation is modified to apply for this condition. These solutions are given by Yuan (see ref. 69). Graphical representation of these solutions is given in Figures 34 to 39. Figures 34 and 35 show the growth in the boundary-layer thickness with the increase of Mach Number and the ratio of the main-stream temperature to the wall temperature. The compressibility effect increases the heat transfer through the wall, and the amount of heat produced in the boundary layer increases with speed. Therefore the increase of Mach Number or the temperature ratio have the same effect on the boundary-layer thickness.

Figures 36 and 37 show velocity profiles plotted against $y(v_0/\nu_1)$ and $y\,U_1/\nu_1$ respectively for various nondimensional lengths, ξ, and Mach Numbers.

Figures 38 and 39 show the temperature distribution plotted against $y\,U_1/\nu_1$ for different Mach Number and ratios of v_0/U_1. The temperature gradient at the wall increases with Mach Number, and decreases with increasing v_0/U_1. This indicates that the heat transfer through the wall increases with the increase in the compressibility effect and decreases as the injection rate increases.

The velocity and temperature profiles for heat transfer through a laminar boundary layer may be obtained more readily by making the following simplifying assumptions: 1) no axial pressure gradient; 2) no variation in fluid properties; 3) $v_0 \propto \frac{1}{\sqrt{x}}$.

The equations of motion, continuity, and energy are simplified to:

$$u\frac{\partial u}{\partial x} + v\frac{\partial u}{\partial y} = \frac{\mu}{\rho}\frac{\partial^2 u}{\partial y^2} \qquad \text{... (I)}$$

and

$$\frac{\partial u}{\partial x} + \frac{\partial v}{\partial y} = 0 \qquad \text{... (II)}$$

$$u\frac{\partial T}{\partial x} + v\frac{\partial T}{\partial y} = \frac{k}{c_p\rho}\frac{\partial^2 T}{\partial y^2} \qquad \text{... (III)}$$

The boundary conditions are:

$$\begin{aligned} y &= 0: \quad & u &= 0, \quad v = v_0(x) \\ y &= \infty: \quad & u &= U_1, \quad \frac{\partial}{\partial y} = 0, \; T = T_1 \end{aligned} \qquad \text{... (IV)}$$

If the following substitutions are made:

$$\eta = \frac{y}{2x}\sqrt{\frac{u_1 x \rho}{\mu}}$$

$$f = f(\eta) = \frac{\psi}{\sqrt{\frac{u_1 x \mu}{\rho}}} \qquad \text{... (V)}$$

where Ψ is the stream function

the momentum equation becomes:

$$f''' + f'' = 0 \qquad \text{... (VI)}$$

with the boundary conditions:

$$\eta = 0: \; f'(0) = 0, \; f(0) = -\frac{2v_0}{u_1}\sqrt{\frac{u_1 x \rho}{\mu}}$$

$$\eta = \infty: \; f'(\infty) = 2, \; f''(\infty) = 0 \qquad \text{... (VII)}$$

A valid solution is obtained only for f(0) = constant = C, or when the injection velocity is given by:

$$v_0 = -\frac{C}{2}\frac{u_1}{\sqrt{\frac{u_1 x \rho}{\mu}}} \qquad \text{... (VIII)}$$

The velocity and temperature profiles are obtained by generalizing equations (I), (II), and (III) and solving the resulting equation. For this purpose dimensionless profile moduli,

$$\beta_F = \frac{u}{u_1} = \frac{1}{2} f'(\eta)$$

$$\beta_H = \frac{T_s - T}{T_s - T_1}$$

and dimensionless fluid property groups,

$$Z_F = 1$$

$$Z_H = \frac{c_p \mu}{k} \qquad \text{... (IX)}$$

are introduced into equations (I), (II), and (III). This gives:

$$u \frac{\partial \beta}{\partial x} + v \frac{\partial \beta}{\partial y} = \frac{\mu}{\rho Z} \frac{\partial^2 \beta}{\partial y^2} \qquad \text{... (X)}$$

If wall temperature, Ts, and the main-stream temperature are independent of x (X) becomes:

$$\beta'' + Z f \beta' = 0 \qquad \text{... (XI)}$$

with following boundary conditions:

$$\eta = 0 \ , \ \beta = 0$$

$$\eta = \infty \ , \ \beta = 1 \ , \ \beta' = 0 \qquad \text{... (XII)}$$

where f denotes the solutions to equations (VI) and (VII).

If values of $f(\eta)$ are available $\beta(\eta)$ may be found by direct integration:

$$\beta'(\eta) = \beta'(0)\left[\exp\left(-Z\int_0^{\eta} f\,d\eta\right)\right] \qquad \text{... (XIII)}$$

$$\beta(\eta) = \beta'(0)\int_0^{\eta}\left[\exp\left(-Z\int_0^{\eta} f\,d\eta\right)\right]d\eta \qquad \text{... (XIV)}$$

and with the boundary condition that $\beta(\infty) = 1$

$$\beta'(0) = \frac{1}{\int_0^{\infty}\left[\exp\left(-Z\int_0^{\eta} f\,d\eta\right)\right]d\eta} \qquad \text{... (XV)}$$

Mickley et al (see ref. 46) used values of $f(\eta)$ given by Schlichting to give numerical solutions to equations (XIII), (XIV), and (XV). Figure 40 shows representative profiles, β , obtained by this method.

Pressure Drop Across Porous Walls

The equation of flow of homogenous incompressible fluids through porous media is developed as follows:

$$\text{Porosity, } f = \frac{\text{volume of voids}}{\text{total volume}} = \frac{Ae}{A}$$

where A = total cross-sectional area

Ae = effective cross-sectional area of the voids

The effective axial velocity component in the voids is:

$$Ue = \frac{Q}{Ae} = \frac{Q}{A}\,\frac{1}{f} = \frac{Um}{f}$$

where Q = volumetric flow

Um = mean approach velocity

Because of twisting of the passages in the porous material, the effective length l_e of a channel will be greater than the height of the porous bed, l . The effective mean value of the absolute fluid velocity is:

$$V_e = u_e \frac{l_e}{l} = \frac{u_m}{f}\,\frac{l_e}{l}$$

From the Hagen-Poiseuille Law for viscous flow in pipes, the pressure drop across a porous bed is:

$$\Delta p = \frac{k_o \mu V_e l_e}{m^2}$$

where m = hydraulic radius of void passages

Ko = constant

Comparing the above with

$$\Delta p = \frac{32 \mu u_m l}{D^2}$$

(Hagen-Poiseuille Law)

it is seen that:

4m = D (pipe diameter)

and Ko = 2 (this value applies strictly to passages of circular cross-section only)

The hydraulic radius of the voids is:

$$m = \frac{\text{flow area}}{\text{wetted perimeter}} = \frac{\text{volume of fluid in the bed}}{\text{wetted surface}}$$

$$= \frac{f A l}{\text{wetted surface}} = \frac{f}{S}$$

where S = wetted surface per unit volume of porous material

After substitution into (1) we have:

$$\Delta p = K_0 \frac{S^2}{f^3} \left(\frac{l_e}{l}\right)^2 \mu \, u_m \, l$$

The above is called the Carman-Kozeny Equation. It can be also written as:

$$\Delta p = K \frac{S^2}{f^3} \mu \, u_m \, l$$

where $K = K_0 \left(\frac{l_e}{l}\right)^2 \doteq 5$ (see ref. 7).

For consolidated porous media the Carman-Kozeny equation does not agree well with experimental results, because of the inaccuracy in measurement of the wetted surface and the high tortuosity of the porous materials.

Two other equations for the pressure drop through porous media are given below:

1. Blake Equation:

$$\Delta p = K \mu \frac{u}{d} \left(\frac{1-f}{f}\right)^2$$ Laminar flow

$$\Delta p = K \rho \frac{u^2}{d} \left(\frac{1-f}{f}\right)$$ Turbulent flow

(see ref. 33)

where d = characteristic particle diameter

K = experimentally determined constant

2. Beldecos Equation:

$$\Delta p = \frac{2FGl\lambda(1-f)^2}{dg\rho f^3} \qquad Re < 10$$

with $F = 100\left(\frac{dG}{\mu}\right)^{-1}$

and $$\Delta p = \frac{2FG^2 l\lambda^{1.1}(1-f)}{dg\rho f^3} \qquad Re > 300$$

with $F = 1.75\left(\frac{dG}{\mu}\right)^{-.1}$

where $\lambda = .205\frac{A}{V_p^{2/3}}$ = shape factor

A = surface area of particle, ft^2

G = mass velocity

V = volume of particle (see ref. 71)

The permeability of a porous medium is given by:

$$K_p = \frac{-Q}{A}\Big/\left(\frac{\Delta p}{\rho g l} + 1\right) \qquad \text{(see ref. 56, page 56)}$$

DESCRIPTION OF APPARATUS

Heat Transfer Rig

The apparatus consisted of a large fan, a combustion chamber, a test section, and a coolant air supply system. The air supplied by the fan was heated by burning propane in the combustion chamber and then exhausted into the test section. One vertical wall of the test duct had a porous bronze slab installed in it. Cooling air, whose injection velocity was varied as the inverse of the square root of the distance along the porous plate, was injected through the porous wall at right angles to the main-stream air flow. To simulate the condition of zero boundary-layer thickness at the leading edge of the porous plate, the boundary layer was bled off through a slit located $\frac{1}{4}$ inch upstream of the porous plate. The coolant mass flow, main air mass flow, and main air temperature were varied to give the widest possible range of test conditions. Provisions were made for the measurement of hot and cold side temperatures of the porous wall and the coolant and hot air temperatures. These temperatures, with the coolant mass flow, were needed for the determination of the heat transfer coefficients of the porous wall. Pitot probes and thermocouples were used in traversing the boundary layer to give the velocity and temperature profiles for a sweat cooled wall with a turbulent boundary layer.

The main air was supplied by a low pressure fan at about $1\frac{1}{4}$ psig. It was then heated in a combustion chamber. The combustion chamber consisted of an 8 inch I.D. duct with a stainless steel flame tube and a Maxon Pilotpak burner nozzle. A bundle of small stainless steel tubes, acting as flow straighteners, was located in the 8 inch I.D. duct leading the hot air from the combustion chamber to the test section. A Honeywell Combustion Control was used to insure safe operation of the combustion equipment.

The test section was 2 inches wide, 3 inches high, and $17\frac{1}{4}$ inches long. In one of the vertical walls of the test duct the test specimen was installed and in the other a Pyrex window. The test specimen (see fig. 11) was made of sintered porous bronze of 41.4 per cent porosity. It was manufactured from 90 per cent Copper, 10 per cent Tin powder of 60 to 80 mesh size. Four thermocouples were imbedded in the coolant-duct-side surface of the porous wall at 1, 4, 7, and 9 inches from the leading edge and at about the main height of the test wall. The thermocouples were placed in $\frac{1}{4}$ long vertical grooves. The thermocouple wires were led along the grooves to reduce errors due to conduction on the plate surface. Four thermocouples were placed in small vertical holes in the test wall at varying distances from the hot surface. These thermocouples were intended to measure the temperature distribution in the wall.

The inside surfaces of the test duct were made of very highly polished stainless steel in order to reduce the heat transfer to the test wall by radiation.

A shielded thermocouple, which could be moved in the vertical direction by a traversing gear, was located at the entrance to the test section. Just above the Pyrex window, at distances of 0.09, 1.1, 4.05, 9.0 and 12.05 inches from the leading edge of the test wall, were located five pitot-thermocouple probes, which were used to traverse the boundary-layer profiles at mid-height of the test duct and in a direction perpendicular to the test wall. The location of the seoond, third, and fourth probes corresponded to that of the thermocouples on the coolant-side of the test wall. The pitot probe was made of 0.008 inch I.D. and 0.016 inch stainless steel tubing. The probes were moved by a traversing gear and the distance of movement was measured by an Ames Dial Gauge.

The coolant duct, which was divided into 2, 4, and 6 inch long compartments, covered the cold side of the test specimen. The coolant duct was dividend into compartments to facilitate the coolant mass flow regulation in order to provide a coolant injection velocity which varied as the inverse of the square root of the distance along the plate. The coolant air was supplied at about 110 psig from the laboratory high pressure air supply system. The air was passed through a Micro-Klean Air Line Filter so that even the microscopic dirt particles would be removed. Otherwise the porous wall would become plugged, and the permeability of the wall would change. From the filter the air passed through a coolant manifold and pressure reducing valves to the coolant duct compartments. To smooth out the flow each coolant compartment had two fine-mesh screens installed in it. Each coolant compartment had a thermocouple at its centre to measure the coolant inlet temperature.

All the thermocouples were connected to a self-balancing Honeywell Brown Electronic Potentiometer. The hot surface temperature of the test wall was measured by a Siemens Ardonox Radiation Pyrometer, which was mounted in such a way that it could be moved parallel to the test wall. The radiation energy from the test wall was focussed by a mirror on a 23-element thermopile. The output from this thermopile was passed through the Ardonox internal circuits and was measured on a very sensitive galvanometer connected to the Ardonox. The Ardonox was calibrated to obtain the relationship between the galvanometer reading and the surface temperature.

A more detailed description of the apparatus is given in Appendix 1. See also Figures 5 to 16.

Pressure Drop Test Rig

This rig consisted of a 6 inch I.D., 24 inches long settling chamber, to which a brass bellmouth was attached.(see fig. 17). The test plugs were inserted into the bellmouth and the static pressure taps on both sides of the plug were used to measure the pressure upstream and downstream of the plug. The air supplied to this rig came from the high pressure supply through the air filter and several regulating valves.

Six 1 inch O.D., $\frac{1}{2}$ inch thick porous bronze (90 per cent Copper, $9\frac{1}{2}$ per cent Tin, and $\frac{1}{2}$ per cent Carbon) plugs of about 20, 25, 30, 35, 40, and 45 per cent porosities were used. Figures 18 to 23 show the microphotographs of these specimens. The manufacturer of these plugs experienced a great deal of difficulty in obtaining the required porosity range. To achieve this, non-spherical grain powder was used and the plugs were pressed after sintering.

EXPERIMENTAL PROCEDURE

Heat Transfer Tests

Series of tests were carried out at 4 main air mass flows, 4 test duct temperatures, 3 coolant mass flows, and 2 traverse probe planes. Because of the time required to transfer the traversing mechanism from one pitot probe to the other, the tests in the two traverse probe planes were carried out separately. The tests were carried out first with boundary layer traversing at the location corresponding to the centre of the second coolant duct compartment, and then at the location corresponding to the centre of the third coolant compartment, i.e. at 4.0625 and 9 inches from the leading edge of the porous plate respectively.

After the rig was warmed up and the test specimen temperature remained constant for about 5 to 10 minutes, the first pitot probe was used to check whether the boundary layer thickness at the leading edge of the test wall was zero. Since the capacity of the suction fan was high, one suction line valve setting was adequate for all tests. A check of the temperature distribution along the plate was made with the Ardonox. Then the temperatures, pressures, and orifice pressure drops were recorded. At the end of each test the traversing by the pitot-thermocouple probe was conducted.

The coolant injection velocity along the plate was made to vary as the inverse of the square root of the distance along the wall or $v_o = \frac{K}{\sqrt{z}}$. This was to insure a fairly constant porous wall temperature on the duct side. The tests were carried out at values of K equal to 0.1378, 0.320, and 0.472. The highest value of K corresponded to the highest mass flow available from the high pressure air supply.

The tests were conducted at combustion chamber outlet temperatures of about 90, 210, 300, and 390°F. One run was conducted at 480°F and one at 560°F. The main-stream velocity ranged from 58 ft/sec. to 110 ft/sec.

Pressure Drop Tests

The porosity of the plugs was determined by measurement of their volume and weight. The same procedure was followed with the porous wall used in the heat transfer tests. Microphotographs of the surface of the plugs were made for the determination of the pore areas and the wetted surfaces. Since the pore structure varied greatly from one region of the surface to another, a "representative" pore structure for each plug could not be found. Also, the pore boundaries were not well defined even after the plugs were etched by different chemicals.

The test samples were glued with epoxy resin into small sleeves, which held the plugs in place in the bellmouth. Before testing, all speciments were washed in alcohol.

The pressure drop test consisted of recording pressures on each side of the test plug, held in the bellmouth, for different air mass flows.

DISCUSSION OF EXPERIMENTAL RESULTS

Heat Transfer through Porous Wall

The tests were conducted at coolant injection velocities of o.237, 0.551, and 0.812 ft/sec. at the first traverse plane, and 0.168, 0.390, and 0.576 ft/sec. at the other. The porous wall Reynolds Number based on the particle diameter ranged from 0.8 to 4.5. The main-stream velocity ranged from 60 to 110 ft/sec., and the main stream Reynolds Number, based on the hydraulic radius, ranged from 40,000 to 90,000. The main-stream temperature ranged from 580 to 1000°R.

To obtain h', the heat transfer coefficient per unit volume, the coolant and the porous wall surface temperatures on the cold side and hot side were inserted into the equation for the temperature distribution in a porous slab (see equation 4a). An iteration was conducted on an electronic computer to obtain h', which was the only unknown in that equation. Because of the complexity of the equation, the computer would stop if the first guessed h' was not very close to the correct value. Only by restarting the program several times with successively better guesses of h' could the correct value be obtained. This process took a fairly long time on the Bendix 500 computer which was used in the calculations. Since the available computer time was limited, h' was calculated for a few test runs only.

In calculating the Nusselt Number, h' is used. The Nusselt Number is given by:

$$Nu' = \frac{h'd^2}{6\left[(1-f)k\right]}$$

where

$\frac{6(1-f)}{d}$ represents the surface area per unit volume for a bed of spheres.

If the simplifying assumption is made that the porous wall is composed of long parallel cylindrical channels, then "d" used in the Nusselt Number is the diameter of the cylinders. Since the channels in a sintered porous material are not cylindrical and are very tortuous, this assumption is not adequate. If the porous material is assumed to be constructed of very small spheres, then d is the sphere diameter. This is a better assumption, but not strictly accurate. In sintering porous materials, the shapes of the spheres are distorted and their boundaries fuse together. Thus "d" defined this way is not a true representative distance for a sintered porous material, but it is used for lack of a better one. The particle diameter used in these calculations was calculated from the average mesh size of the particles used in the fabrication of the porous wall. The value for d was calculated to be 0.00143 inch.

The Nusselt Number was plotted against the Reynolds Number, which was given by $\frac{G_c d}{\mu f}$. The mass flow per unit area, G_c , was divided by the porosity, f, to represent the actual mass velocity in the pores. Figure 24 shows this graph. A correlation line for the beds of granular materials, and some previous experimental results (see ref. 29) are also given on this graph. The points from this experiment lie close to the correlation line, but are somewhat removed from the previous experimental points. Since in the calculation of Nu' d is used, a small decrease in the value of d will lower the experimental points.

With coolant injection velocities of 0.237, 0.551, and 0.812 ft/sec, the values of h' were about 1.6×10^5 , 3.0×10^5 , and 4.4×10^5 Btu/hr. ft^2 °F/ft^3 respectively. The values of h' are given in Appendix 3. The few values of h' obtained indicate that h' increases with main-stream velocity, but is insensitive to the main-stream temperatures. Runs 7 and 10 are at the same main-stream temperature, but the velocities are 69 and 77 ft/sec. respectively. For run 10, a higher value of h' was obtained. Similarly, in runs 21 and 23, which have the same main-stream temperature, the main-stream velocities are 67 and 83 ft/sec. The resulting values of h' are 2.4×10^5 and 3.1×10^5 Btu/hr. ft.°F/ft.^{3} respectively. Because of the small number of experimental values obtained no definite conclusions can be reached. But since the increases in main-stream temperature and velocity increase the heat transfer to the porous wall, a similar effect can be expected on the porous wall.

Figures 25 to 28 show the computer calculated temperature distribution in the porous wall. After h' and the constants C_1, C_2, and C_3 are calculated by the computer, various values of x, the distances from the cold surface of the porous wall, are substituted into equation 4a and the wall temperatures are calculated. The curves show a very high temperature drop near the hot surface of the porous wall, while near the cold side the temperature decrease is smaller. Figure 25 also shows the readings obtained from the thermocouples imbedded in the porous wall. These thermocouples did not give good results. One reason for this may be that when the holes were drilled the passages in the porous wall were blocked, and the thermocouples were located in air pockets. This explains the fact that in Figure 25, near the cold surface of the wall, the measured temperature is higher than the calculated one, and near the hot surface it is lower.

Figures 29 and 30 show the cooling efficiency plotted against the ratio of the coolant mass flow to the main-stream mass flow for different coolant injection velocities. Figure 29 is for the first traverse station, and Figure 30 is for the second traverse station. Cooling efficiency, η , is defined as the ratio of the temperature difference between the main stream and the hot wall surface, and the temperature difference between the main-stream temperature. The cooling efficiency would be 100 per cent if the hot surface temperature were lowered to the same temperature as that of the coolant at inlet. The mass flow ratio is given by $\frac{\rho_o V_o}{\rho_1 U_1}$, where ρ_o and, V_o, and ρ_1, and U_1 are the density and velocity of the coolant and main stream respectively. The injection velocity is calculated from $V_o = \frac{K}{\sqrt{z}}$, where z is the distance from the leading edge of the porous plate, and the values of K are 0.1378, 0.320, and 0.472. The higher the mass flow ratio, the closer will the wall surface temperature approach the coolant temperature, and the higher will be the cooling effieiency.

Neglecting the experimental scatter of points, correlation lines are drawn on Figures 29 and 30. The slope of the correlation line for the first traverse station is 0.94 and for the second traverse station, 5 inches further downstream, the slope of the correlation line is 1.2. This indicates that for the same mass flow ratio higher cooling efficiency is obtained at the downstream station. This demonstrates increase of the blanketing effect produced by transpiration cooling as the distance along the plate increases. Figures 29 and 30 show that η is proportional to the mass flow ratio.

The highest cooling efficiency obtained at the first traverse station is 83 per cent for a mass flow ratio of 0.014, and at the second traverse station the highest cooling efficiency is 80 per cent for a mass flow ratio of 0.010. For the same flow ratio and main-stream temperature, the experimental points from runs with high main-stream velocity lie slightly below those with low main-stream velocity.

Figure 31 shows the combined thermal conductivity of the porous matrix and the coolant plotted against the mass flow ratio (equation for k_m

is given on page 24). The results from runs with the same velocity of injection lie on lines of constant combined thermal conductivity, k_m. Figure 31 indicates that for a constant velocity of injection k_m is independent of the mass flow ratio. Figure 32 shows k_m plotted against the injection velocity. The correlation line drawn on the graph shows that k_m is directly proportional to v_o. The results from runs at the second traverse station lie below this line. For values of v_o of 0.168, 0.237, 0.390, 0.551, and 0.812 ft/sec., k_m was 1.5, 3.0, 3.3, 5.5, and 8.0 Btu/hr. ft. °F. Appendix 3 gives values of k_m for all runs.

Heat Transfer Through Boundary Layer

With coolant injection the transition to turbulent flow occurs at very low Reynolds Number, therefore, all tests conducted in this experiment were in the turbulent range. The injection velocity was varied approximately as $\frac{1}{\sqrt{X}}$, to provide a fairly constant test wall surface temperature. When the porous wall surface temperature was measured by the Ardonox, it was found that the wall temperature near the leading edge was higher than in the middle section. But in the part of the porous plate where measurements were made, the surface temperature was fairly constant. The temperature at the second traverse station was only slightly lower than at the first station. Thus the condition of constant wall temperature was maintained fairly accurately. Since the texture of the porous slab was very fine, the injected fluid came into the mainstream in very small streams.

The film heat transfer coefficient is calculated from the following equation:

$$h = \frac{\omega\, C_p\, (t_s - T_c)}{(T_1 - t_s)}$$

where ω - coolant mass flow

c_p - specific heat of coolant inside the porous wall

t_s = hot porous wall surface temperature

T_c = coolant inlet temperature

T_1 = main stream temperature

Thus from the measured values of the coolant mass flow and the surface, main-stream, and coolant inlet temperatures the film heat transfer coefficient for all test runs is calculated.

Appendix 3 gives the film heat transfer coefficient on the hot side of the porous wall obtained from experimental results as well as a film heat transfer coefficient, h_c, for a solid plate calculated from the Dittus and Boelter's equation, $Nu = .0265\ Re_x^{.8}\ Pr^{.3}$, given in the Introduction to the Transfer of Heat and Mass, by Eckert. The Reynolds Number in this equation is based on the distance from the leading edge of the plate. The effectiveness of coolant injection in reducing the film heat transfer coefficient is evident. The value of the film heat transfer coefficient is reduced by coolant injection at first traverse station by at least 10 per cent at very low injections velocities, and up to 80 per cent at the highest injection velocity. At the second traverse station values of h for three runs were about the same as h_c. This was probably due to experimental inaccuracy. The experimental results show that the film heat transfer coefficient, h, increases with the main-stream velocity and decreases with the main-stream temperature. In runs 3, 4, and 5, T_1 and v_o are the same, and the main-stream velocities are 59.3, 66.5, and 70.2 ft/sec. The calculated values of h for these runs are 5.8, 7.9, and 9.8 Btu/hr. $ft.^2\ ^\circ F$ respectively. Similar increase in h with an increase in U_1 can be seen in other runs with same main-stream temperature and injection velocity. Runs 6, 10, and 12 have the same U_1 and v_o, but T_1 values of 594, 665, and 748°R. The values of h for these runs are 12, 11, and 9 Btu/hr. ft.^{2} °F respectively. Thus the results prove that h increases with U_1 and decreases with T_1.

Figure 33 shows h plotted against the mass flow ratio. The points with the same injection velocities are joined by curves. The curves at low mass flow ratios are almost vertical, while those at higher mass flow ratio are less steep and show that h increases with the main-stream velocity.

An attempt was made to find a correlation for h, by plotting Nu_x against Re_x on logarithmic scale. But the points showed no definite correlation, even when points with the same mass flow ratio were selected.

The plot of η, cooling efficiency, versus the product of the square of the mass flow ratio and the Reynolds Number is shown in Figure 41. A theoretical curve, based on an equation derived by Grootenhuis (see ref. 29), is shown on the same graph. The experimental points show a great amount of scatter and lie considerably below the theoretical curve. Experimental results obtained by other researchers (Friedman, Jakob, and Fieldhouse, Duwez and Wheeler) show a similar deviation from the theoretical curve (see ref. 29). Since the theoretical curve was derived with the assumption that there is no heat transferred by radiation and that the Prandtl Number equals unity, the experimental points should lie below it. For the same injection velocity and mainstream temperature the experimental points (in Figure 41) corresponding to runs with low mainstream velocity lie below the points with higher main-stream velocity. This is because $(T_1 - T_c)$ is constant, and with high U_1 the film heat transfer coefficient is higher. Therefore the surface temperature ts is higher, (T - ts) is smaller, and

$\eta = \dfrac{T_1 - t_s}{T_1 - T_c}$ is smaller.

Figures 42 to 44 show velocity profiles $\left(\frac{u}{U_1}\right)$ plotted versus a non-dimensional distance y/ϑ, where ϑ is the momentum thickness and is given by:

$$\vartheta = \int_0^\infty \frac{u}{U_1}\left(1 - \frac{u}{U_1}\right)dy$$

When plotted this way, the velocity profiles look similar. Since the pitot-thermocouple probe could not be brought very close to the wall, traversing of the region immediately next to the porous wall could not be performed.

Figures 45 to 54 show $\frac{u}{U_1}$ plotted versus a non-dimensional distance, $\frac{y}{2}\sqrt{\frac{U_1}{\nu x}}$. The profiles for the runs with the same injection velocities are similar, but the profiles for runs with higher U_1 are steeper. When comparing the velocity profiles for runs with different injection velocities it is evident that the higher the injection velocity the steeper is the profile. The theoretical curves for laminar boundary-layer velocity profiles (see fig. 40) are shifted to the right when coolant injection is present. The experimental profiles are for a turbulent boundary layer, but they exhibit a similar behaviour.

Figure 46 shows velocity profiles at the two traverse stations obtained from runs with same conditions (i.e. same T_1, U_1, and $v_o = \frac{K}{\sqrt{x}}$, where K = .1378). The points corresponding to the second traverse station are lower. This indicates that the boundary-layer thickness is increasing in the downstream direction and the velocity profiles are steeper near the leading edge of the porous plate.

Figures 55 to 63 show temperature $\left(\frac{T - t_s}{T_1 - t_s}\right)$ profiles plotted versus a non-dimensional distance $\frac{y}{2}\sqrt{\frac{U_1}{\nu x}}$. As was seen from the curves of velocity profiles, the temperature profiles are steeper at low injection velocities, and flatten out as the injection velocity is increased. This in qualitative agreement with Figure 40. The temperature profiles were plotted on logarithmic paper to see if these profiles follow a power-law distribution. The result was negative, since the graphs were not straight lines.

Pressure Drop Tests

The porosities of the bronze plugs were found to be 22.4, 25.3, 30.9, 36.9, and 40.8 per cent respectively. One plug was not tested because its surface was covered by epoxy resin, which plugged the pore openings. Figures 65 to 69 show the pressure drop across the plug plotted against air mass flow. Except at low mass flows the graphs show a straight line relationship between the pressure drop and the mass flow. This proves that the Carman-Kozeny equation is correct, since for any one plug it may be written as:

$$\Delta p = (\text{constant})\, \mu\, u_m\, l$$
$$= (\text{constant})\, u_m$$

and u_m is proportional to the mass flow.

CONCLUSIONS

The effect of air injection on the heat transfer through the porous bronze wall and the turbulent boundary layer in subsonic flow has been studied experimentally.

The heat transfer equation through a porous wall was solved to obtain h', the heat transfer coefficient per unit volume, and the temperature distribution inside the porous wall. For injection velocities of 0.237, 0.551, and 0.812 ft/sec., h' was calculated to be about 1.6×10^5, 3.0×10^5, and 4.4×10^5 Btu/hr. ft.^{2} °F/ft.^{3} respectively.

The cooling efficiency was found to be proportional to the mass flow ratio in the range of mass flow ratios from 0.004 to .014. The cooling efficiency improved with the distance along the plate.

The combined thermal conductivity was directly proportional to the injection velocity. For injection velocities of 0.168, 0.237, 0.390, 0.551, and 0.812 ft/sec., k_m was calculated to be 1.5, 3.0, 3.3, 5.5, and 8.0 Btu/hr. ft. °F.

The film heat transfer coefficient, h, was found to vary directly with the mainstream velocity, and inversely with the main-stream temperature.

Coolant injection into a turbulent boundary layer increased the boundary-layer thickness and flattened the velocity and temperature profiles. The larger the velocity of injection, the larger this effect was.

Pressure drop across porous bronze plug was proportional to the air mass flow.

BIBLIOGRAPHY

Reference Nos.

1. Abraham, L. H.
Techniques and Problems in Testing Structures at Elevated Temperatures
Aeronautical Engineering, Review, November 1956

2. Avery, W. H.
25 Years of Ramjet Development
Jet Propulsion, November 1955

3. Berman, A. S.
Laminar Flow in Channels with Porous Walls
Report No. K-944, Carbide & Carbon Chemicals Co.

4. Billington, I.
Hot Wire Anemometer and its Use in Non-Steady Flow
Aerophysics Laboratory, University of Toronto

5. Bond, J. W.
Problems of Aerophysics in the Hypersonic Region
Aero Digest, June 1956

6. Brunk, W. E.
Experimental Investigation of Transpiration Cooling for a Turbulent
Layer in Subsonic Flow Using Air as a Coolant
NACA TN 4091, 1957

7. Carman, P. C.
Flow of Gases Through Porous Media
Butterworths Scientific Publications, London, 1956

8. Churchill, S. W. and Stubbs, H. E.
Heat and Momentum Transfer from the Wall of a Porous Tube
ER 1-2323-9-F, 1957

9. Coppage, J. E.
Heat Transfer and Flow Friction Characteristics of Porous Media
Tech. Rept. No. 16, December 1, 1952
Dept. of Mech. Eng., Stanford University, Stanford, California

10. Cox, D. D.
Selecting Structural Materials for Hypersonic Flight
Aeronautical Engineering Review, January 1958

11. Debeau, D. E.
Evaluation of Porous Materials for Boundary-Layer Control
WADC-TR-56-484, 1956

12. Donoughe, P. L. and Livingood, J. N. B.
Exact Solutions of Laminar-Boundary-Layer Equations with Constant
Property Values for Porous Wall with Variable Temperature
NACA TN 3151

13. Dorrance, W. H.
Some Problems in the Aerothermodynamics of Hypersonic Flight
Aeronautical Engineering Review, January 1957

14. Driest, E. R. Van
Problems of Aerodynamic Heating
Aeronautical Engineering Review, October 1956

15. Duncombe, E.
An Experimental Investigation of Protection Achieved by Sweat Cooling on Porous Surfaces Adjacent to Non-Porous Surfaces
N.A.E. Report 16, 1952

16. Duwez, and Wheeler
Experimental Study of Cooling by Injection of a Fluid Through a Porous Material
Journal of the Aeronautical Sciences, Vol. 15, No. 9, p. 509

17. Eckert, E. R. G. and Livingood, J. N. B.
Method for Calculation of Laminar Heat Transfer in Air Flow Around Cylinders of Arbitrary Cross Section
NACA Report 1118, 1953

18. Eckert, E. R. G. et al
Measurement of Total Emissivity of Porous Materials in Use for Transpiration Cooling
Jet Propulsion, Vol. 26, No. 4, April 1956

19. Eckert, E. R. G. et al
Comparison of Effectiveness of Convection, Transpiration, and Film-Cooling Methods with Air as Coolant
NACA Report 1182, 1954

20. Eisenklam, P. and Hargreaves, C. M.
Flow Through Porous Materials. The Retardation of Liquid Flow Rates in Porous Materials. Part I
Min. of Supply PDGW Rep. EMR/52/2, 1952

21. Eisenklam, P.
Corrections for the Masking of Specimens used in Flow Experiments
Research, July 1952

22. Eisenklam, P.
The Passage of Liquids Through Consolidated Porous Media
Ph.D. Thesis, London University, 1954

23. Eisenklam, P.
The Retardation of Liquid Flow Rates Part II. The Effect of Gases Dissolved or Entrained in the Liquid
Min. of Supply DGGW Rep. EMR/55/6, May 1955

24. Friedman, J.
A Theoretical and Experimental Investigation of Rocket Motor Sweat Cooling
Journal of American Rocket Society No. 79, December 1949

25. Geery, E. L. et al
Experimental Studies on Heat Transfer and Fluid Flow Systems
AGC-1310-4, 1957, Aerojet General Corporation

26. Green, L. Jr.
Experimental Studies on Heat Transfer and Fluid-Flow Systems. Part II
A GC -AE -25
Aerojet General Corporation

27. Green, L. Jr. and Alan, K. L.
Heat Removal From a Resistance-Heated Porous Solid
A GC -1380, 1957
Aerojet General Corporation

28. Green, L. and Lemke, B. J.
Gas Cooling of a Porous Heat Source
Theoretical
NAA - SR - 163, 1951
Atom. Energ. Research Dept.
North American Aviation Inc.

29. Grootenhuis, P.
The Mechanism and Application of Effusion Cooling
The Journal of the Royal Aeronautical Society, Vol. 63, No. 578,
February 1959

30. Grootenhuis, P. et al
Heat Transfer to Air Passing Through Heated Porous Metals. General
Discussion on Heat Transfer
Proceedings of General Discussion on Heat Transfer
Institute of Mechanical Engineers, 1951

31. Hargreaves, C. M.
The Flow of Porous Media
M.Sc. Thesis, London University, 1952

32. Harned, M.
The Ramjet Powerplant
Aero Digest, July 1954

33. Hatch, L. P. and Isakoff, S.
Fluid Dynamics of Porous Systems
BNL-1106, Brookhaven National Laboratory

34. Hepper, R. H.
Designing for High-Speed Missile Cooling
Aero Digest, June 1956

35. Hsu, S. T.
Determination of Thermal Conductivities of Metals by Measuring Transient
Temperatures in Semi-Infinite Solids
Trans. of ASME, Vol. 79, No. 5, p. 1197, July 1957

36. Jakob, and Fieldhouse
Experimental and Theoretical Work on Transpiration Cooling
Heat Transfer
John Wiley & Sons, Inc., New York, Vol. II, p. 394

37. Kitchenside, A. W.
The Effects of Kinetic Heating on Aircraft Structures
Journal of the Royal Aeronautical Society, February 1958

38. Kay, J. M.
An Introduction to Fluid Mechanics and Heat Transfer
University Press, 1957

39. Klunker, E. B. and Ivey, H. R.
An Analysis of Supersonic Aerodynamic Heating with Continuous Fluid Injection
NACA Report 990, 1950

40. Klunker, E. B. and Ivey, H. R.
An Analysis of Supersonic Aerodynamic Heating with Continuous Fluid Injection
NACA TN 1987, 1949

41. Kovasznay, L.
Calibration and Measurement in Turbulence Research by the Hot-Wire Method
NACA TN 1130, June 1947

42. Libby, et al
An Experimental Investigation of the Isothermal Boundary Layer on a Porous Flat Plate
Journal of the Aeronautical Sciences, Vol. 19, p. 127, 1952

43. Locke, G. L.
Heat Transfer and Flow Friction Characteristics of Porous Solids
NP - 1757 (AEC Library)

44. Masson, D. J. and Gaxley, C.
Surface Protection and Cooling Systems for High Speed Flight
Aeronautical Engineering Review, November 1956

45. Mayer, E. and Bartus, J. G.
Transpiration Cooling in Porous Metal Walls
Jet Propulsion, November and December 1954

46. Mickley, H. S. et al
Heat, Mass, and Momentum Transfer for Flow Over a Flat Plate with Blowing or Suction
NACA TN 3208

47. Morduchow, M.
On Heat Transfer Over a Sweat-Cooled Surface in Laminar Compressible Flow with a Pressure Gradient
Journal of the Aeronautical Sciences, October 1952

48. Ness, N.
On the Temperature Distribution Along a Semi-Infinite Sweat-Cooled Plate
Journal of the Aeronautical Sciences, November 1952

49. Newman, G.
An Investigation of the Non-Adiabatic Flow of Fluids Through a Porous Material With Special Reference to Boiling Liquids.
Ph.D. Thesis, Imperial College, London University, 1958.

50. Norton, F. H. et al.
Progress Report on the Measurement of Thermal Conductivity of Refractory Materials.
United States Atomic Energy Commission, Mass. Inst. of Techn., 1953

51. Pierpont, P. K.
Investigation of Suction-Slot Shapes for Controlling a Turbulent Boundary Layer
NACA TN No. 1292, 1947

52. Ross, J. and Kraus, G.
On a Study of Porous Media by Means of Flow Methods
NP-4204 Progress Report No. 1, 1951

53. Rubesin, M. W., and Inouye, M.
A Theoretical Study of the Effect of Upstream Transpiration Cooling on the Heat-Transfer and Skin-Friction Characteristics of a Compressible Laminar Boundary Layer
NACA TN No. 3969, 1957

54. Rubesin, M. W. and Pappas, C. C.
An Analysis of the Turbulent Boundary-Layer Characteristics on a Flat Plate with Distributed Light-Gas Injection
NACA TN No. 4149, 1958

55. Rubesin, M. W. et al
An Analytical and Experimental Investigation of the Skin Friction of the Turbulent Boundary Layer on a Flat Plate at Supersonic Speeds
NACA TN No. 2305, 1951

56. Scheidegger, A.E.
The Physics of Flow Through Porous Media
University of Toronto Press, 1957

57. Schneider, J. P.
Conduction Heat Transfer
Addison Welsley Publishing Co., 1955

58. Stadler, J.
Heat Transfer to Bodies in a High Speed Rarefied Gas Stream
NACA TN No. 2438, 1952

59. Tsahonas, S. R.
Laminar Flow Through Granular Media
AD - 33957, 1953

60. Unteberg, W.
An Analysis of Heating Problems in Supersonic Ramjet Tailpipes
Jet Propulsion, May 1957

61. Weinbaum, S. and Wheeler, H. L.
Heat Transfer in Sweat-Cooled Porous Metals. Theoretical Considerations
Journal of Applied Physics, Vol. 20, p. 113, 1949

62. Weisberg, H. L.
Velocity and Pressure Distribution in Turbulent Pipe Flow with Uniform Wall Suction
Carbide and Carbon Chemicals Company, K-1187

63. Wolff, E. R.
The Development of a Mass Flow Probe
Aerophysics Laboratory, University of Toronto

64. Yates, E. C. Jr.
On the Permeability of Porous Materials
NACA TN 3596, 1956

65. Yuan, S. W. and Ness, N.
Heat Transfer in a Laminar Compressible Boundary Layer on a Porous Flat Plate with a Variable Fluid Injection
Project Squid., Tech. Memo PIB-15. Polytechnic Institute of Brooklyn

66. Yuan, S. W. and Chin, C.
Heat Transfer in a Laminar Boundary Layer on a Partially Sweat-Cooled Plate
Project Squid. Tech. Report No. 13, 1949, Polytechnic Institute of Brooklyn

67. Yuan, S. W.
A theoretical Investigation of the Temperature Field in the Laminar Boundary Layer on a Porous Flat Plate with Fluid Injection
Project Squid. Report No. 4, Polytechnic Institute of Brooklyn, 1947

68. Heat Transfer. A Bibliography of Unclassified Report Literature
U.S. Atomic Energy Commission, TID-3305, March 1957

69. Yuan, S. W.
Heat Transfer in Laminar Compressible Boundary Layer on a Porous Flat Plate with Fluid Injection
Journal of the Aeronautical Sciences, Vol. 16, No. 12, December 1949

70. Statistical Hydrodynamics in Porous Media
Journal of Appl. Phys. 25 (1954) 994

71. Beldecos, N. A., et al.
Hydraulic Aspects of Fluid Flow Through Packed and Flüidized Systems
WIAP-4, Westinghouse Electric Corporation, Industrial Atomic Power Group, October 1953.

72. Libby, P., Lew, H., and Romano, F.
On the Stability of a Laminar Compressible Boundary Layer Over a Flat Plate Subject to Uniform Suction and Injection.
PIBAL Report No. 133, Polytechnic Institute of Brooklyn, October 1948.

APPENDIX 1

DETAIL DESCRIPTION OF THE HEAT TRANSFER RIG

Air Supply

The main air was supplied by a Sturtevant Centrifugal Compressor, which was driven by a 10 HP, 3500 pm, 10 a, 550v, 60 cycle, 3 phase General Electric Induction motor. The fan was rated at 2 psig at 900 cfm, and was run at about 2330 pm. It exhausted into a duct 8 inches in diameter. Two 2 inch pipes branched out from the main duct. One, fitted with a 2 inch gate valve, served as a by-pass to let out air when the main line was almost shut off. The other line supplied the primary air for combustion. Further in the main duct there was a butterfly valve driven by a 22v, 60 cycle, 24 watt Modutrol motor. The motor was supplied by 115v a.c. current fed through a 60 cycle 115v to 25v Hammond transformer, and was controlled by a potentiometer and an on-off switch. A 0.309 inch ID orifice plate was used to measure the main flow. Two Iron-Constantan thermocouples were used to measure the air temperature. One was located just before the orifice and the other before the combustion chamber entrance. The primary-air line was fitted with an Iron-Constantan thermocouple, a 1,1875 inch ID orifice plate, and a 2 inch globe valve. The pressure drops in the orifices were read on glass manometers filled with dyed water. The absolute pressures in the main-air and the primary-air lines were read on bourdon-type pressure gauges with ranges of 0 to 30 and 0 to 15 psig respectively. The manometers were connected to the pressure taps by ¼ inch plastic tubing and the pressure gauges were connected to the pressure taps by ¼ inch copper tubing. See Figure 5 for a schematic diagram of the apparatus, and Figure 6 for a photograph of the rig.

The cooling air was supplied at about 110 psig from the Laboratory high pressure air supply. The air was bled off from the main line by a 2 inch gate valve at its beginning. A 1.25 inch ID orifice plate was located in this line. The air was then led to a gate valve located in the instrument pannel, and then by a 1 inch pipe to a Cuno Micro-Klean Air Line Filter. Although a simple filter was designed for this rig, the use of the Cuno Filter was decided upon because of its ability to remove from the air microscopic dirt particles. This was important in this experiment because of the danger of blockage of the porous bronze plate. From the filter the air entered the coolant manifold, made of a 3 inches in diameter and 12 inch long cylinder, and then through three lines with pressure regulators and orifice plates it entered the coolant duct. The $\frac{1}{2}$ inch line leading to the first coolant compartment in the test duct and the other two 3/8 inch lines leading to the second and third compartments had 0.225 inch ID orifice plates. Before entering the test section the air was led by 3/8 inch copper tubing through pressure reducing valves installed in the instrument pannel. Two Iron-Constantan thermocouples, one installed in front of the first orifice and the other in the coolant manifold, measured the air temperature. The first orifice was not used because a high pressure manometer could not be obtained. The pressure drops across the other three orifices were read on glass-tube manometers, since the air pressure at these orifices was reduced to 30 psig. The pressure tubes were connected to the manometers by 1/8 inch copper tubing. The coolant pressure at entry was read on a 0 to 160 psig pressure gauge, and at the three functioning orifices by three 0 to 60 psig gauges.

Combustion Chamber

The propane used for combustion was supplied from a bank of compressed propane bottles. The propane pressure from the supply line was reduced to 20 psig by a $\frac{1}{2}$ inch by $\frac{1}{2}$ inch propane regulator. The propane then passed through a 5/32 inch ID orifice plate, which was located in a 1 inch pipe, a propane valve, and a second propane regulator. Part of the propane flow was then bled off by a $\frac{1}{4}$ inch copper tubing and passed through a needle valve, a solenoid gas valve and a shut-off cock to feed the pilot flame. The main propane flow was led to the combustion chamber by way of a safety shut-off valve.(see Fig. 7). All the control devices, except the first regulator and the shut-off cock, were located on the instrument pannel. The orifice pressure drop was measured on a water-filled glass-tube manometer. Propane pressure was measured before the orifice and after the second regulator by 0 to 200 psig and 0 to 30 psig pressure gauges respectively. An Iron-Constantan thermocouple measured propane temperature at entry to the orifice.

The combustion chamber was made of a duct 8 inches in diameter with a conical perforated stainless steel flame tube. The cone was 24 inches long, and 4 inches in diameter at one end and 7 inches in diameter at the other end. The main air entered the combustion chamber at right angles. The primary air after having mixed with the main propane stream in the Series 52 HG - 200 Maxon mixing tube entered the Maxon Pilotpak 2 -24 burner nozzle. The nozzle was attached to a flange which fitted over the entrance to the combustion chamber. A movable plug was fitted in the nozzle to restrict the nozzle throat area and thus increase the lower range of operation of the burner. The flame tube was held concentric and in the right axial location by being attached by means of three legs to an annular disk which fitted between the above-mentioned flange and the combustion chamber. The burner nozzle had an outlet of the pilot line, a spark plug, and a flame rod (see fig. 8). The insulated electrical lines from the spark plug and the flame rod were led out through two holes in the flange. The voltage in the spark plug line was boosted by a 110v to 1000v transformer.

The combustion equipment was controlled by a Honeywell R 485A Combustion Control. This control equipment was connected to the 110v ac supply, start-stop push button switch, solenoid valve, mercury switch safety shut-off valve, spark plug transformer, and the flame rod. The mercury switch was installed at the main fan exit and was intended to break the electrical current to the control equipment as soon as the main air fan failed and the air delivery pressure fell. Unfortunately, this type of switch did not function properly and another, more sensitive one, was not available. When the ignition button was pressed, the Combustion Control opened the solenoid valve in the pilot line and injected some propane into the burner nozzle. At the same time the spark plug was actuated and thus the pilot flame was established. If the flame did not light up and the flame rod was not enveloped by a flame, which completed the flame rod's circuit, the solenoid valve would be shut off. If the flame held, the air was then introduced slowly and the propane safety shut-off valve opened, and the combustion chamber was in operation.

At the exit from the combustion section there was a 36 inch long stainless steel duct. The entrance of this duct was filled with 8 inches long, $\frac{3}{4}$ inch in diameter stainless steel tubes, which acted as flow straighteners. The pressure drop from the mixing tube to the combustion chamber was measured on a manometer, and the combustion chamber exit temperature was measured by a Chromel-Alumel thermocouple. Both the combustion chamber and the following section were insulated by 1 inch thick Magnesia insulation (see fig. 9). Copper gaskets were used between the combustion chamber and the following section, and at the entrance to the test section.

Test Section

At the entrance to the test section was a 2 inch long stainless steel nozzle, which was designed according to the British Standard Code on Flow Measurement. The nozzle reduced the flow from the 8 inch duct to the 2 inch wide by 3 inch high test duct. The gasket between the test duct and the nozzle was made of 1/16 inch thick Asbestos sheet packing. It was covered with aluminum foil and was wrapped with fibre glass insulation.

The test duct was $17\frac{1}{4}$ inches long. The two vertical walls of the test duct were made of $5\frac{3}{4}$ inches wide, 17 inches long steel frames, which had 3 inch by 12 inch windows (see fig. 10 for the cross-sectional view of the duct). Above and below the window the frames had 1 inch wide, $\frac{1}{4}$ inch thick, and 17 inches long steel strips bolted to the faces of the duct facing each other. One frame had the coolant duct brazed on the outside to cover the window. The top and bottom of the duct were made of stainless steel slabs which held between them, on one side the Pyrex glass window and spacing slabs, and on the coolant duct side the porous wall and spacing slabs. The steel strips on the side frames had their edges, which held the stainless steel slabs, cut at an angle, so that when the bolts holding the two side frames together were tightened, the stainless steel slabs pressed on the porous wall and the Pyrex glass window forming a leak-proof duct. Both the side frames and the horizontal walls had $\frac{1}{4}$ inch thick steel pieces welded to them to form flanges at each end, when the duct was assembled. Asbestos sheet packing 1/64, 1/32, and 1/16 inch thick, was used between the bearing surfaces to give tight seals. This packing could withstand 1000°F. When the duct was assembled, the ends were machined on a shaper to give smooth surfaces. At the entrance to the duct a 1/16 inch thick asbestos gasket and a $\frac{1}{4}$ inch thick steel flange were clamped to the duct flange, and holes were drilled through the outer flange into the duct walls. The holes were then tapped and screws inserted into them. This was done to insure that the longitudinal members of the duct did not slide with respect to each other and to give the duct more rigidity.

The Pyrex window was 0.22 inch thick, 3.25 inch wide, and 12.5 inch long. It was held against the frame by the flanges on the horizontal walls (see fig. 10).

Thin Asbestos gaskets were used at faces of contact of the glass and the steel. Since Pyrex does not soften below 1500°F, it was sufficient for this application. Forward of the Pyrex slab and held in a similar way was a $\frac{1}{4}$ inch by 2.5 inch by 3 inch stainless steel spacer. Behind the slab was another spacer whose dimensions were $\frac{1}{4}$ inch by 1.5 inch by 3 inch. During testing the outside of the Pyrex window was covered by very highly polished copper plates to reduce the heat radiation from the test wall.

The test specimen was held in position in the same way as the Pyrex window. In addition at each end it had flanges (see fig. 11), 1/16 inch wide, which pressed against similar flanges on $\frac{1}{2}$ inch thick steel spacers on each side of the porous wall. The spacer closer to the duct entrance had a $\frac{1}{4}$ inch wide and 3 inch high vertical slot cut in it. The slot, whose purpose was to remove the boundary layer from the beginning of the porous wall, was located $\frac{1}{4}$ inch from the beginning of the test specimen, and was connected to the outside of the test section by a duct brazed to the side wall. This duct was connected to a suction fan. All the inside test duct surfaces had a mirror polish to reduce the radiant heat transfer to a minimum. Silver plating would have been more effective but since sulphur was present in the combustion gasses the silver would have been corroded.

The coolant duct was made of 1/16 inch thick sheet metal brazed to the side of the test duct. The cross-section of the coolant duct is shown in Figure 10. It was devided into 3 compartments to give the coolant injection velocity which varied approximately as the inverse square root of the distance from the leading edge of the test wall. The first compartment was 2.031 inches by 3 inches, the second was 4 inches by 3 inches, and the third was 5.969 inches by 3 inches. To smooth out the coolant flow, two fine-mesh stainless steel screens were installed in each compartment. To prevent leakage from one duct to another, the edges of walls separating the compartments and bearing on the porous wall surface were made knife-edge sharp. To prevent corrosion and to reduce the radiant heat transfer, the inside walls of the coolant duct were painted with high temperature aluminum paint.

Each coolant duct had a static pressure tap, a movable Iron-Constantan thermocouple, and a connection which was pressure-tight and through which the thermocouple leads from the test wall could be led out. The static pressures were read on three 0 to 100 psig range high precision Laboratory Test Gauges. The test duct had three static pressure taps in the floor at distances of 2.66, 8.58, and 14.57 inches from the beginning of the duct. The pressures were read on water-filled manometers. Chromel-Alumel thermocouples were imbedded in the floor at 2.53, 8.46, and 14.66 inches from the duct entrance. A movable, shielded Chromel-Alumel thermocouple (see fig. 12) was installed in the duct 1.625 inches from the duct entrance. Five movable pitot and Chromel-Alumel thermocouple probes (see fig. 13) were located just above the Pyrex window and at 0.09, 1.1, 4.05, 9.0, and 12.05 inches from the beginning of the test wall, which was 1.625 inches from the duct entrance. The pitot probe opening was 1.6 inches from the ceiling and the thermocouple about 1.5 inches. The pitot probe was made of 0.008 inch ID and 0.016 inch OD, $\frac{1}{4}$ inch long stainless steel tubing silver-soldered to a 0.042 inch OD stainless steel tubing which was soldered to 0.125 inch OD stainless steel tubing. Side by side with the pitot probe was a Chromel-Alumel thermocouple whose wires were sheathed in a 0.042 inch tubing. Outside the duct the 0.125 inch tubing was joined to a 0.25 inch OD stainless steel tubing from which the pressure line and the thermocouple leads were separated by means of a brass "T" connection brazed to the 0.25 inch tubing. The silver solder used in the manufacture of these probes could withstand a temperature of 2000°F. Since the pitot probe was made of such small diameter tubing, there was a great deal of trouble with dirt particles blocking its entrance. These probes were calibrated against a standard probe.

Test Specimen

The sintered porous bronze test wall was manufactured by the Sheepbridge Engineering (Canada) Limited, in Guelph. Although three pieces of different porosities and powder size were made, only one was tested because of time limitation. The test specimen was made of 90 per cent Copper and 10 per cent Tin bronze powder of 60 to 80 mesh size. This powder was sprinkled in a mold, pressed cold, and then sintered in an oven. The slab used in the tests had a porosity of 41.4 per cent, very fine texture and one very smooth surface.

The bronze slab was machined on a shaper to the required dimensions (see fig. 11). It had 4 Iron-Constantan thermocouples soldered in 1/16 inch by 1/16 inch by $\frac{1}{4}$ inch grooves in the side facing the coolant duct at 1, 4, 7, and 9 inches from the leading edge. The first three thermocouples were located in centres of the coolant compartments. In order to measure the temperature inside the porous wall, four Chromel-Alumel thermocouples, sheathed in 0.042 inch OD stainless steel tubing, were placed from the top edge of the wall into small holes, about 1 1/32 inches deep, and forced in contact with the metal. The holes were drilled at 0.10 inch intervals and at 3.625, 3.795, 4.125 inches from the leading edge of the test wall.

Suction and Exhaust Systems

The gas sucked out from the test duct passed through a 1 inch line which had a 1 inch gate valve and cooled in a 4 inches OD duct, was blown into the exhaust duct by a General Electric Turbosupercharger Model 7S-B31-A2. The fan was driven at 3900 pm by a 3 HP, 1735 pm, 3.5a, 550v, 60 cycle, 3 phase, Type AD English Electric motor.

The exhaust system consisted of a 12 inch long diffuser, and an 8 inch OD duct, which joined into the Laboratory exhaust system. The diffuser, made of mild steel, provided a smooth transition from the 2 inches by 3 inches test duct to the exhaust duct. The exhaust duct had a butterfly valve in it, so that it could be closed when the rig was not in operation, and the exhaust gasses from the Laboratory exhaust system tended to flow into the rig.

Instrumentation

The Iron Constantan and the Chromel-Alumel thermocouples were connected to two selection switches and were read on a Honeywell Brown Electronic Potentiometer which had two ranges and was self-balancing (see fig. 14). The pitot probe total head pressures were read on a micromanometer filled with alcohol. The two traversing gears used were driven by 24v dc motors. One traversing gear, operating the shielded thermocouple at the duct entry, was bolted to the test duct. The other, operating the probes on the side of the duct, could be mounted at five different positions on a rail and attached to any one probe. The distance travelled was measured by a finely divided scale on the first traversing gear, and by Ames Dial Gauge on the other. The direction of travel of the traversing gears was reversed by a double pole single throw switch.

The temperature of the porous wall in the test duct was measured by a Siemens Ardonox Radiation Pyrometer, which was mounted on a rail and could be moved parallel to the test duct (see fig. 15). The Ardonox was a very sensitive instrument, which focused radiation energy from the test specimen by a concave mirror coated by vapourized aluminum. A 23-element thermopile consisting of Nickel Chrome-Constantan thermocouples was used as the radiation receiver. A thin plastic foil highly permeable to infrared radiation sealed the housing of the instrument and protected the mirror and the radiation receiver from dust. For eliminating the influence of the housing temperature on the test specimen temperature reading, a temperature-sensitive resistor preventing the slope of voltage versus temperature characteristic from varying was connected in parallel with the radiation receiver. In addition, a balancing circuit was used for temperature measurements ranging up to 930 F. This circuit consisted of a dc bridge with a temperature-sensitive resistor. The required parallel shifting of the characteristic was caused by this circuit.

For the temperature measurement in the range of 200 to 1000°F a Photoelectric Amplifier was required. An available dc amplifier was tried but it was not sensitive enough and did not give satisfactory results. Next a dc microvoltmeter was tried, but it was unsatisfactory. Finally, two galvanometers were used, and the Ardonox had to be calibrated.

The dc power to the Ardonox was supplied by a Kepco Labs Power Supply Model 5C - 18 - 4M. The Ardonox required a very steady dc supply and the above unit perfomed the requirement perfectly. The 15 dc input to the Ardonox was passed through a Heath Company Resistance box to obtain the required 1.22 - o.22 ma current. This current was checked frequently during tests by a Winston Model 328 milliameter. The output from the Ardonox was connected to the galvanometers. A 0 - 10 mv Rubicon Galvanometer, supplied by 6v dc Heath Kit Battery Eliminator, was used for the low temperature range. A 0 -100mv G.E. Galvanometer, supplied by 110v ac was used for the high temperature range. The input to this galvanometer was passed through a 5 watt 500 ohm Howlett Pachard Voltage Attenuator. When one galvanometer was in use, the other was shorted out. All connections were made with shielded wires to prevent interference from stray emfs.(see fig. 16).

To calibrate the Ardonox, a solid bronze plate, of the same composition as that of the test specimen, was installed in the duct. The calibration plate had nine thermocouples fitted in holes drilled from the coolant duct side to within 1/32 inch of the hot surface. The calibration covered a range of temperatures and mass flows which were used in the tests. A great deal of time was spent on this calibration because of difficulty in getting the Ardonox subsidiary equipment to work properly.

APPENDIX 2

OPERATIONAL PROCEDURE FOR THE HEAT TRANSFER TESTS

The following procedure was followed in the operation of the heat transfer rig: 1) the Honeywell Brown Potentiometer was turned on to allow it to warm up; 2) the Ardonox dc power supply and the Battery Eliminator were switched on; 3) the exhaust duct butterfly valve was opened and the switches on the main air and suction fans were turned on; 4) the cooling air valves were opened; 5) the main air flow was set to a very low value; 6) the switch in the combustion control equipment circuit was turned on to allow at least 60 seconds for the warming up of the Honeywell Control; 7) the propane pressure behind the second regulator was set at 4 psig and both the needle valve and the shut-off cock in the pilot line were partly opened; 8) the Potentiometer was set on the Chromel-Alumel range and the selection switch set to connect the combustion chamber thermocouple with the Potentiometer; 9) the manometers and the galvanometers were zeroed; 10) the ignition button was pressed, and if the combustion chamber thermocouple indicated a temperature rise, the propane flow was increased; 11) the air and coolant flows were set at the required values; 12) the main propane safety shut-off valve was opened and the propane flow was adjusted to give the desired test duct inlet temperature; 13) about an hour was allowed for the temperature of the test wall to stabilize.

After the test specimen temperature remained constant for about 5 to 10 minutes, the first pitot probe was used to check the boundary-layer thickness at the leading edge of the test wall. The following values were then recorded: 1) temperatures, pressures, and orifice pressure drops of the air, coolant, and propane; 2) test duct floor temperatures and pressures;

3) test wall temperatures; 4) coolant duct temperatures; 5) room temperature and pressure; 6) temperature and total head pressure at increasing distances from the test wall. In order not to interfere with the flow during traversing by one probe, the other probes were withdrawn and hidden in the test duct ceiling, which had slots milled in it for this purpose. Because of their construction, the pitot probes could not be brought closer than 0.060 inch from the wall, but the thermocouples were bent to be about .030 inch closer to the test wall.

When testing was stopped, the propane valves were closed. Then, after the duct had cooled sufficiently, the air fans and valves, the Potentiometer, the Ardonox, and the galvanometers were closed.

APPENDIX 3

Test Results

Run No.	U_1 ft/sec.	T_1 °R	v_o ft/sec.	k_m Btu/hr. ft. °F	$h' \times 10^{-5}$ Btu / hr. ft^2 °F ft^3	h Btu / hr. ft^2 °F	h_c* Btu / hr. ft^2 °F
Distance from Leading Edge of Plate = 4.06 in.							
3	59.3	578	0.237	2.54		5.77	11.37
4	66.5	586	0.237	3.04		7.95	11.23
5	70.2	581	0.237	2.96		9.83	12.95
6	77.0	594	0.237	4.17		12.05	13.82
7	61.1	665	0.237	3.07	1.49	7.67	9.61
8	68.8	662	0.237	3.43		9.57	11.18
9	68.6	751	0.237	2.78		6.43	11.56
10	76.7	665	0.237	3.05	1.73	10.97	12.60
11	85.2	663	0.237	3.18		12.12	13.19
12	76.7	748	0.237	2.94		9.04	12.28
13	85.2	736	0.237	3.1		10.21	14.0
15	78.4	910	0.237	2.77		6.95	11.72
17	60.7	584	0.551	5.76		4.00	11.84
18	68.7	591	0.551	4.83		5.30	12.83
19	77.0	585	0.551	5.34		9.37	14.17
20	80.4	580	0.551	5.60	1.62	11.68	14.83
21	67.3	663	0.551	5.50	2.44	3.46	13.23
22	77.0	676	0.551	5.56	3.75	5.78	14.47
23	83.4	666	0.551	5.54	3.14	8.50	14.38
25	74.1	748	0.551	5.50		3.92	11.10
26	88.1	760	0.551	5.55		7.13	13.95
27	91.8	756	0.551	5.62	4.015	8.50	14.50

Run No.	U_1 ft/sec.	T_1 °R	v_0 ft/sec.	k_m Btu/hr. ft. °F	$h' \times 10^{-5}$ Btu / hr. ft.² °F ft.³	h Btu / hr ft.² °F	h_c* Btu / hr. ft.² °F
28	85.8	923	0.551	5.53		4.14	12.43
29	97.8	938	0.551	5.65		6.96	13.73
30	103.6	753	0.551	5.67		10.30	14.89
31	65.3	581	0.812	7.17		3.39	12.73
32	73.0	581	0.812	7.34		5.06	13.91
33	79.7	586	0.812	6.67		6.35	14.88
34	85.3	578	0.812	8.09		3.12	15.80
35	72.0	664	0.812	8.32		3.60	12.80
36	81.2	673	0.812	8.51		4.48	14.23
37	88.1	674	0.812	7.93		6.60	14.83
38	96.1	670	0.812	7.95	5.17	9.99	15.74
39	78.1	753	0.812	8.06	3.69	3.07	12.70
40	86.7	760	0.812	7.79		4.22	13.73
41	97.6	759	0.812	7.81		7.42	15.23
42	95.5	996	0.812	7.78		3.85	13.02
43	102.3	932	0.812	8.00		6.31	14.38
44	110.3	908	0.812	8.19		6.52	16.23
Distance from Leading Edge of Plate = 9.00 inches							
46	65.4	578	0.576	4.92		4.48	10.87
47	79.6	578	0.576	4.70		9.84	12.73
48	76.6	733	0.576	4.91		3.53	11.03
49	96.3	751	0.576	4.80		8.6	12.92
50	92.2	751	0.390	3.38		10.21	12.45
51	74.5	742	0.390	3.59		5.7	10.61
52	63.4	579	0.390	3.37		10.09	10.75
53	69.9	577	0.390	3.32		9.25	11.42
54	75.7	578	0.390	3.31		13.38	12.27
55	80.7	578	0.390	3.31		13.38	12.92
56	62.2	659	0.390	3.30		4.99	10.92
57	84.6	666	0.390	3.37		10.37	10.40
58	60.8	580	0.168	1.42		6.33	10.22

Run No.	U_1 ft/sec.	T_1 °R	v_o ft/sec.	k_m Btu/hr. ft. °F	$h' \times 10^{-5}$ $\frac{\text{Btu}}{\text{hr. ft}^2\ °\text{F ft}^3}$	h $\frac{\text{Btu}}{\text{hr. ft}^2\ °\text{F}}$	h_c* $\frac{\text{Btu}}{\text{hr. ft}^2\ °\text{F}}$
59	73.4	586	0.168	1.56		8.80	11.80
60	65.8	661	0.168	1.51		6.31	10.42
61	82.7	668	0.168	1.60		10.75	12.08

<u>Note</u> * h_c is calculated from: $N_{ux} = .0265\, R_{ex}^{\,.8}\, P_r^{\,.3}$

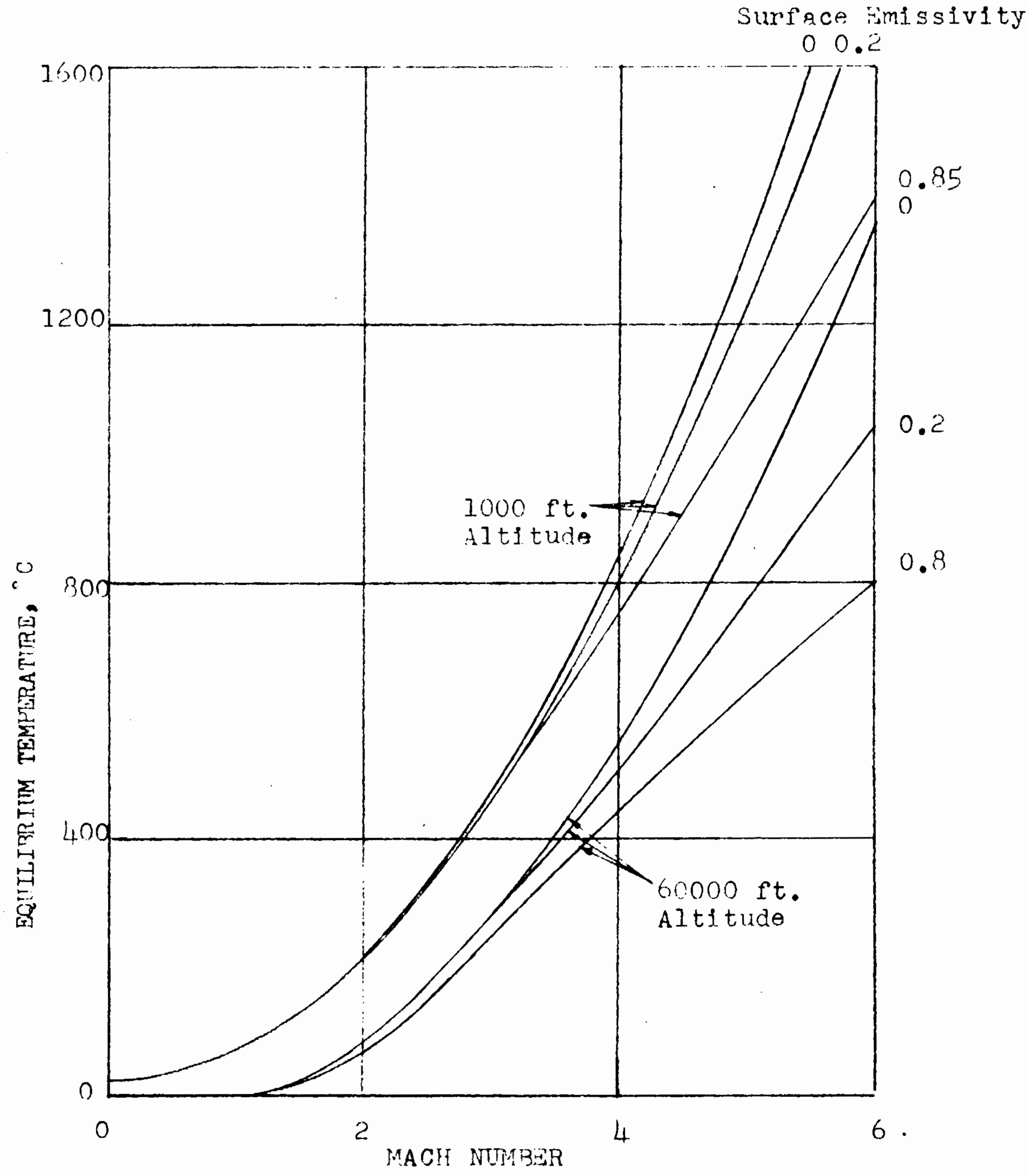

(from ref. 37)

FIGURE 1. KINETIC HEATING EFFECT

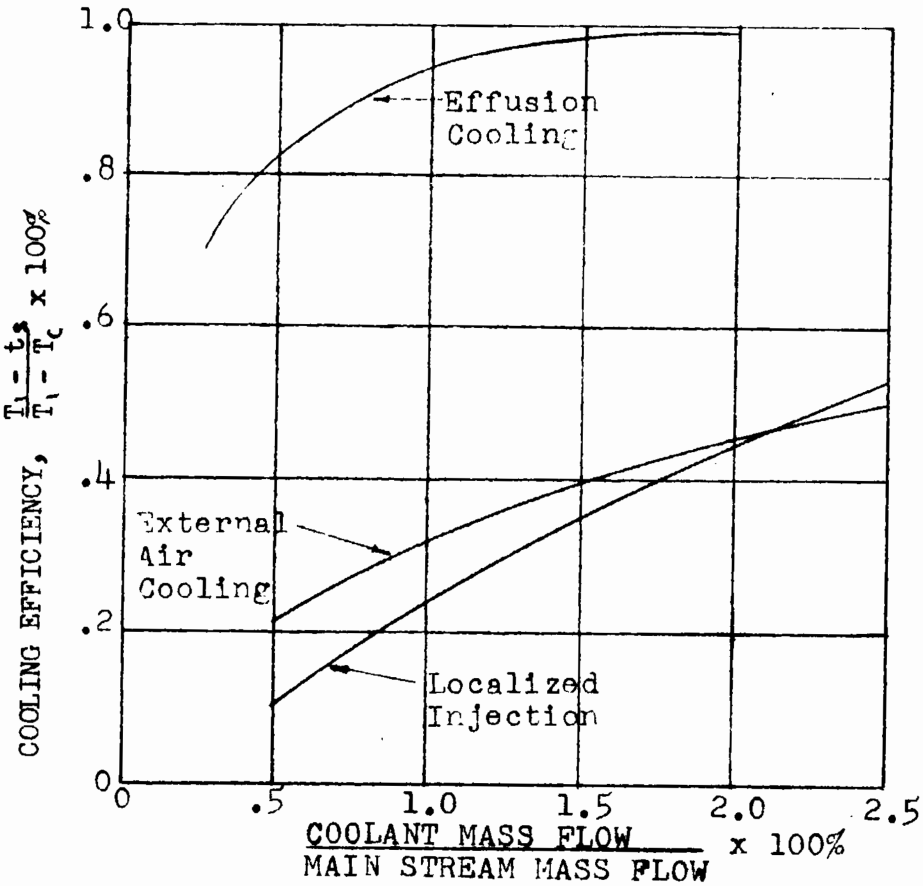

(from ref. 29)

FIGURE 2. COMPARISON OF COOLING METHODS IN COOLING COMBUSTION CHAMBER LINER

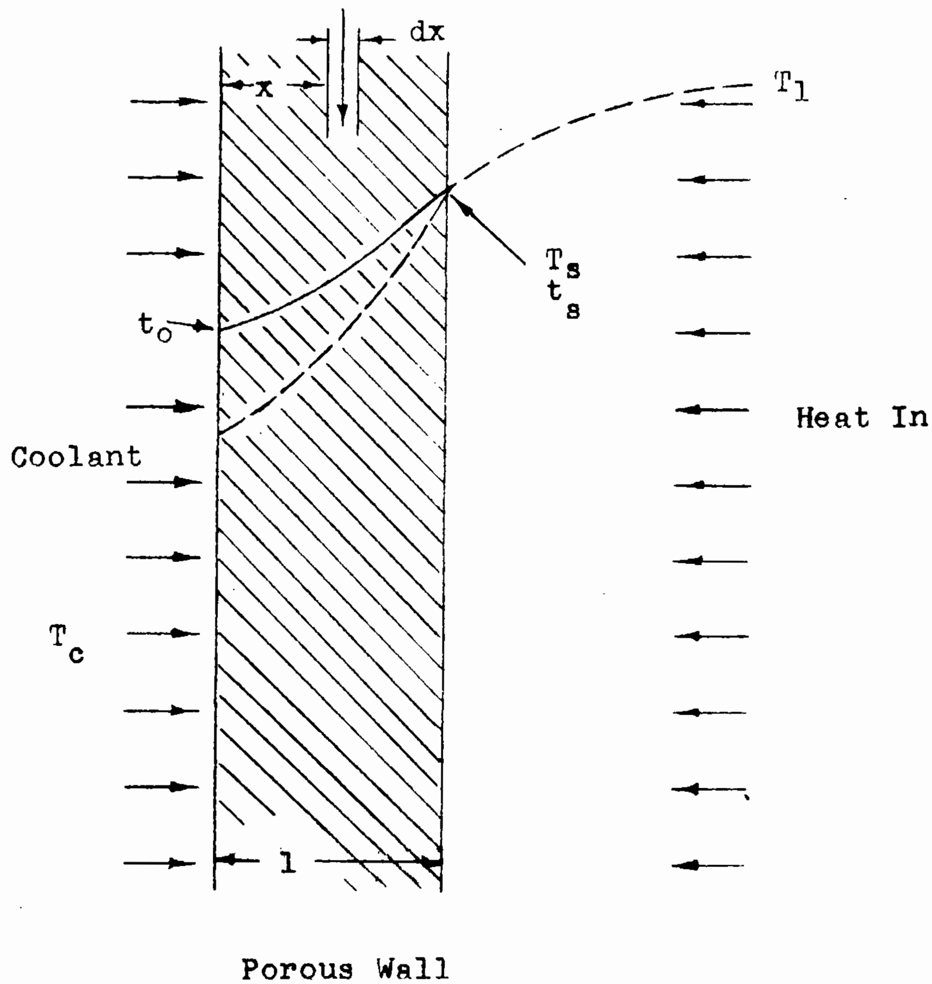

FIGURE 3. TEMPERATURE DISTRIBUTION IN A TRANSPIRATION COOLED WALL

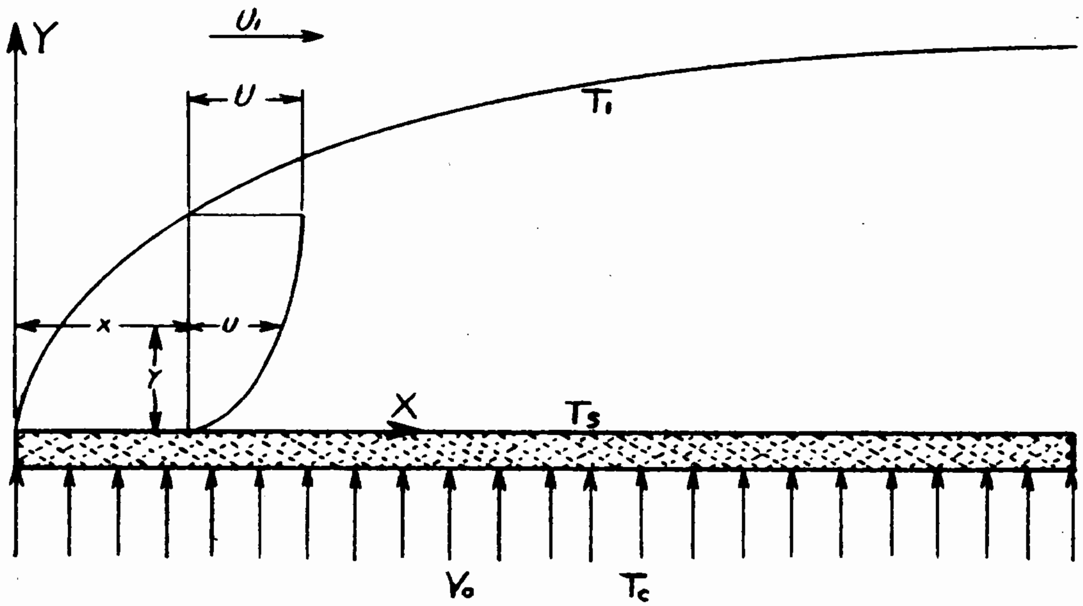

FIGURE 4. BOUNDARY LAYER ON A TRANSPIRATION COOLED POROUS WALL

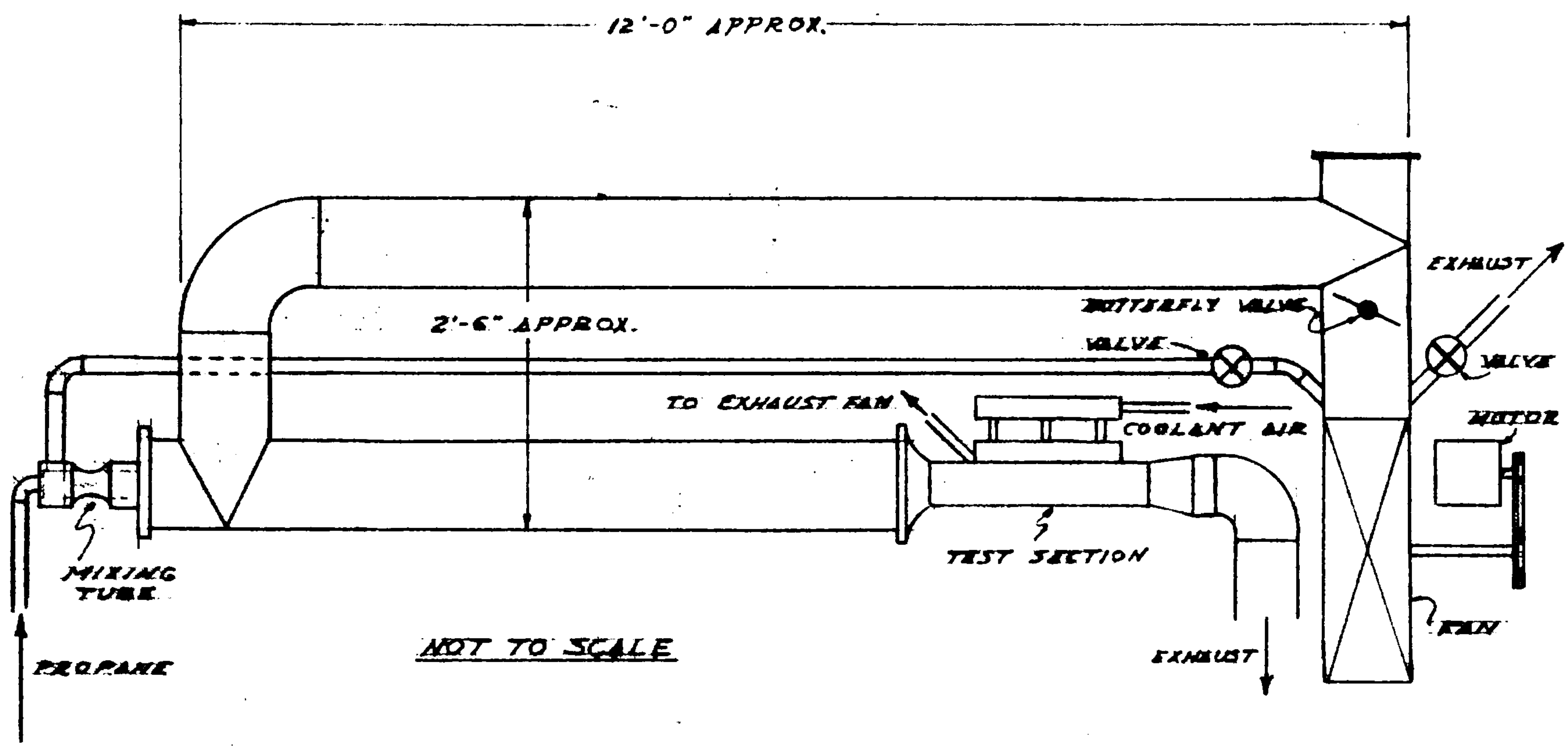

FIGURE 5. SCHEMATIC DIAGRAM OF HEAT TRANSFER RIG

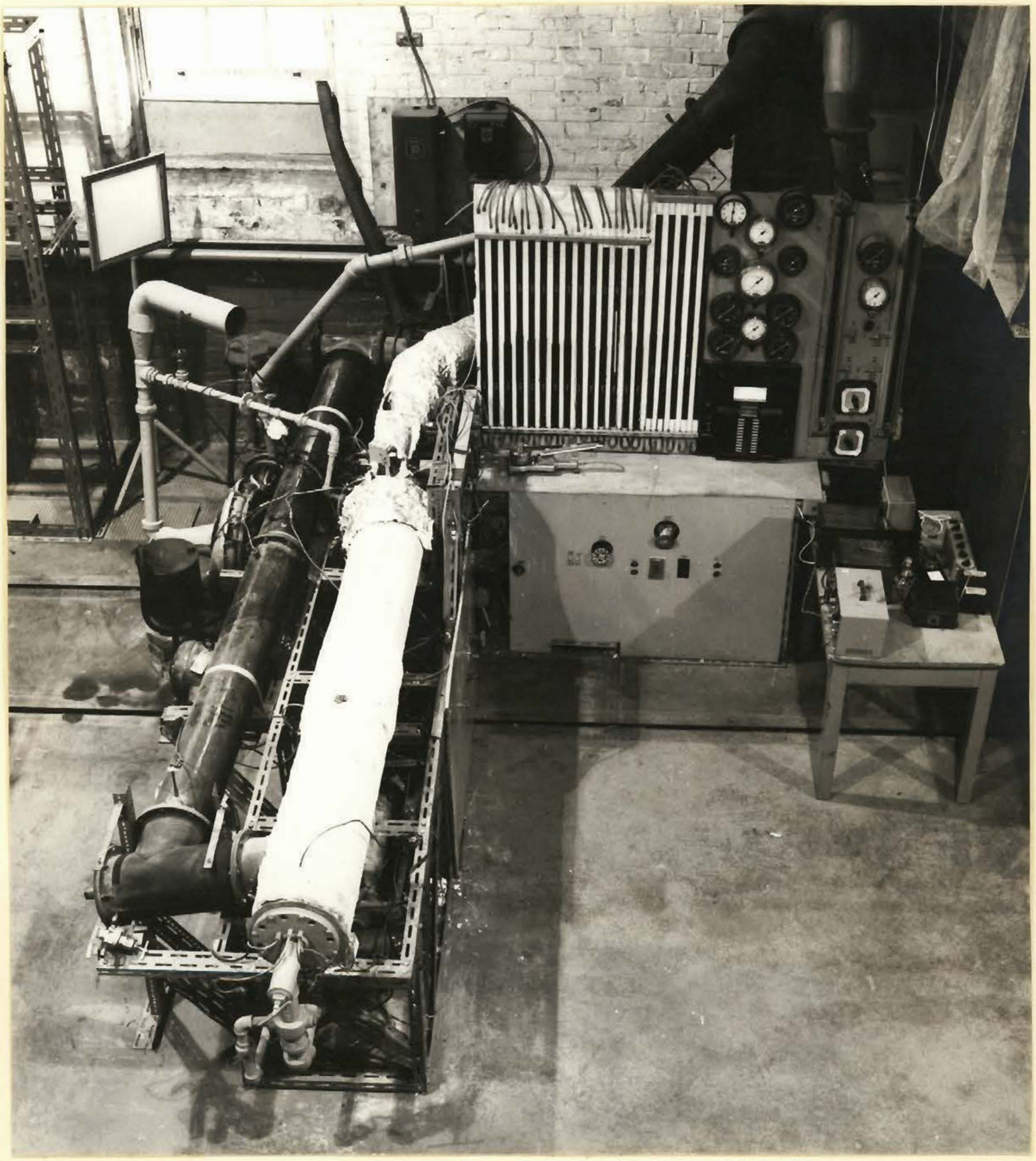

FIGURE 6. HEAT TRANSFER RIG

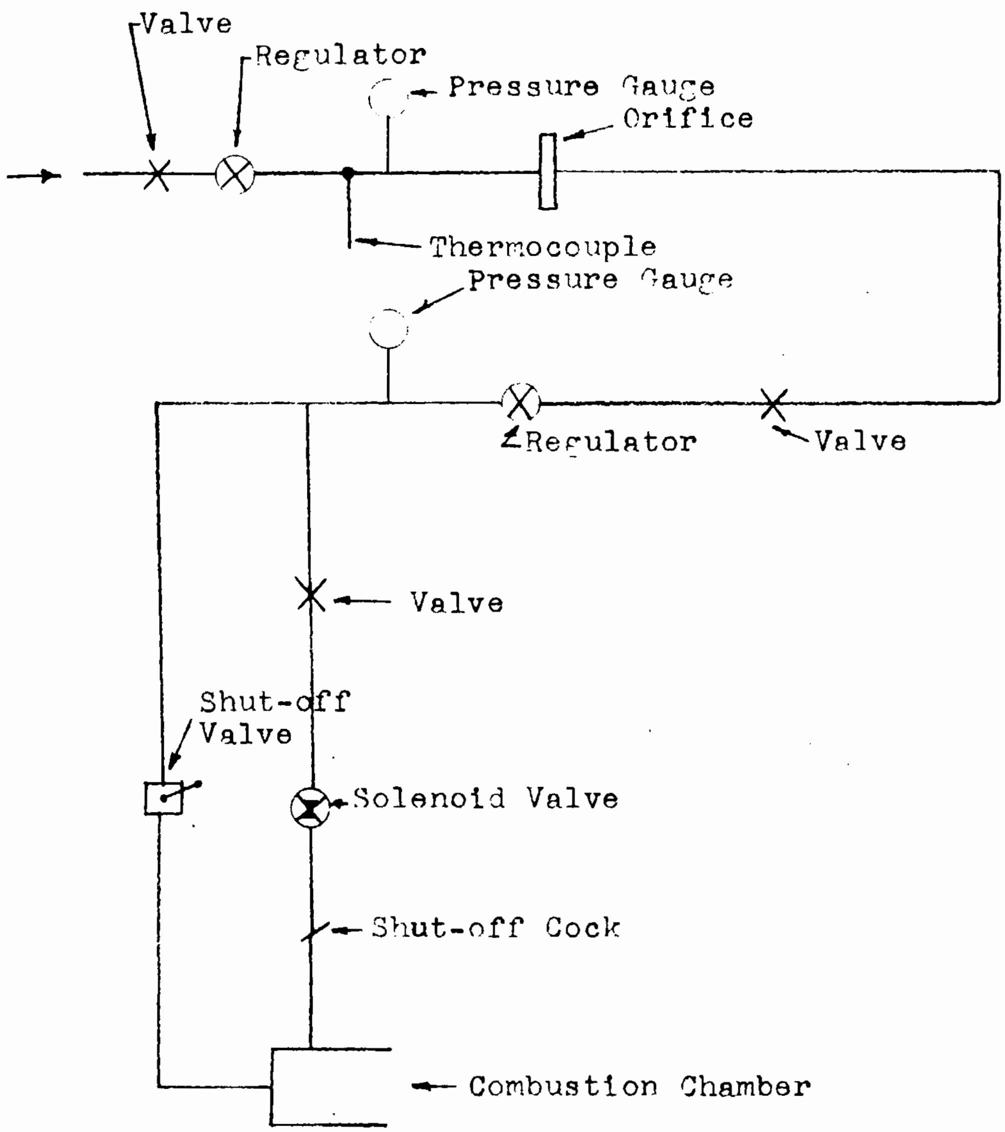

FIGURE 7. PROPANE LINE

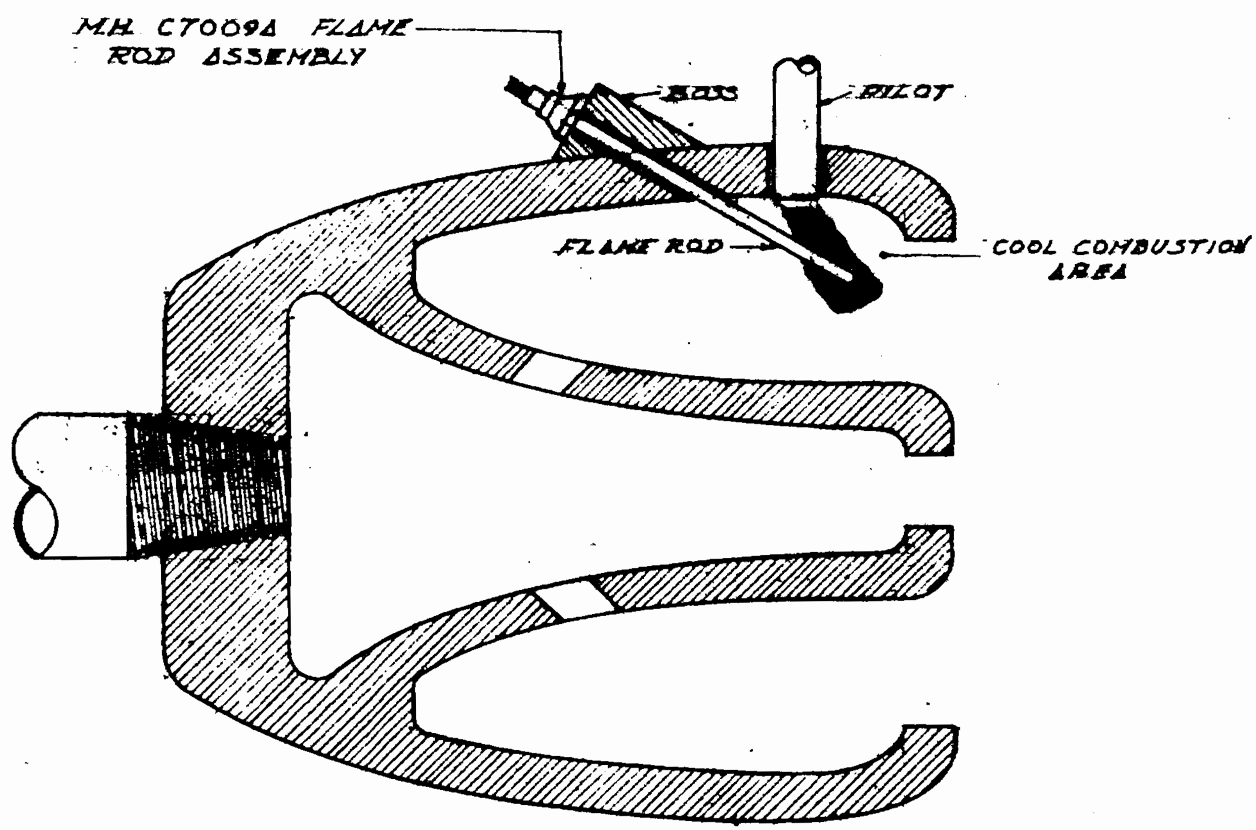

FIGURE 8. BURNER NOZZLE

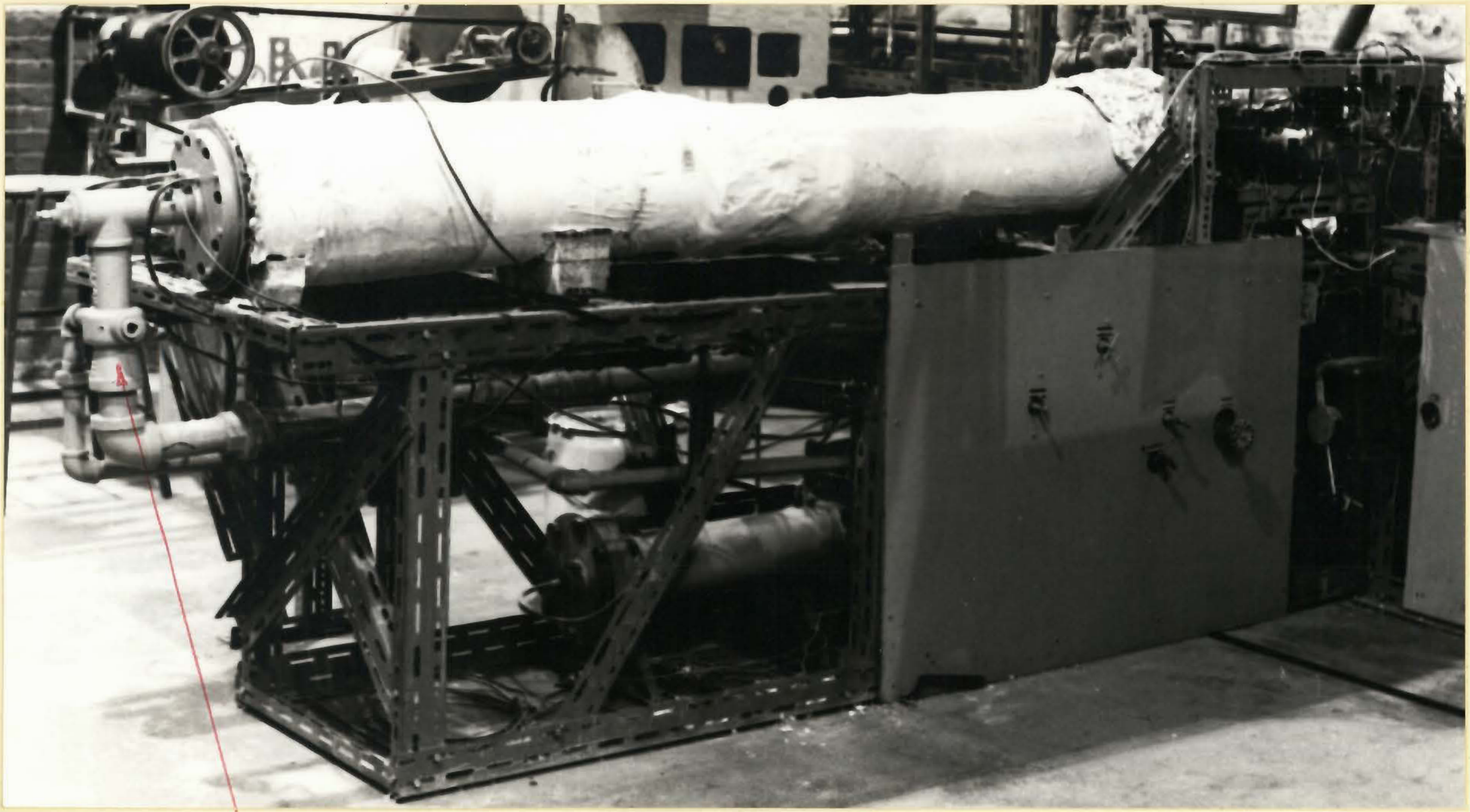

Mixing Nozzle

FIGURE 9. COMBUSTION CHAMBER

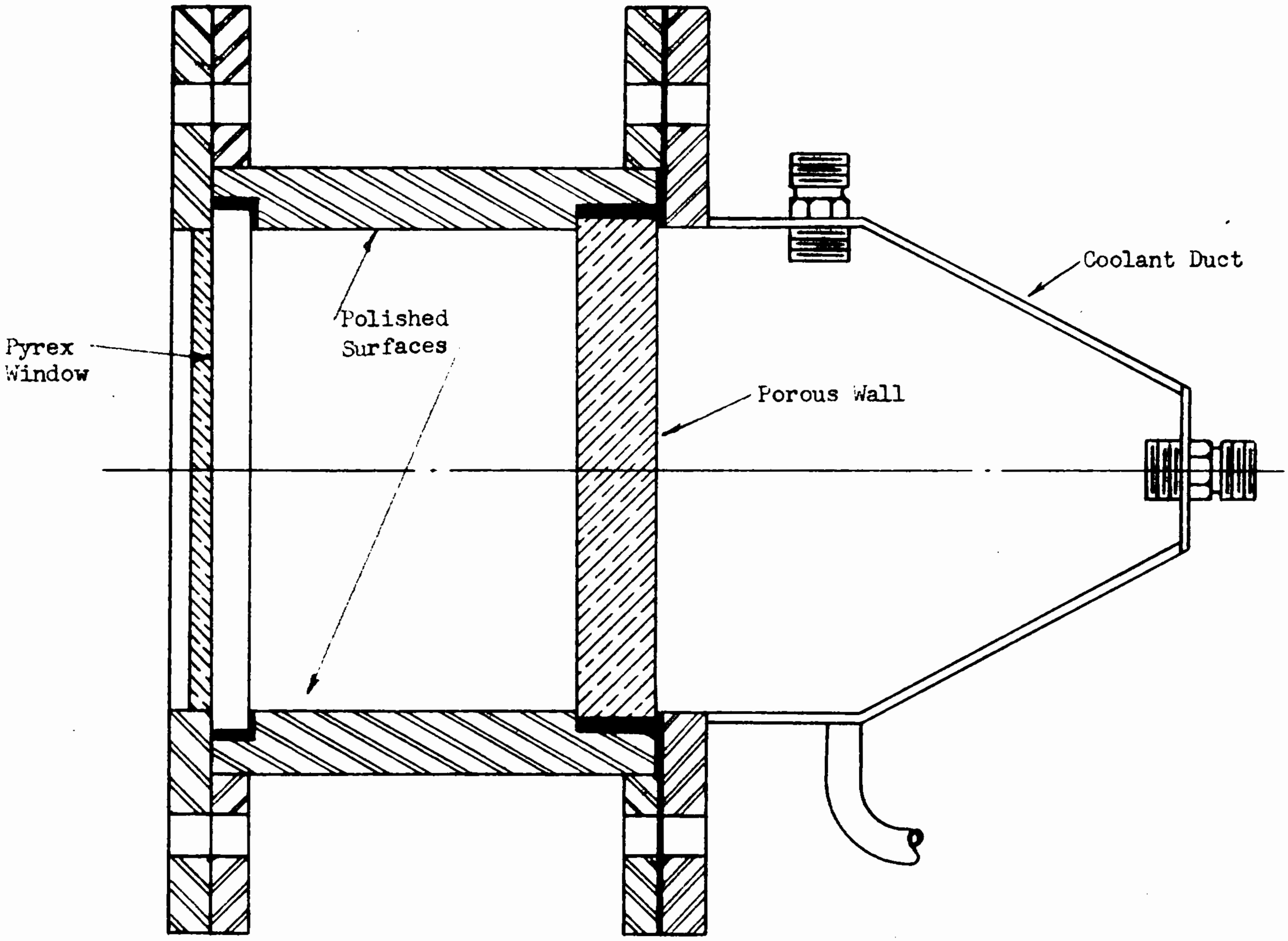

FIGURE 10. CROSS-SECTION OF TEST DUCT

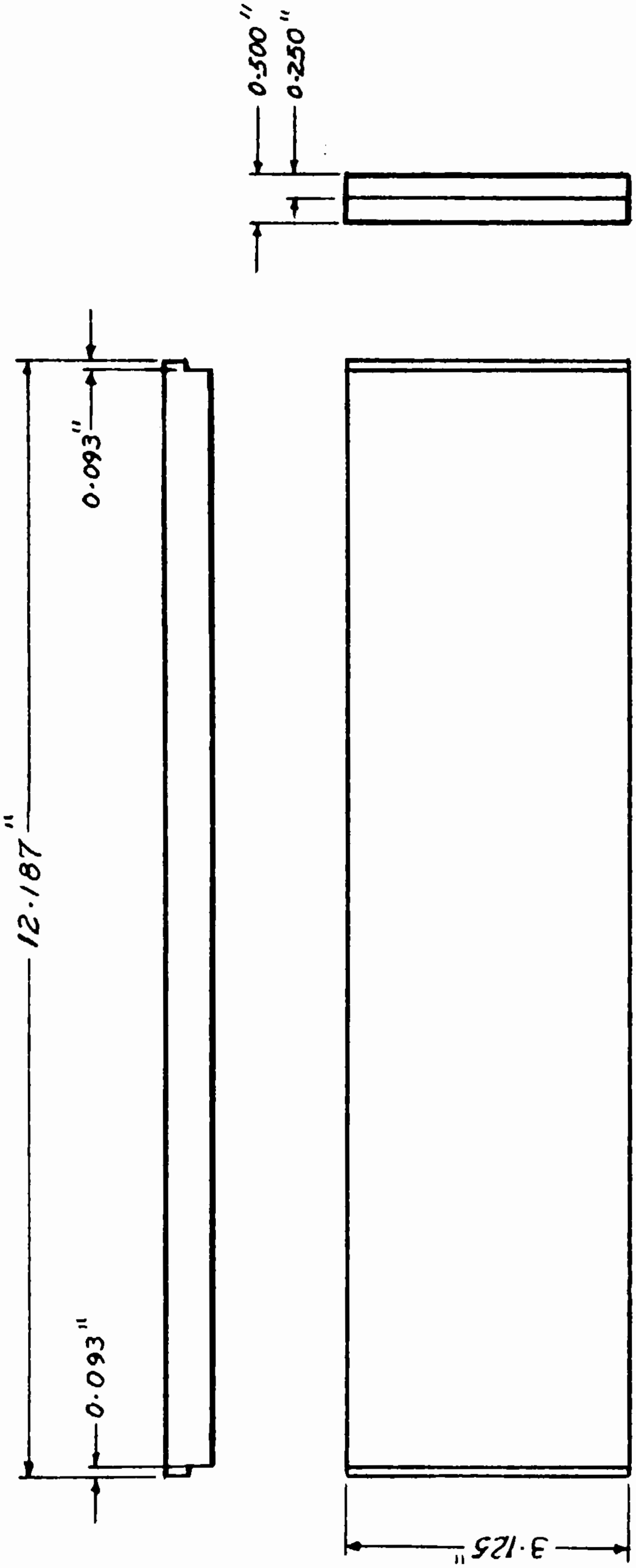

FIGURE 11. POROUS WALL

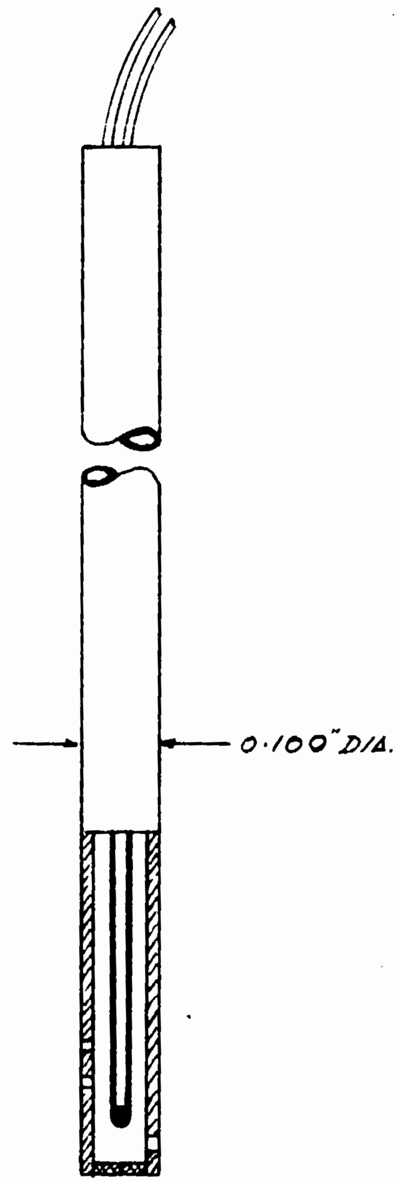

FIGURE 12. SHIELDED THERMOCOUPLE PROBE

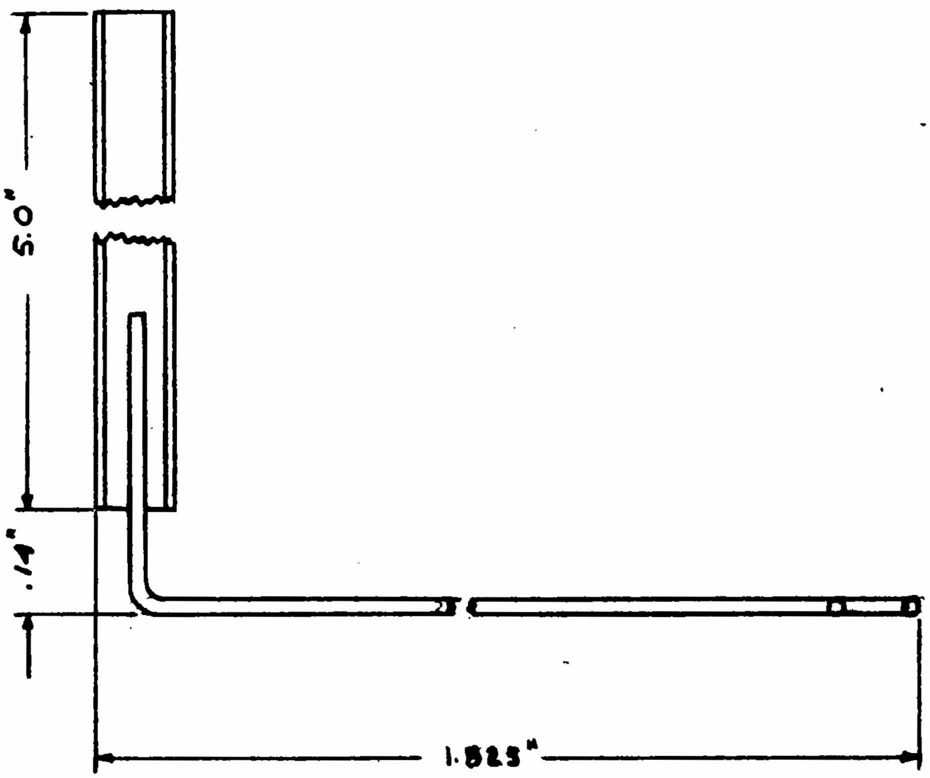

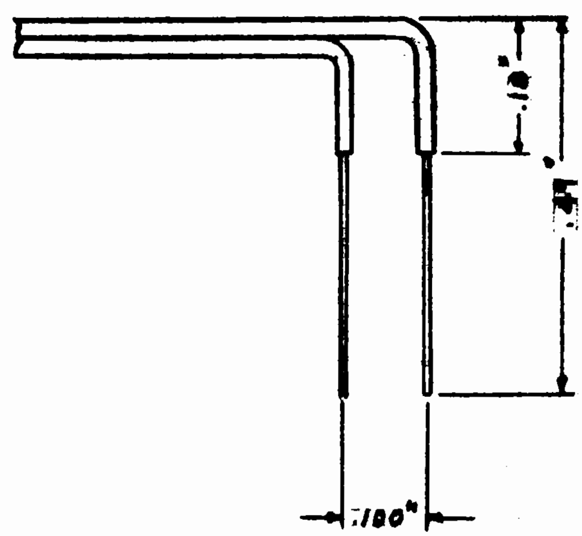

FIGURE 13. PITOT-THERMOCOUPLE PROBE

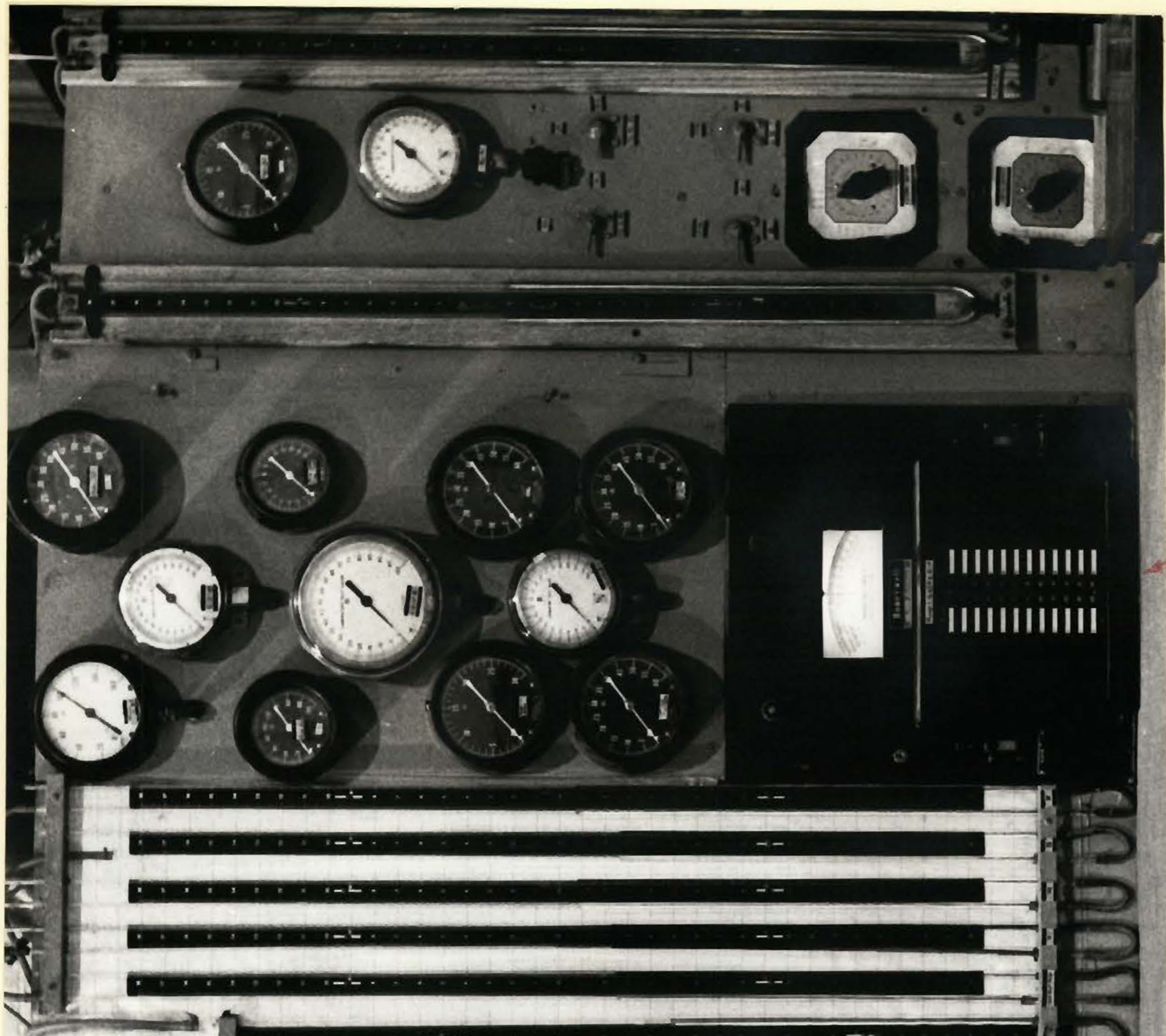

Potentiometer

Micromanometer

FIGURE 14. INSTRUMENT PANNEL

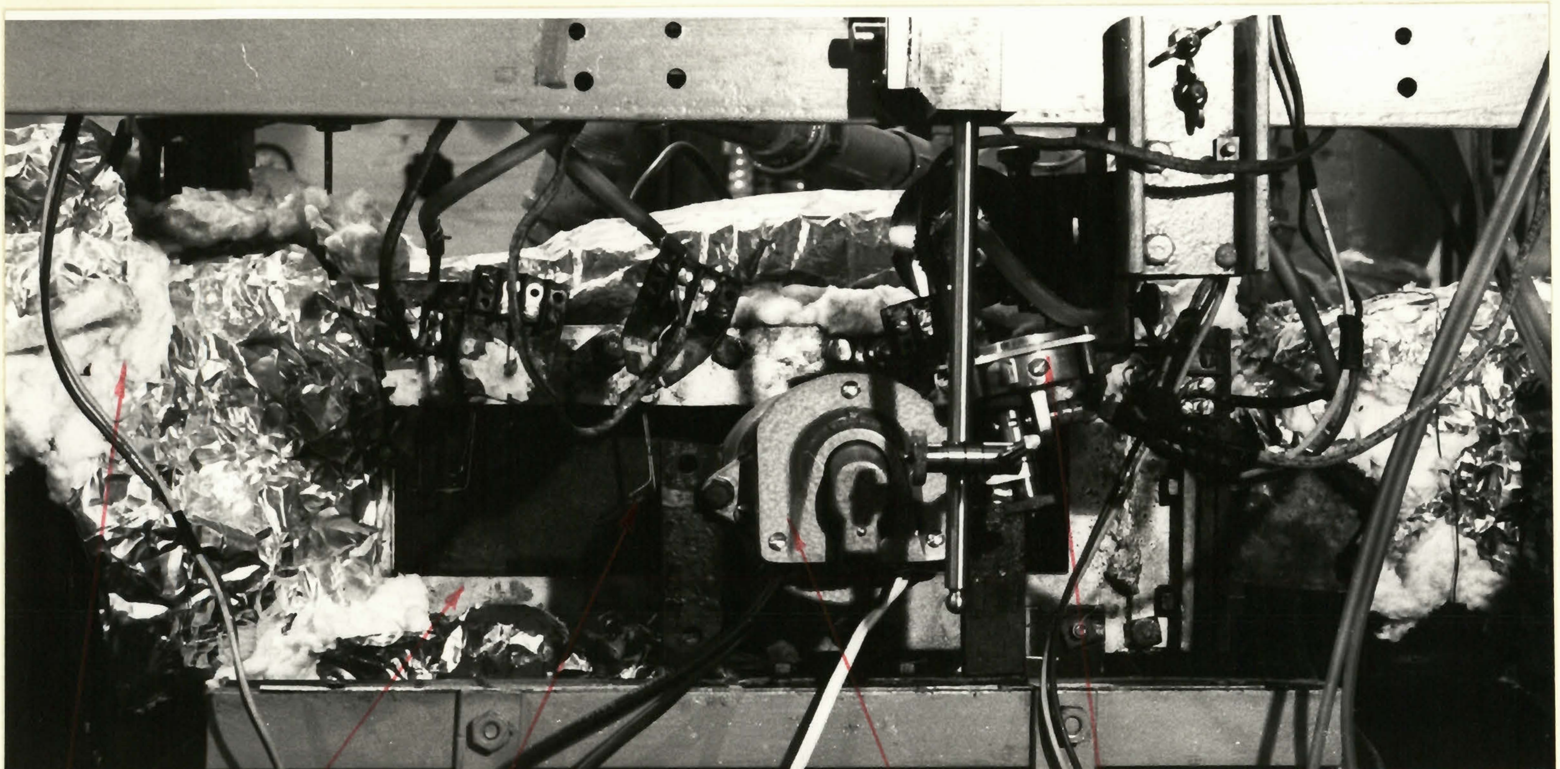

Insulation Test Duct Pitot-Thermocouple Probe Ardonox Ames Dial Gauge

FIGURE 15. SIDE VIEW OF TEST DUCT

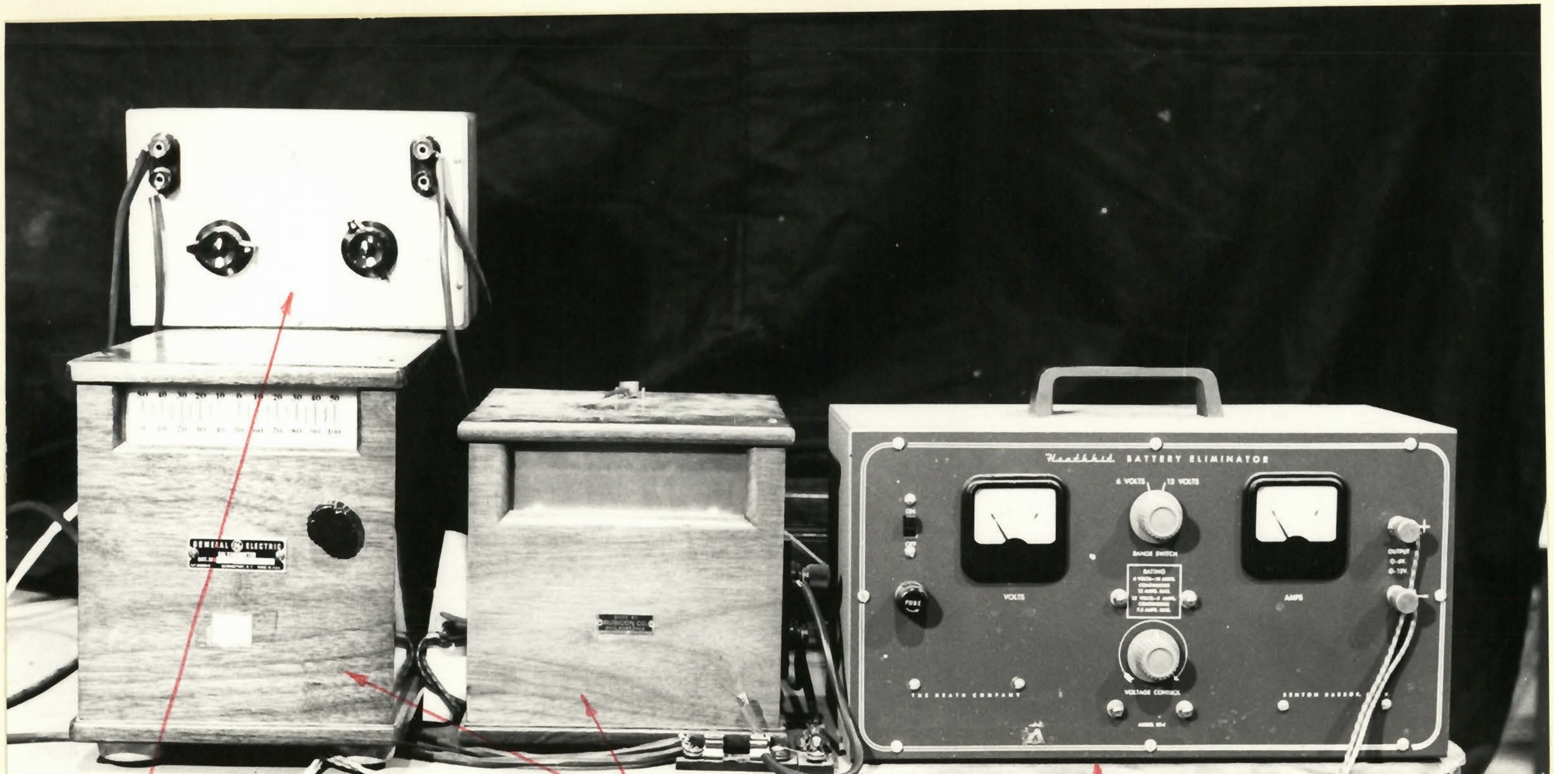

Voltage Attenuator Galvanometer Battery Eliminator

FIGURE 16. INSTRUMENTS USED WITH ARDONOX

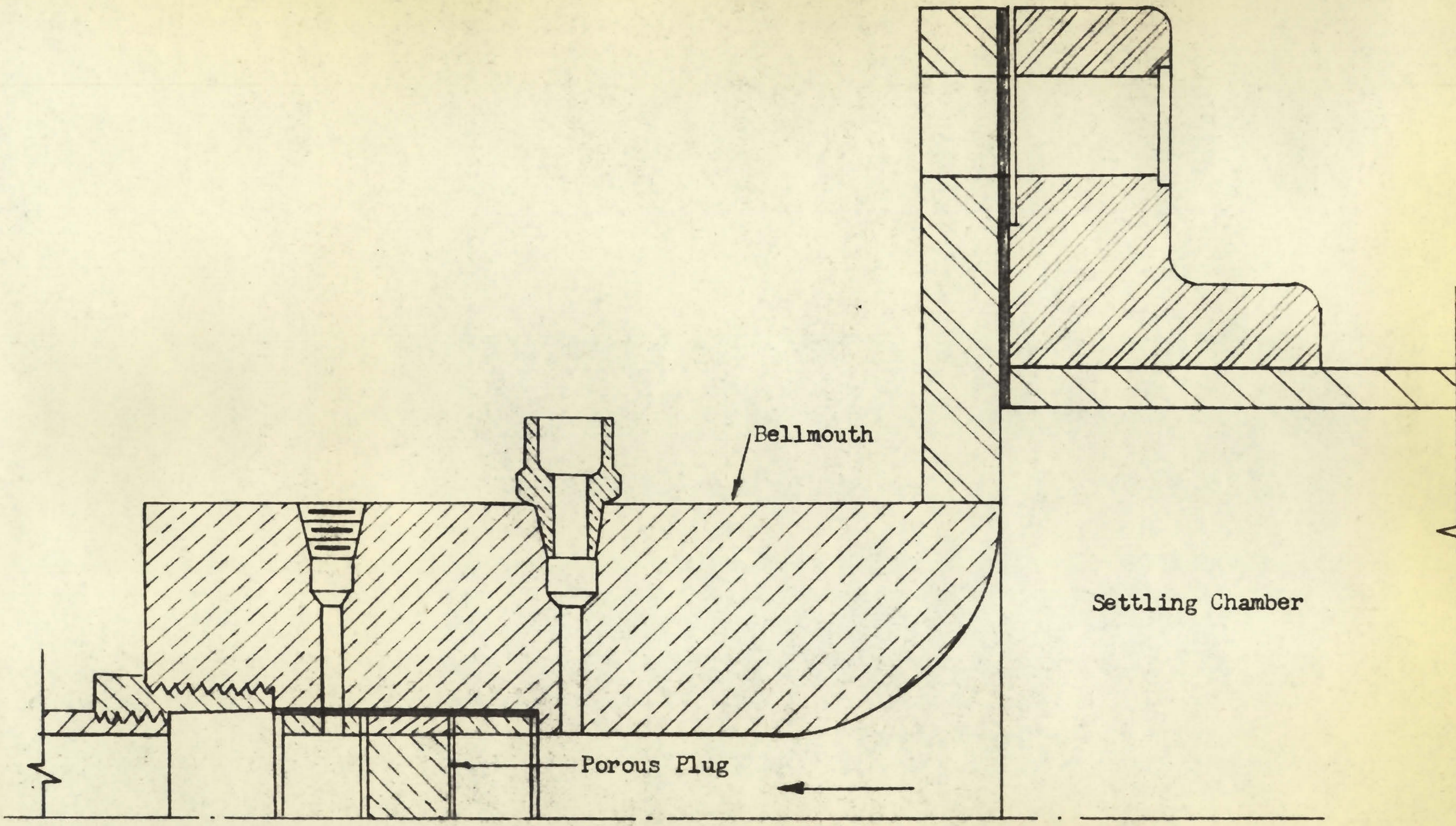

FIGURE 17. CROSS-SECTION OF BELLMOUTH AND SETTLING CHAMBER OF PRESSURE DROP RIG

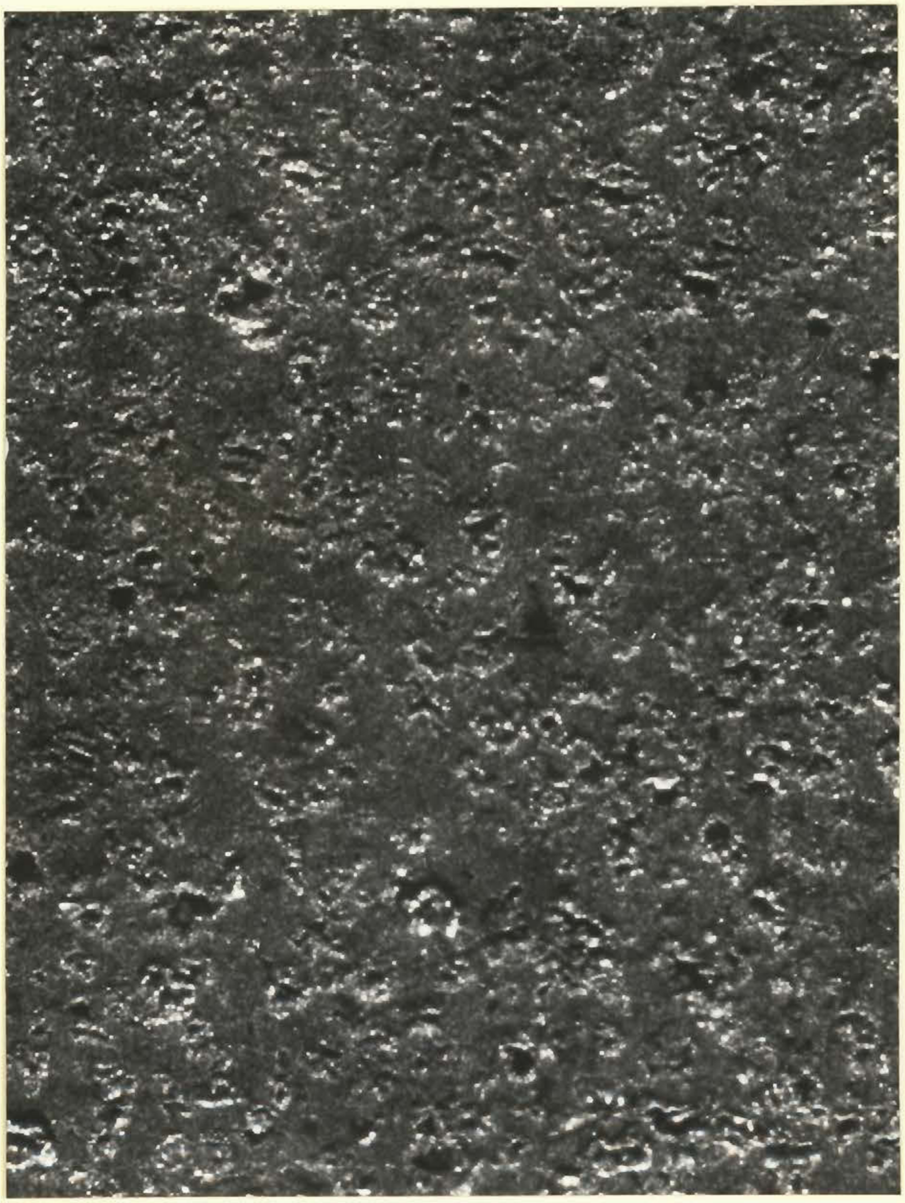

Porosity = 22.4%

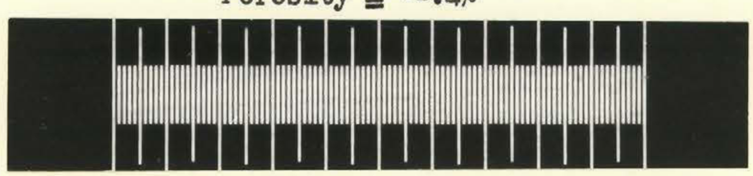

1 mm. with same magnification as the microphotographs

FIGURE 18. POROUS BRONZE PLUG SURFACE

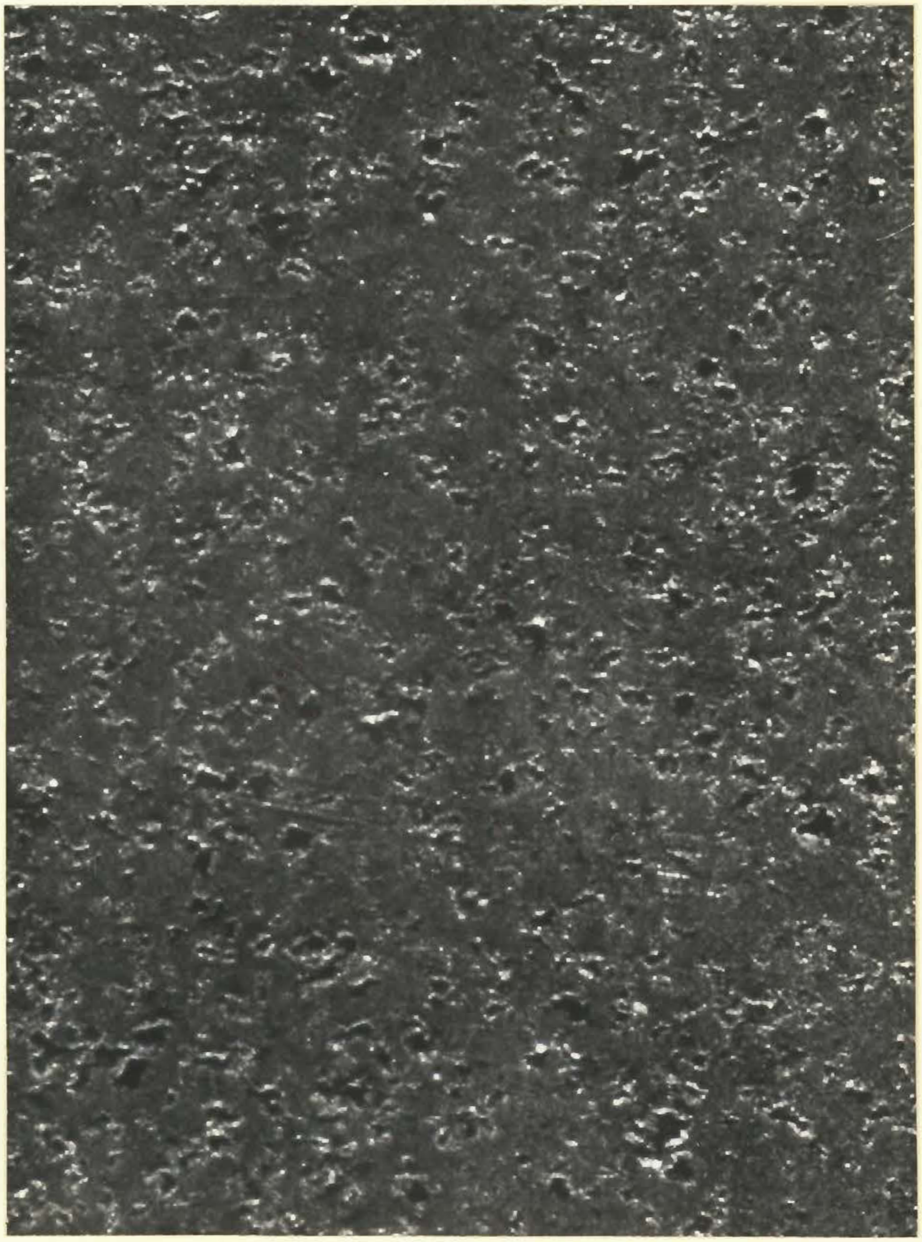

Porosity = 25.3%

FIGURE 19. POROUS BRONZE PLUG SURFACE

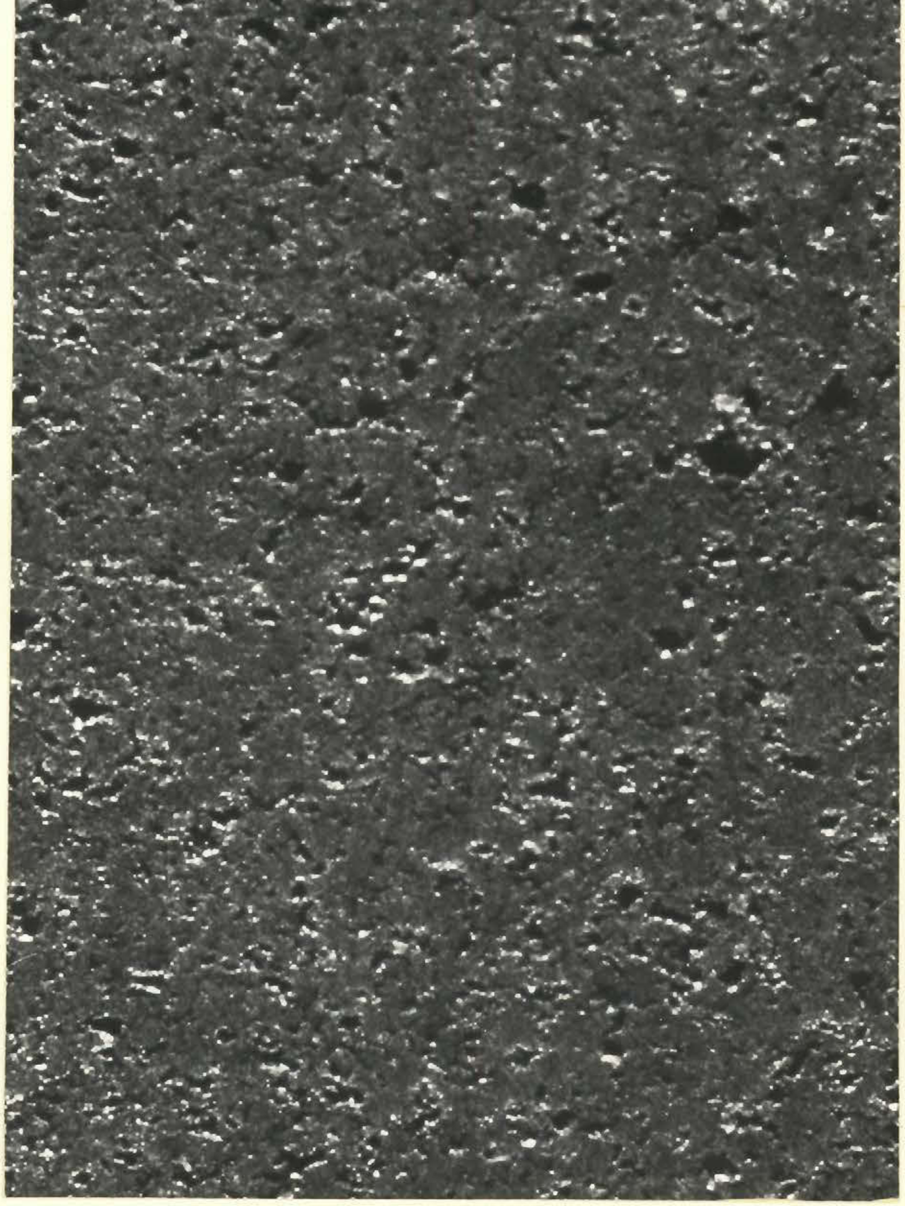

Porosity = 30.9%

FIGURE 20. POROUS BRONZE PLUG SURFACE

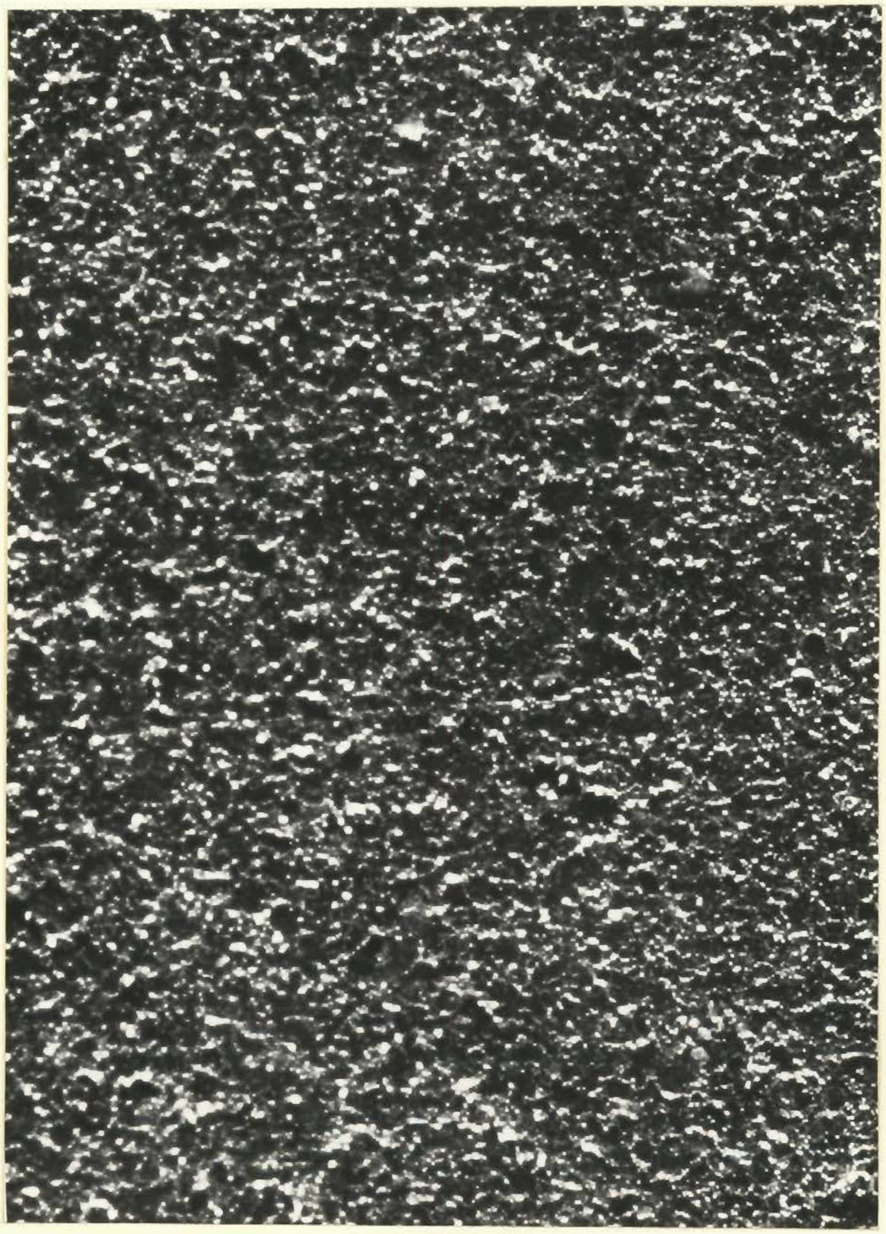

Porosity = 36.9%

FIGURE 21. POROUS BRONZE PLUG SURFACE

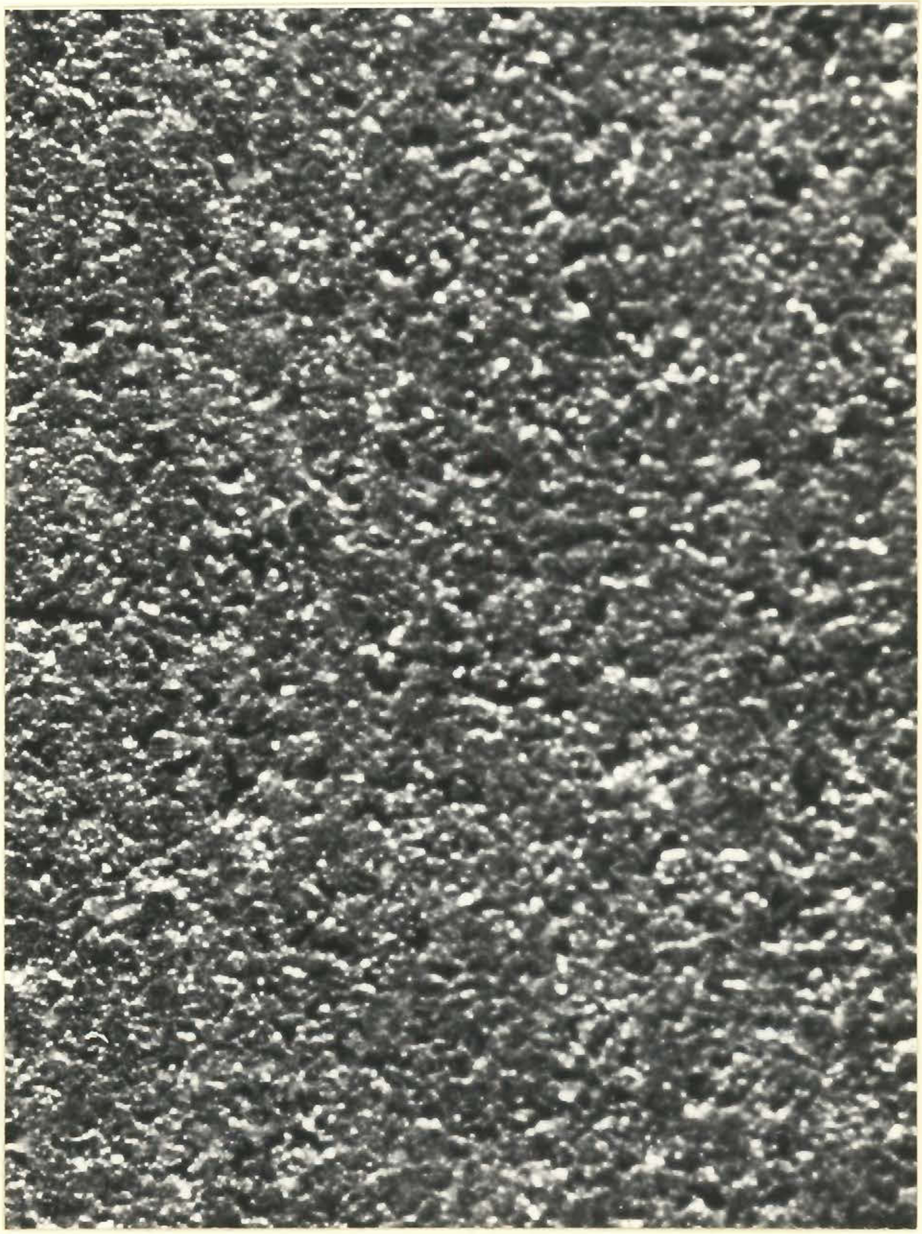

Porosity = 40.8%

FIGURE 22. POROUS BRONZE PLUG SURFACE

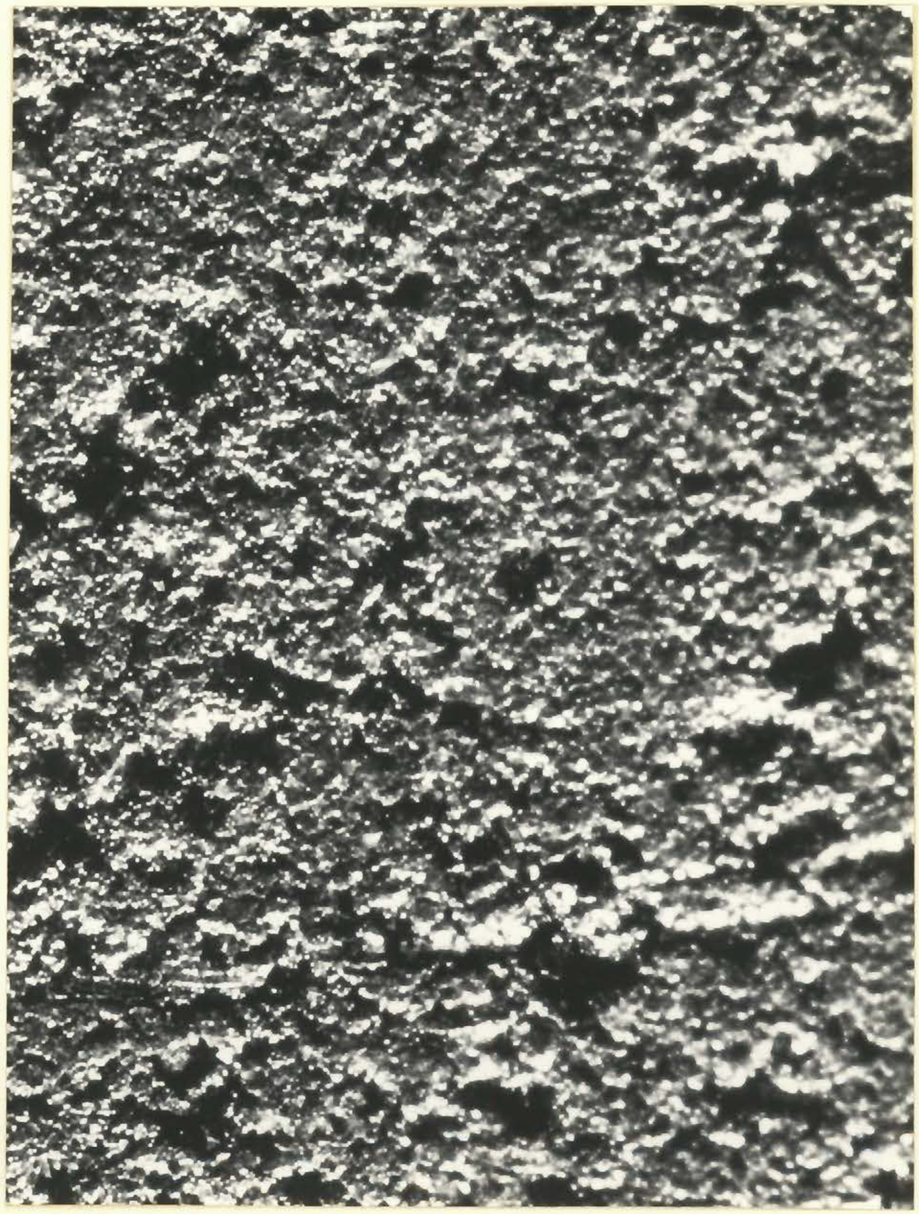

Porosity = 46.6%

FIGURE 23. POROUS BRONZE PLUG SURFACE

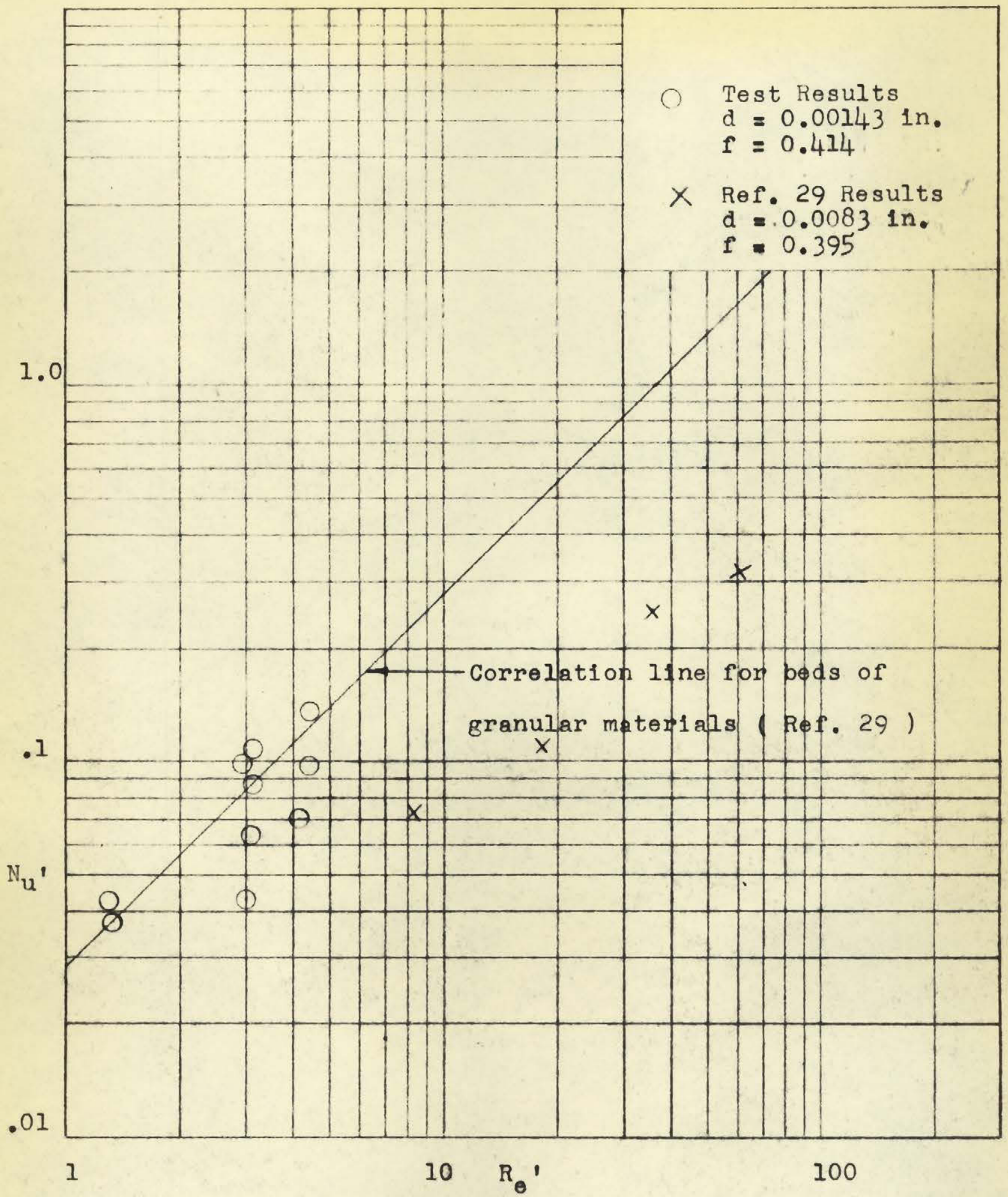

FIGURE 24. INTERNAL HEAT TRANSFER CORRELATION FOR POROUS BRONZE

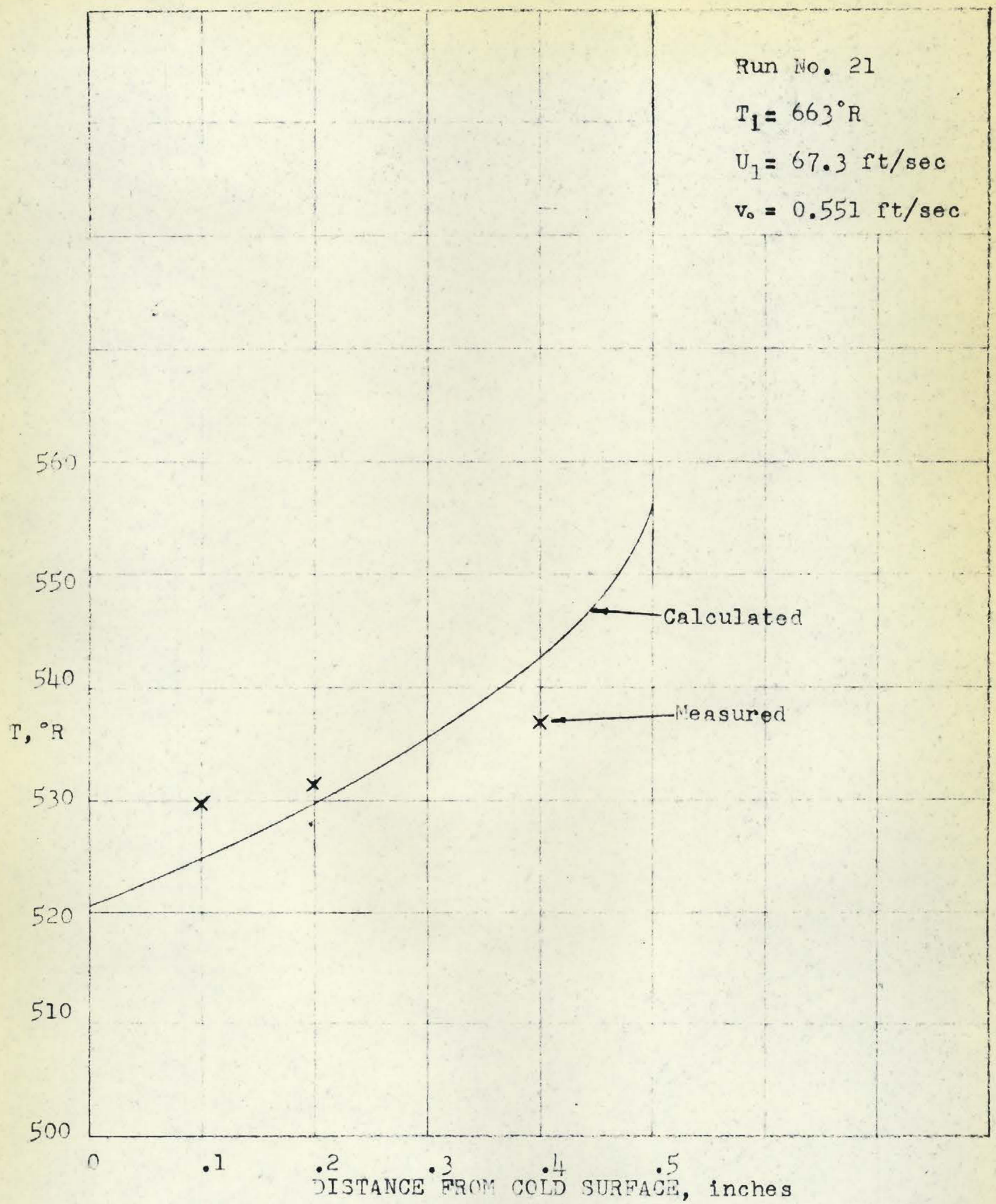

FIGURE 25. TEMPERATURE DISTRIBUTION IN POROUS WALL

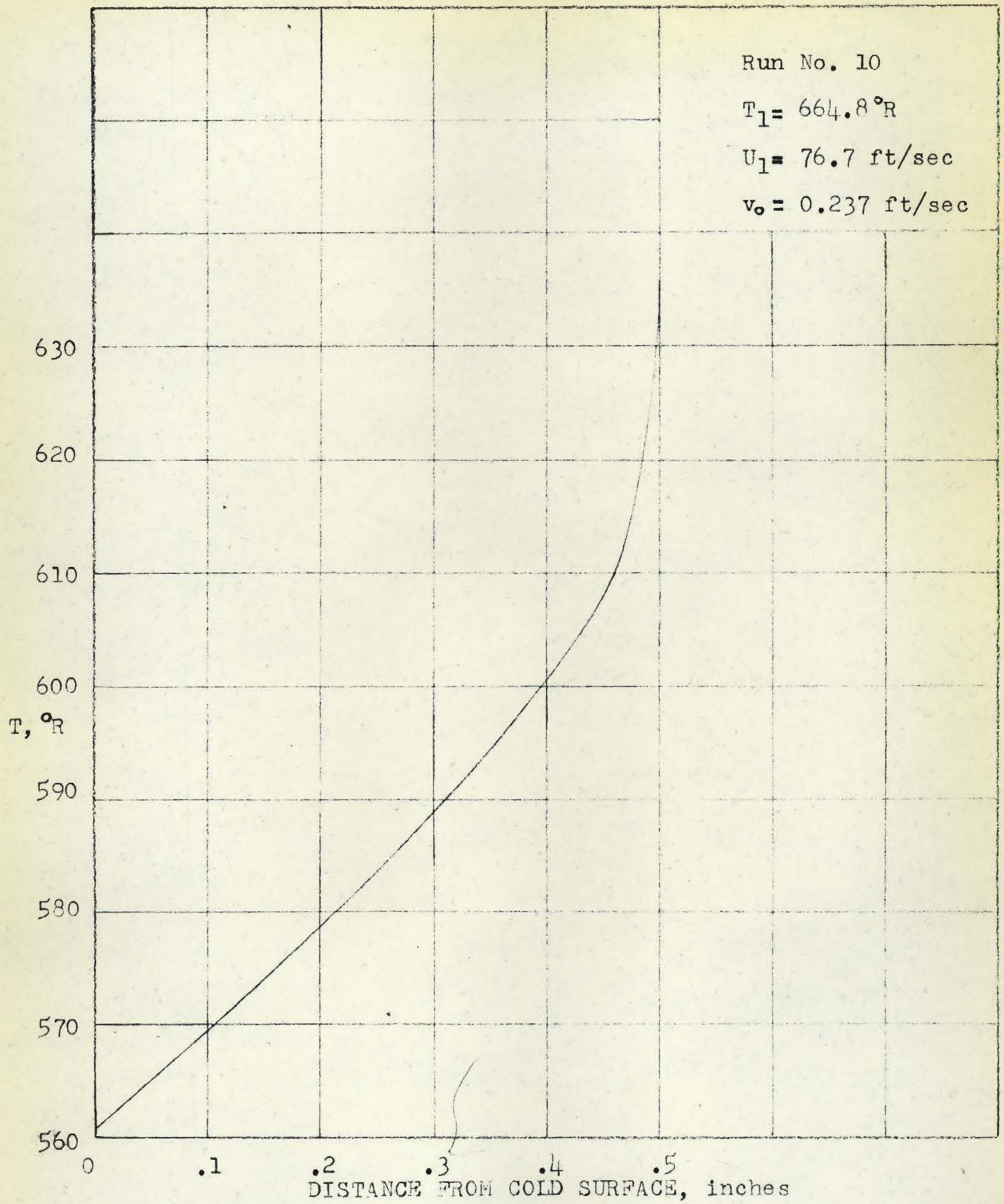

FIGURE 26. CALCULATED TEMPERATURE DISTRIBUTION IN POROUS WALL

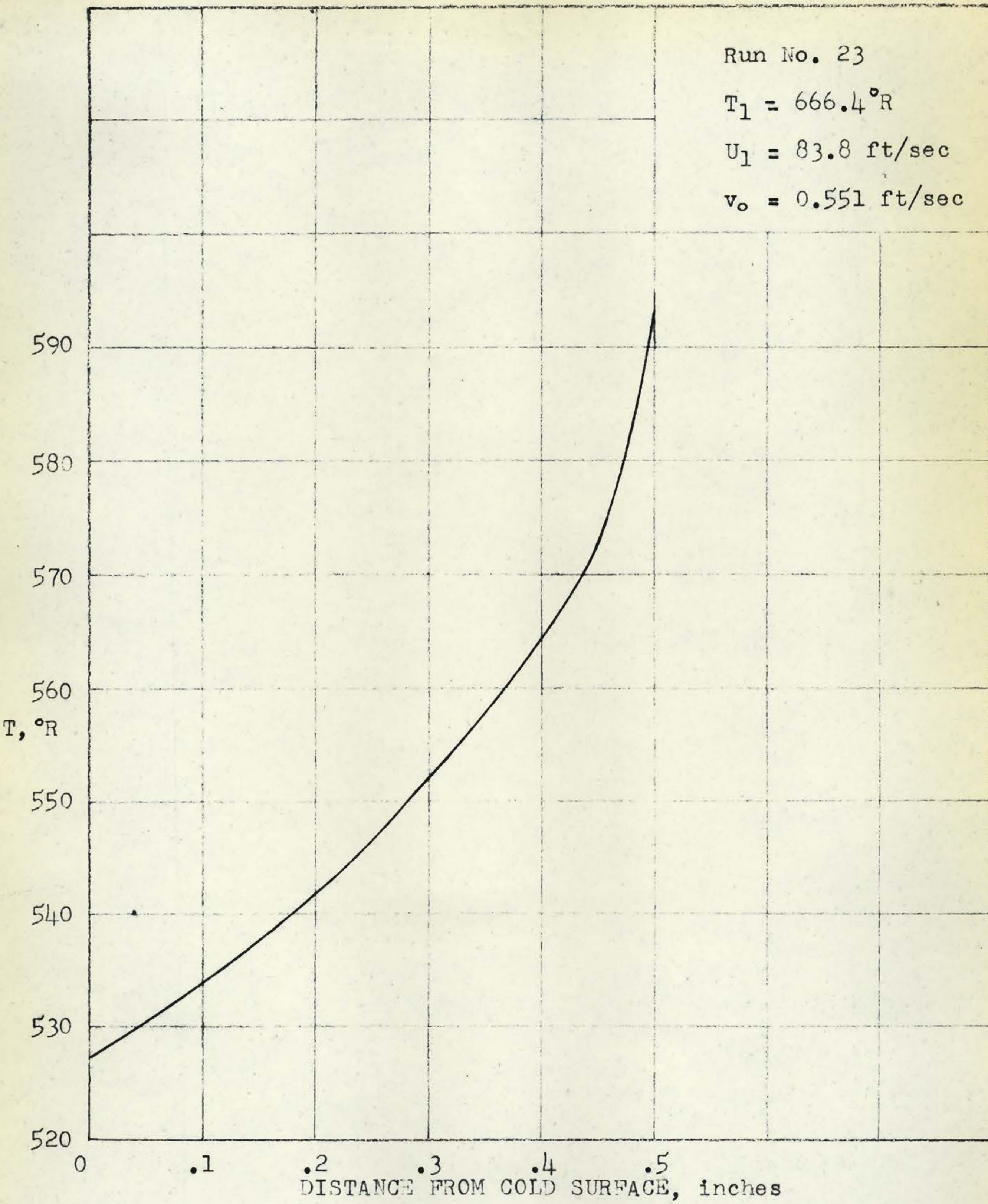

FIGURE 27. CALCULATED TEMPERATURE DISTRIBUTION IN POROUS WALL

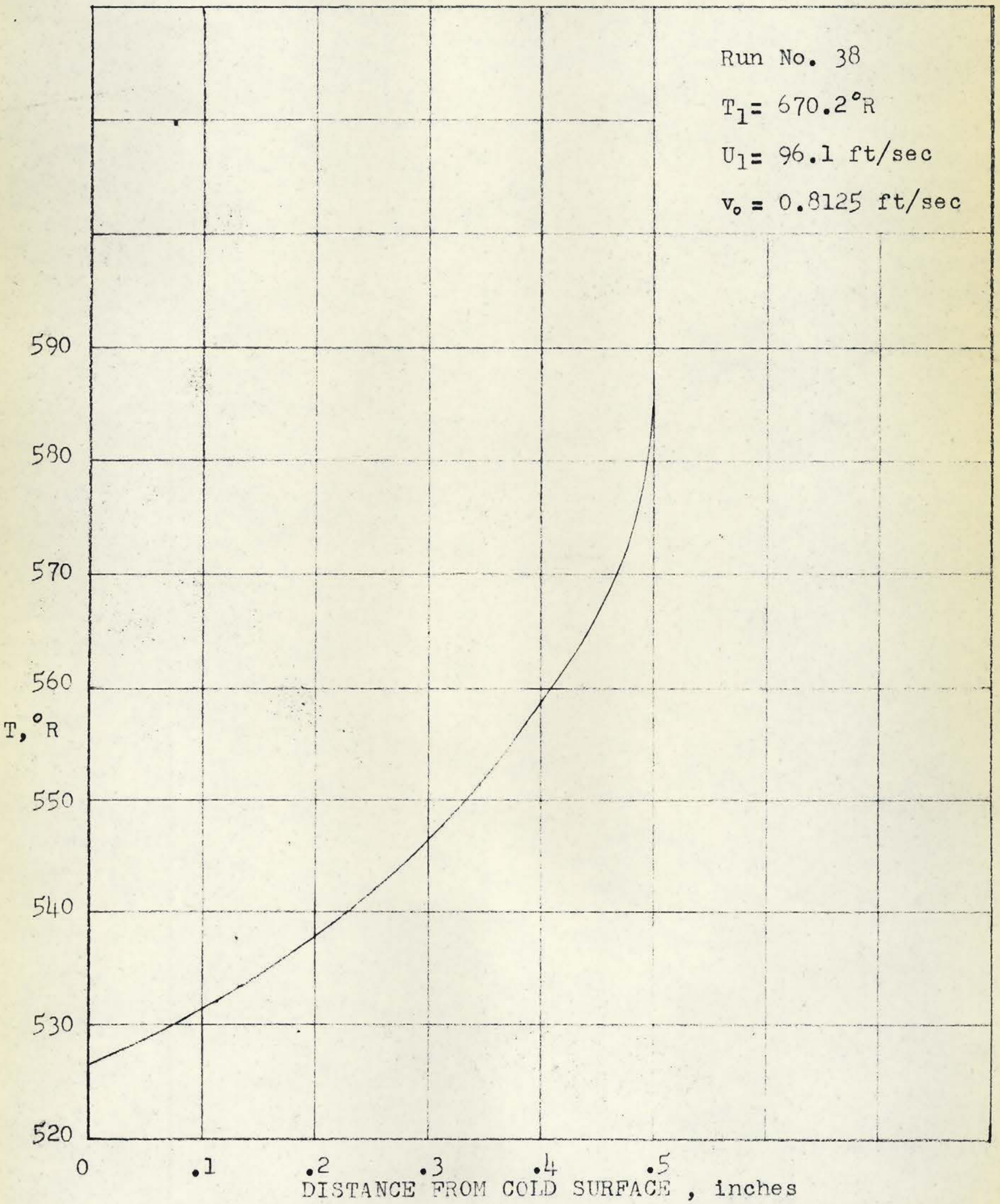

FIGURE 28. CALCULATED TEMPERATURE DISTRIBUTION IN POROUS WALL

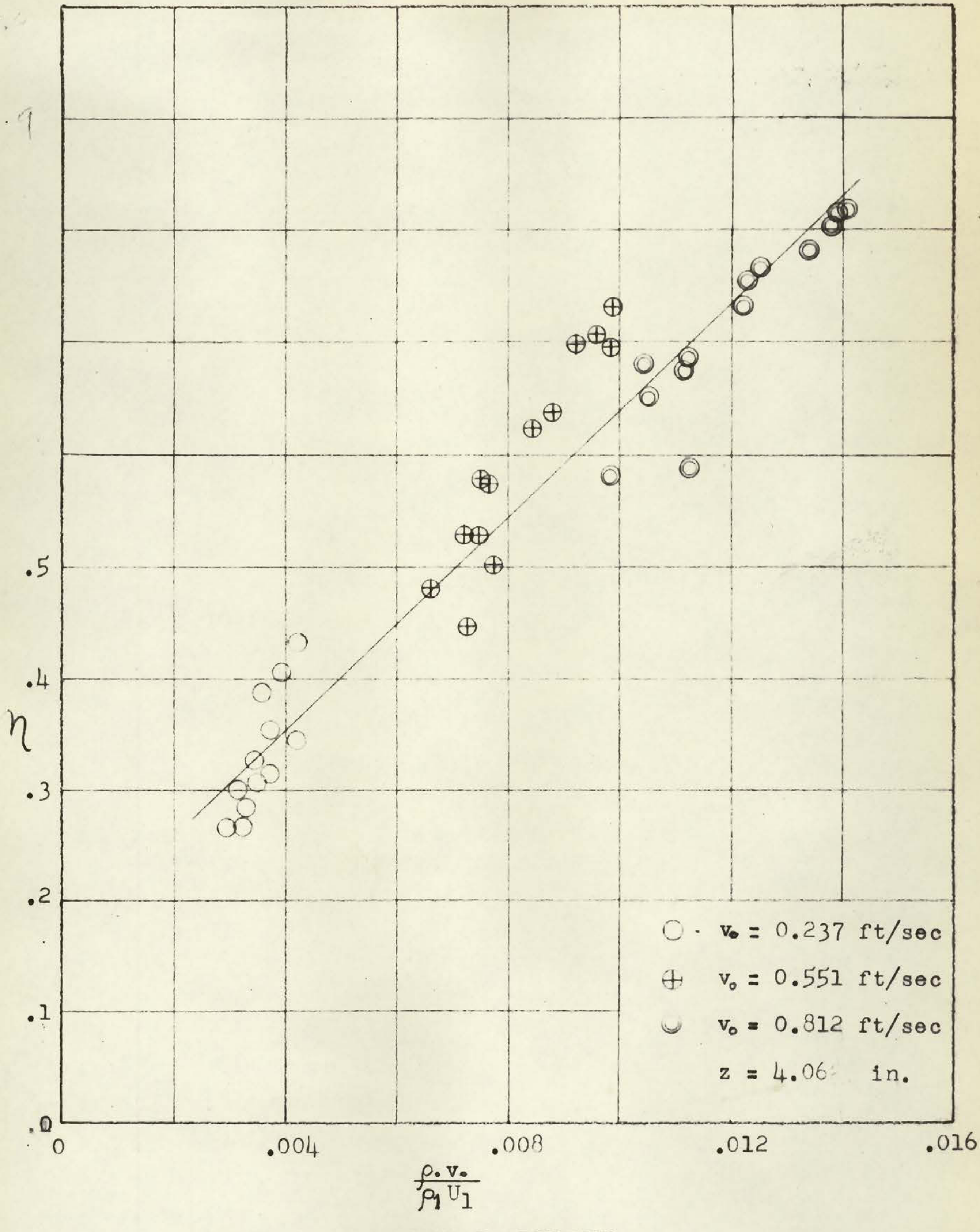

FIGURE 29. COOLING EFFICIENCY

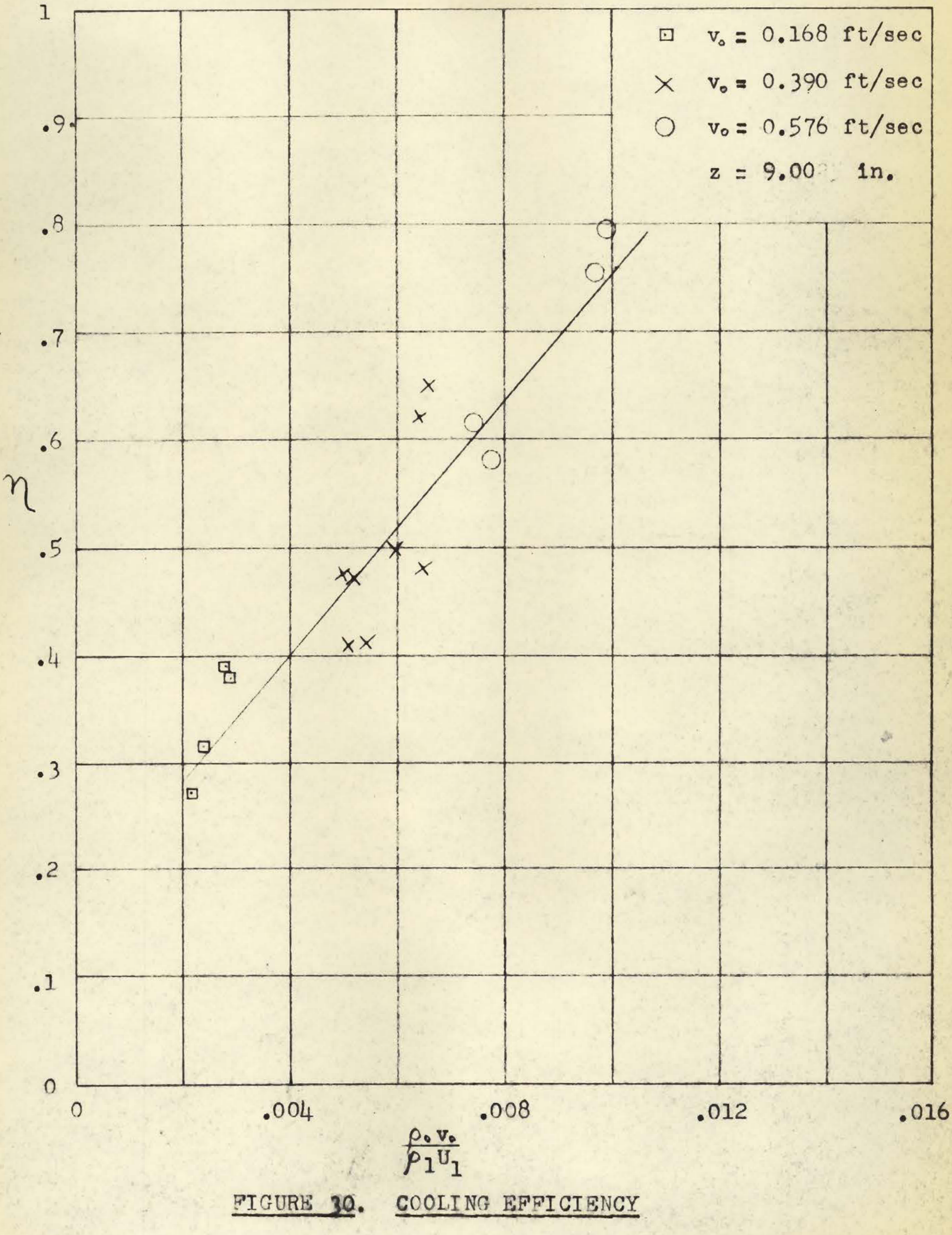

FIGURE 30. COOLING EFFICIENCY

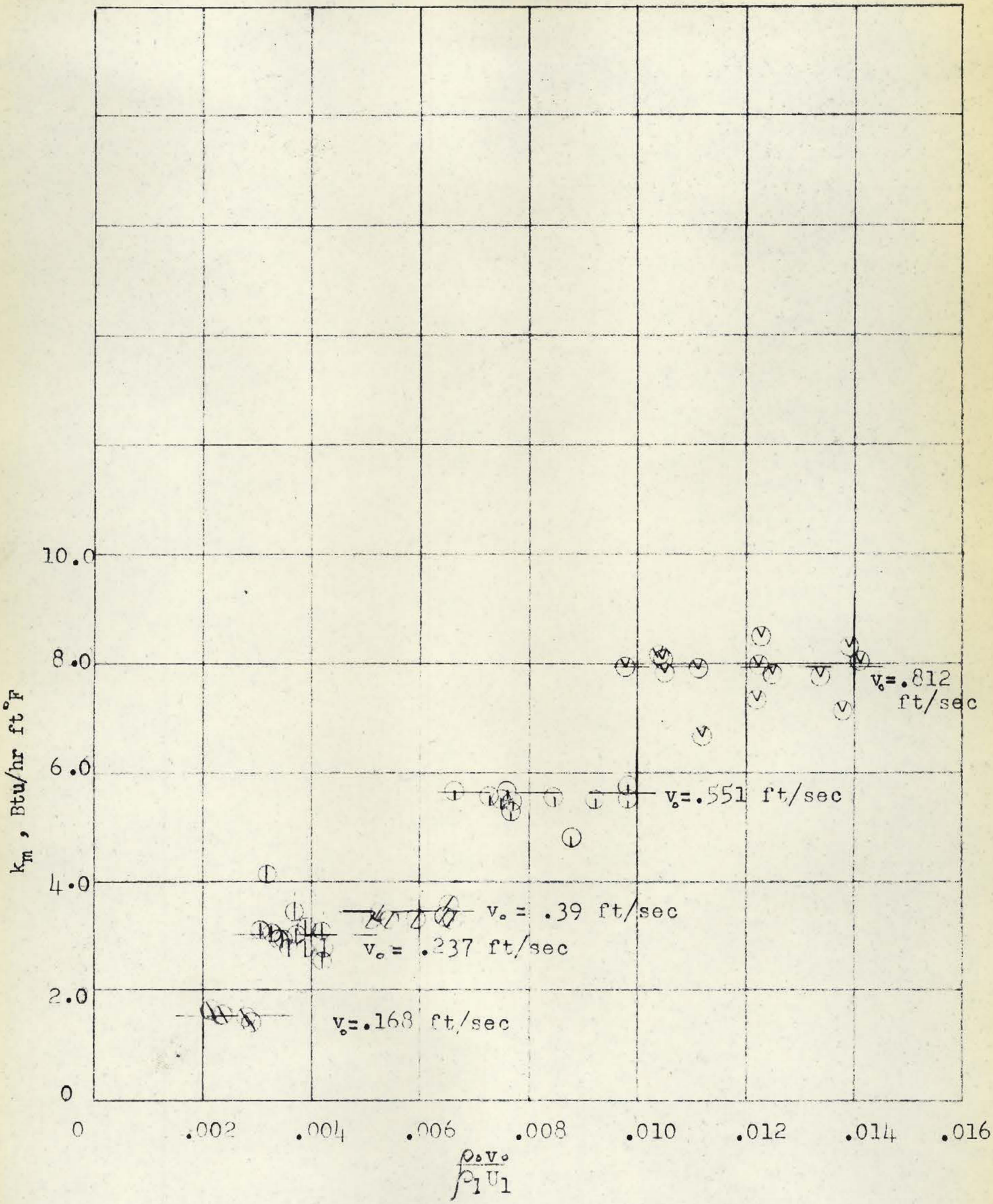

FIGURE 31. COMBINED THERMAL CONDUCTIVITY

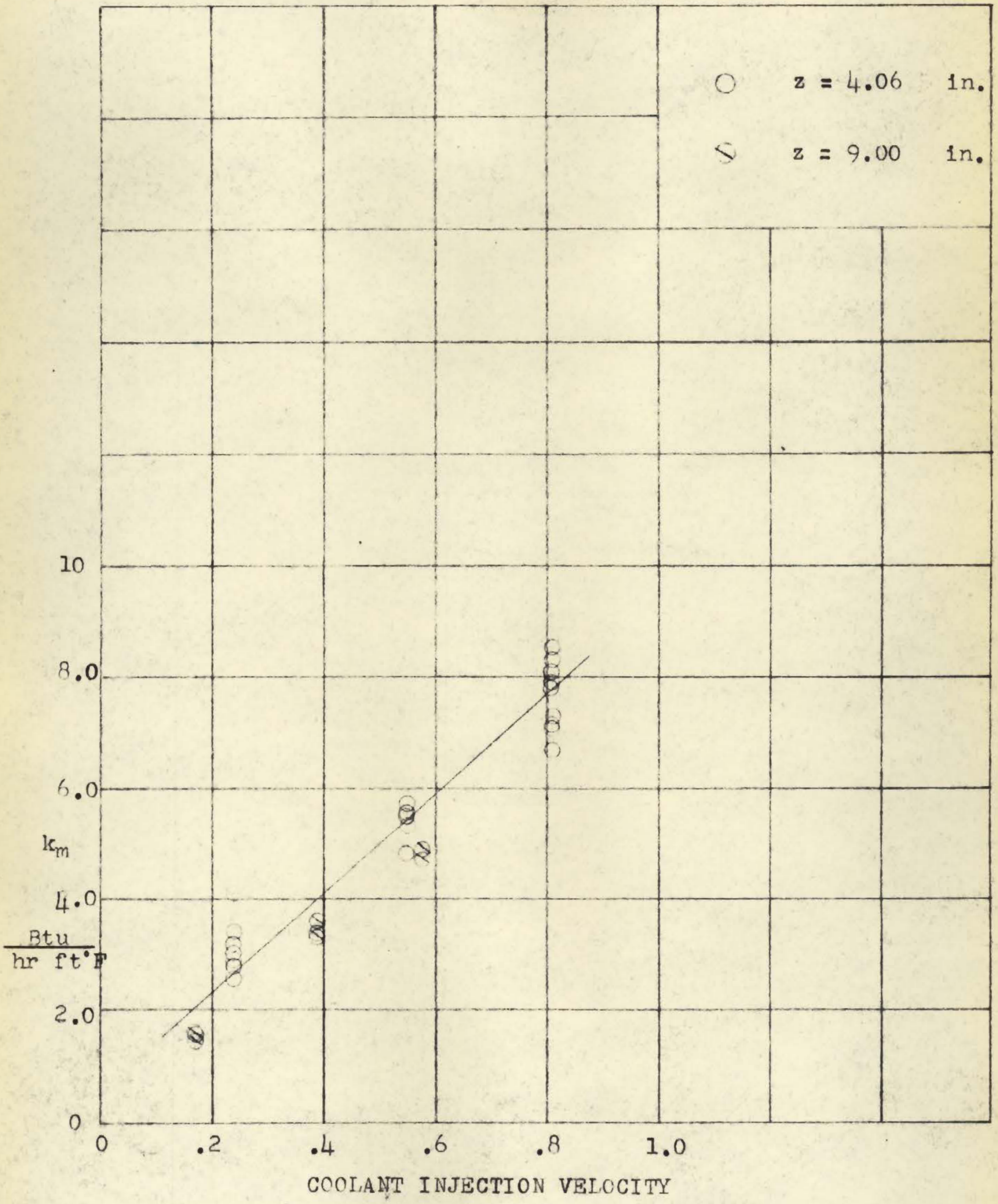

FIGURE 32. COMBINED THERMAL CONDUCTIVITY

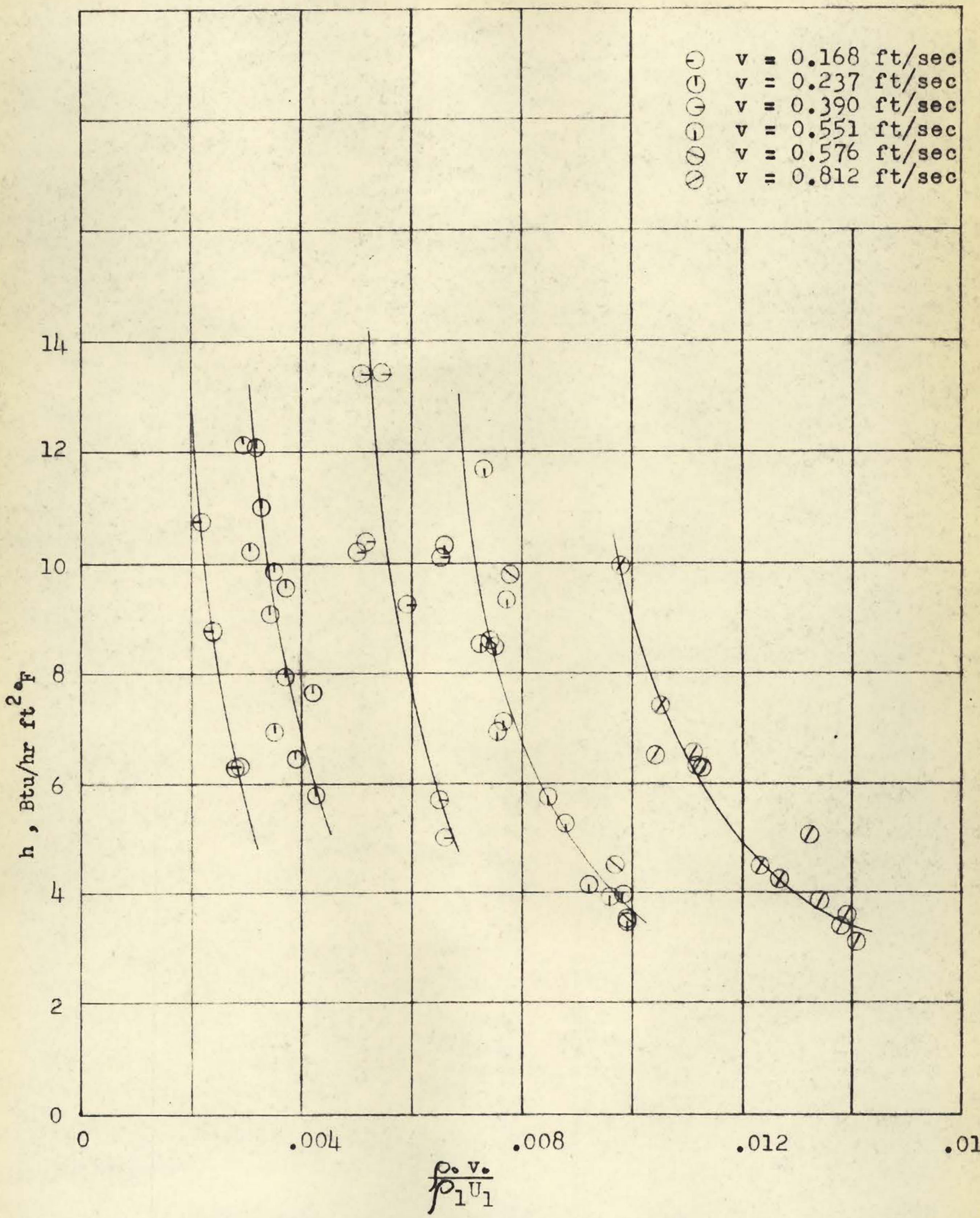

FIGURE 33. HEAT TRANSFER COEFFICIENT

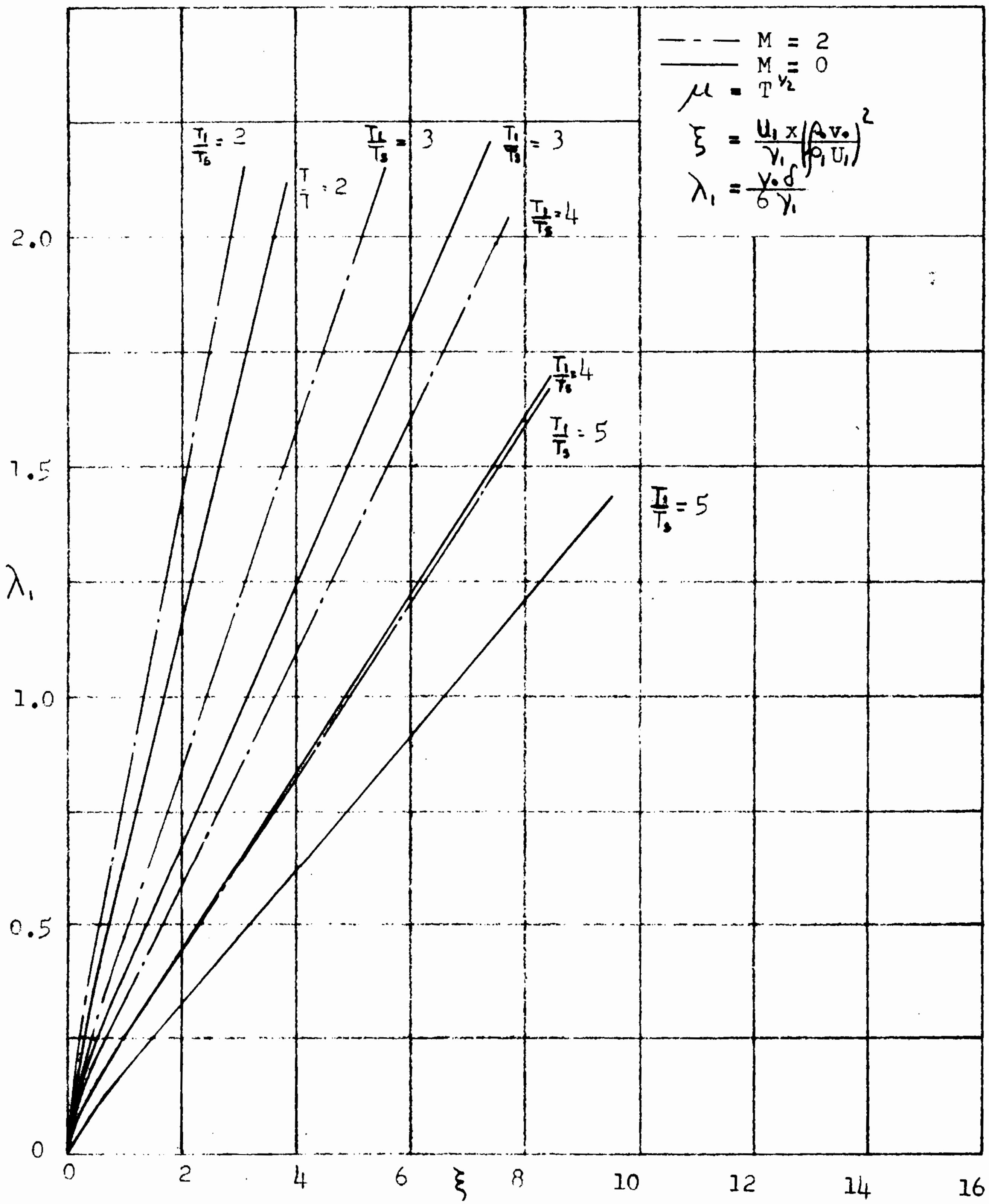

FIGURE 34. NON-DIMENSIONAL BOUNDARY LAYER THICKNESS VS. NON-DIMENSIONAL LENGTH IN DIRECTION OF FLOW (from ref.69)

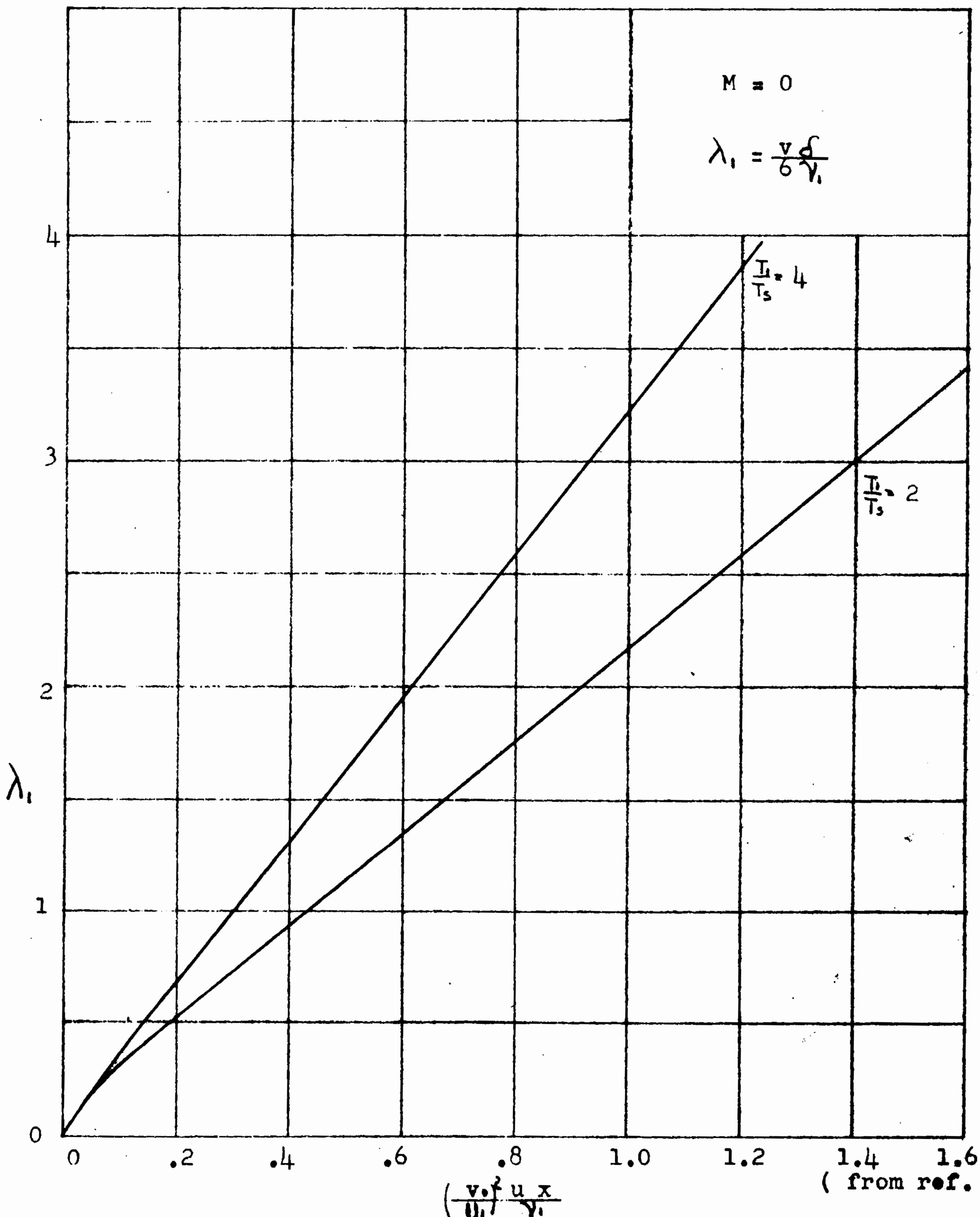

(from ref. 69)

FIGURE 35. NON-DIMENSIONAL BOUNDARY LAYER THICKNESS VS. NON-DIMENSIONAL LENGTH IN DIRECTION OF FLOW

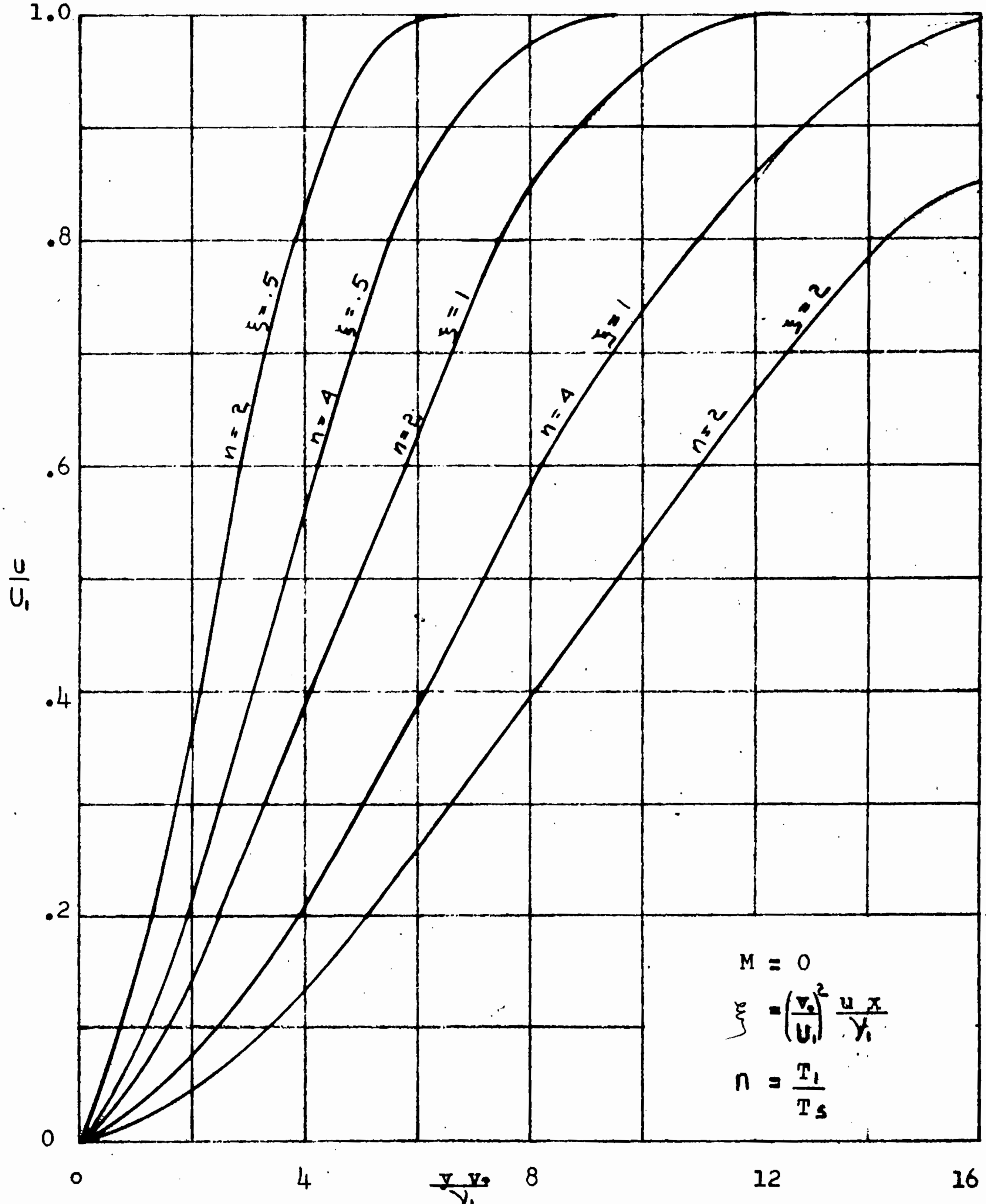

(from ref.69)

FIGURE 36. VELOCITY PROFILES AGAINST $\frac{v_0 y}{\gamma_1}$ AT DIFFERENT LOCATION ALONG THE PLATE

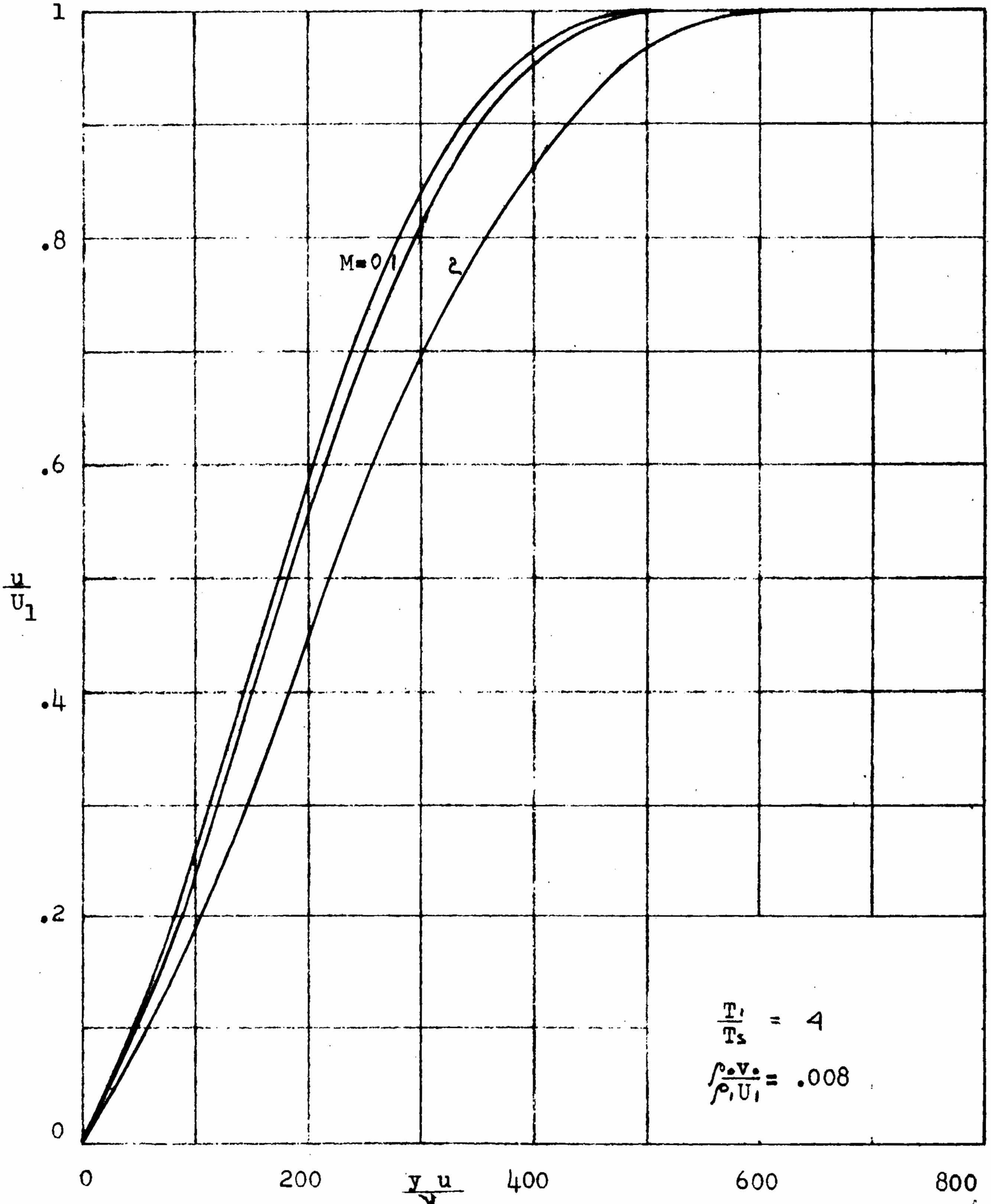

(from ref. 69)

FIGURE 37. VELOCITY PROFILES VS. $\left(\frac{y\,u}{\nu_1}\right)$ FOR DIFFERENT MACH NUMBERS

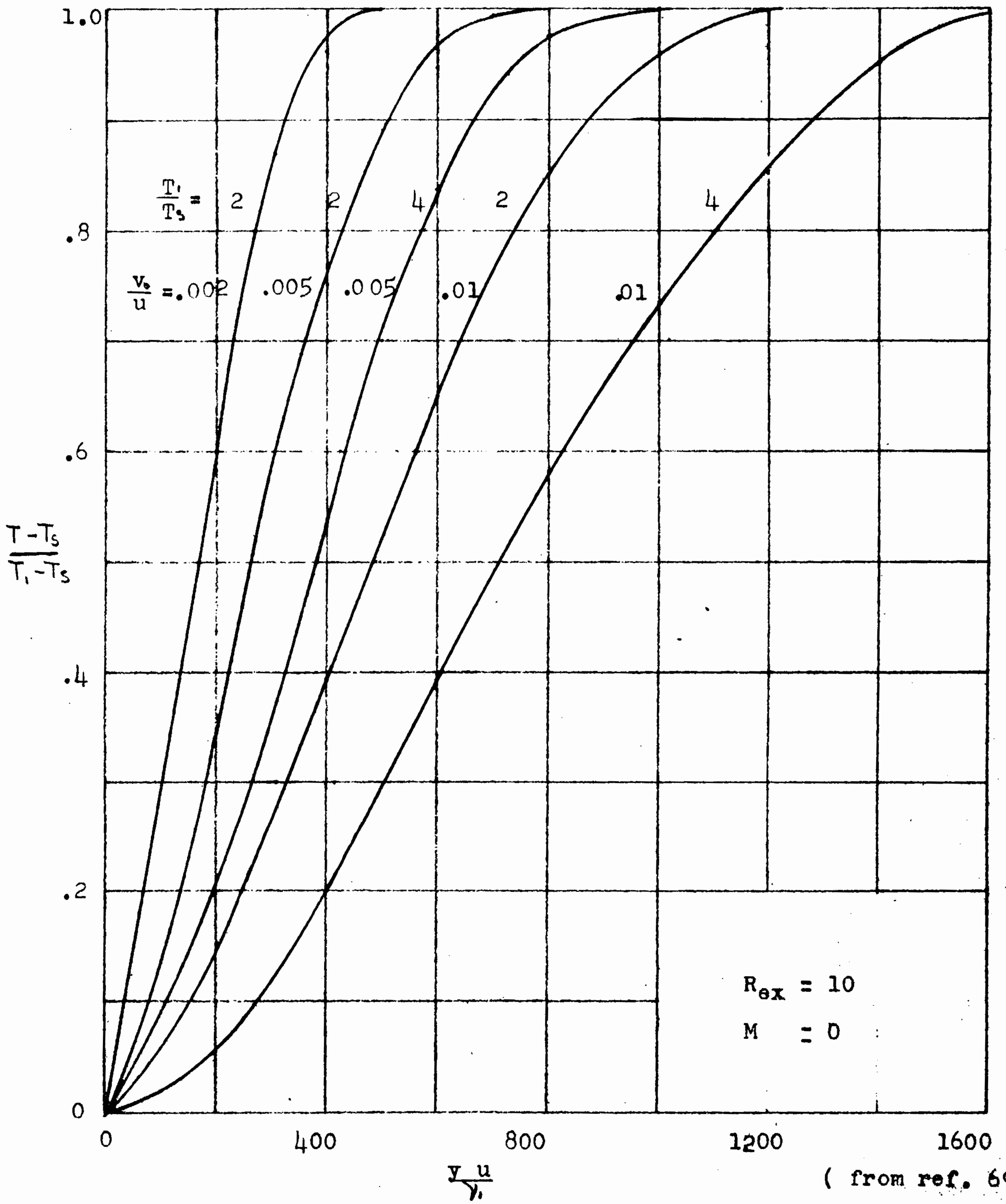

(from ref. 69)

FIGURE 38. TEMPERATURE PROFILES AGAINST $\frac{yu}{\nu_1}$ FOR VARIOUS INJECTION VELOCITIES

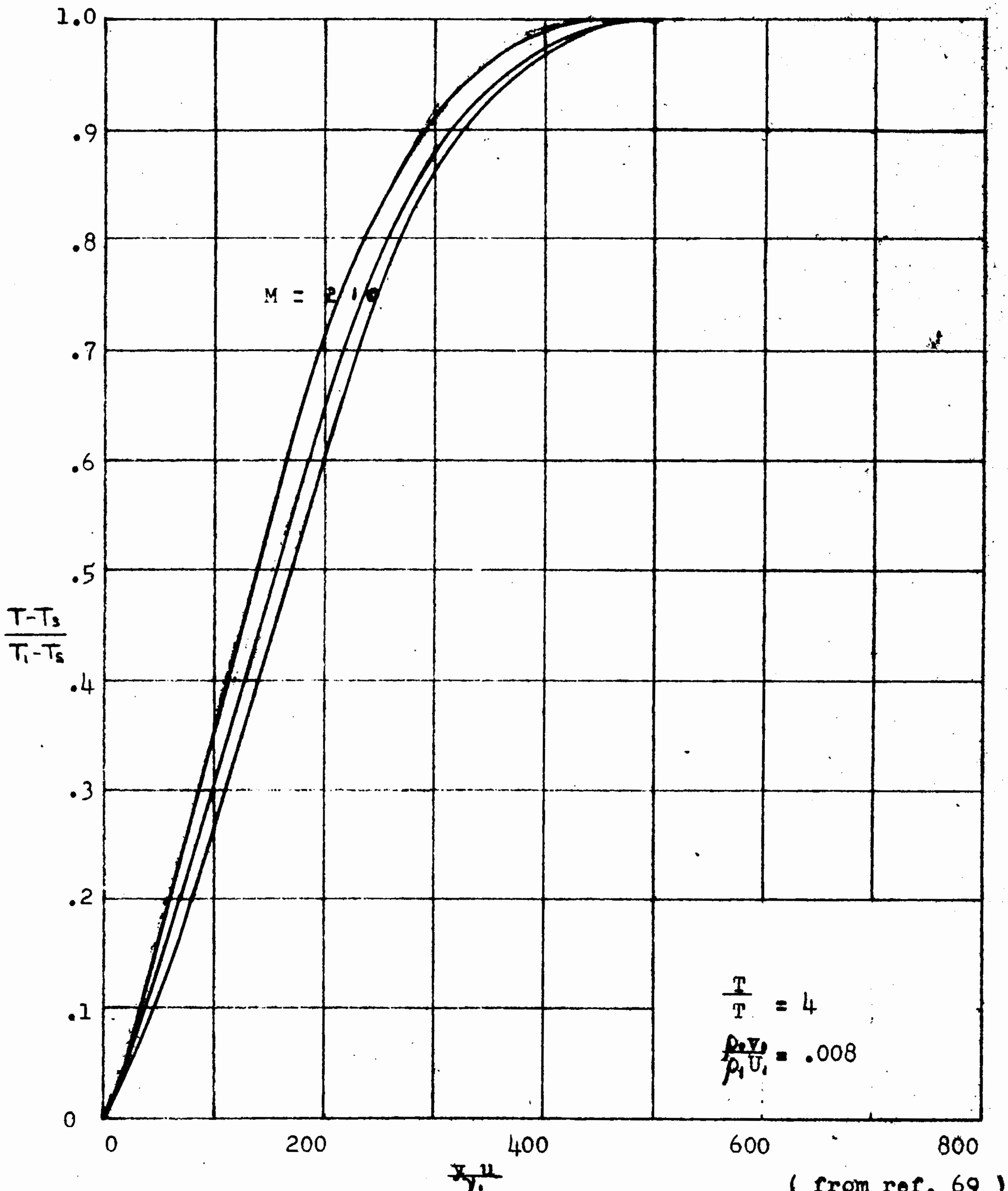

(from ref. 69)

FIGURE 39. VELOCITY PROFILES VS. $\frac{y\,u}{\gamma_1}$ FOR DIFFERENT MACH NUMBERS

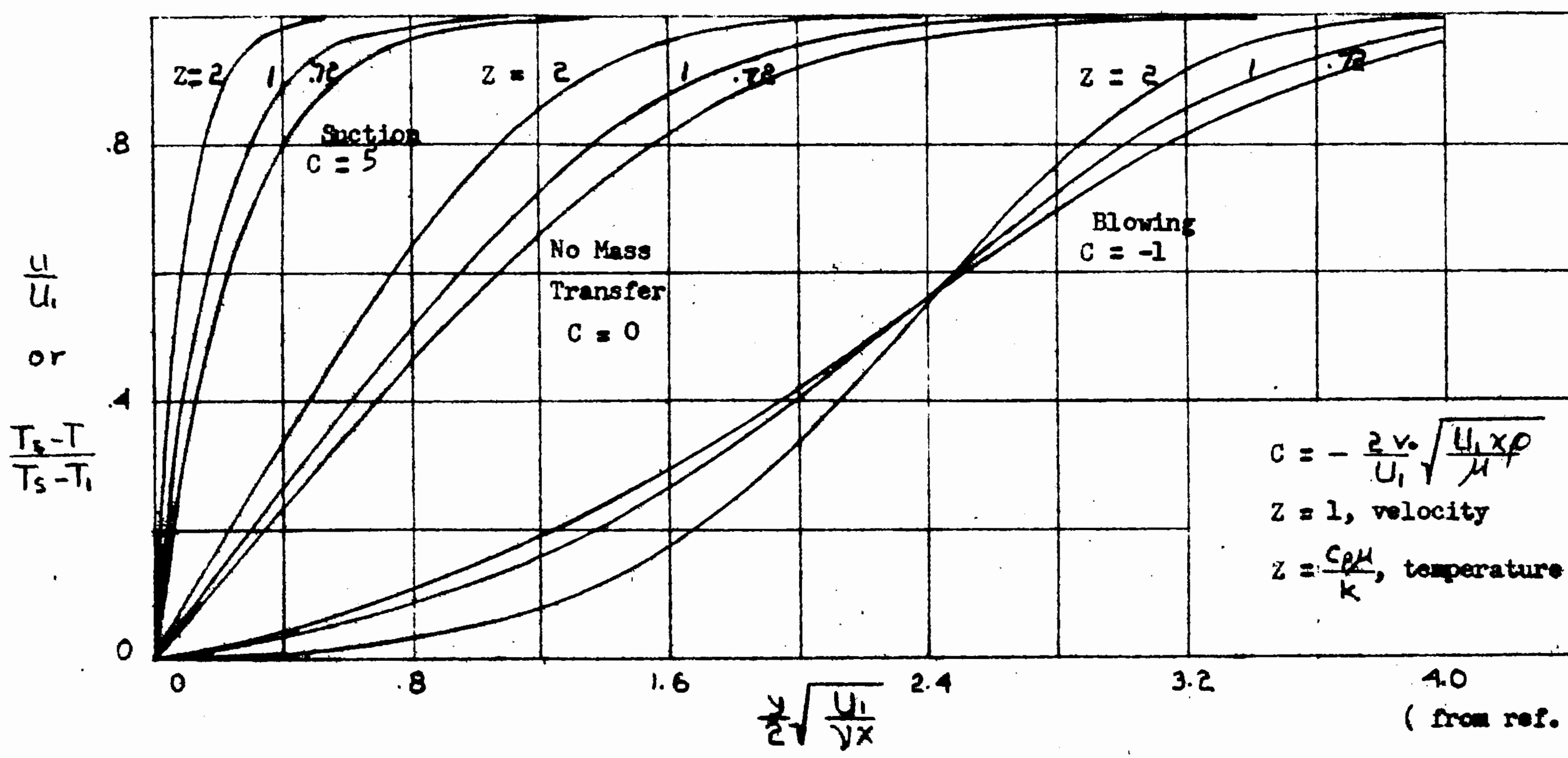

(from ref. 46)

FIGURE 40. THEORETICAL LAMINAR-BOUNDARY-LAYER PROFILES WITH SUCTION AND BLOWING

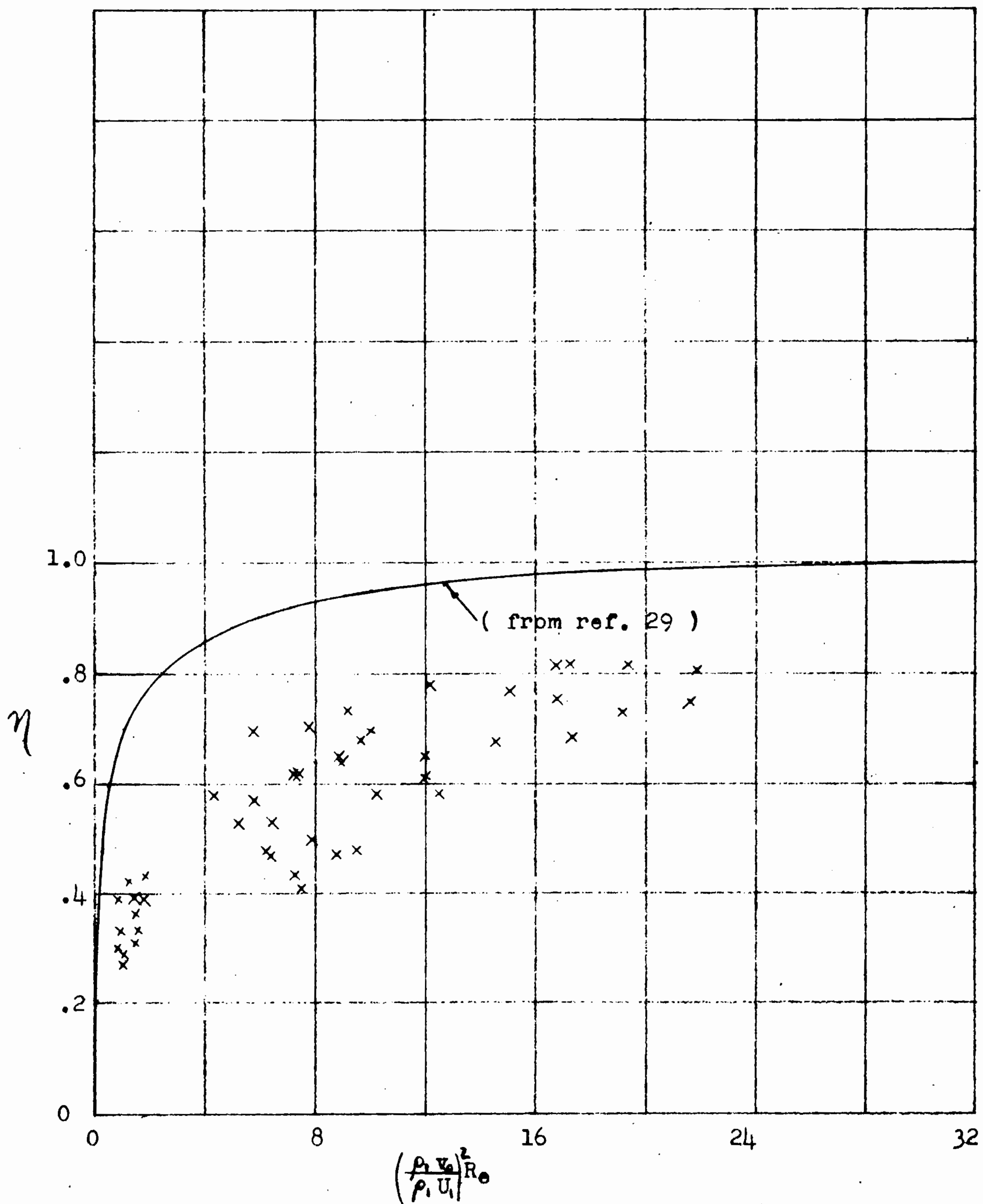

FIGURE 41. COOLING EFFICIENCY AGAINST $\left(\frac{\rho_1 v_o}{\rho_1 U_1}\right)^2 R_e$

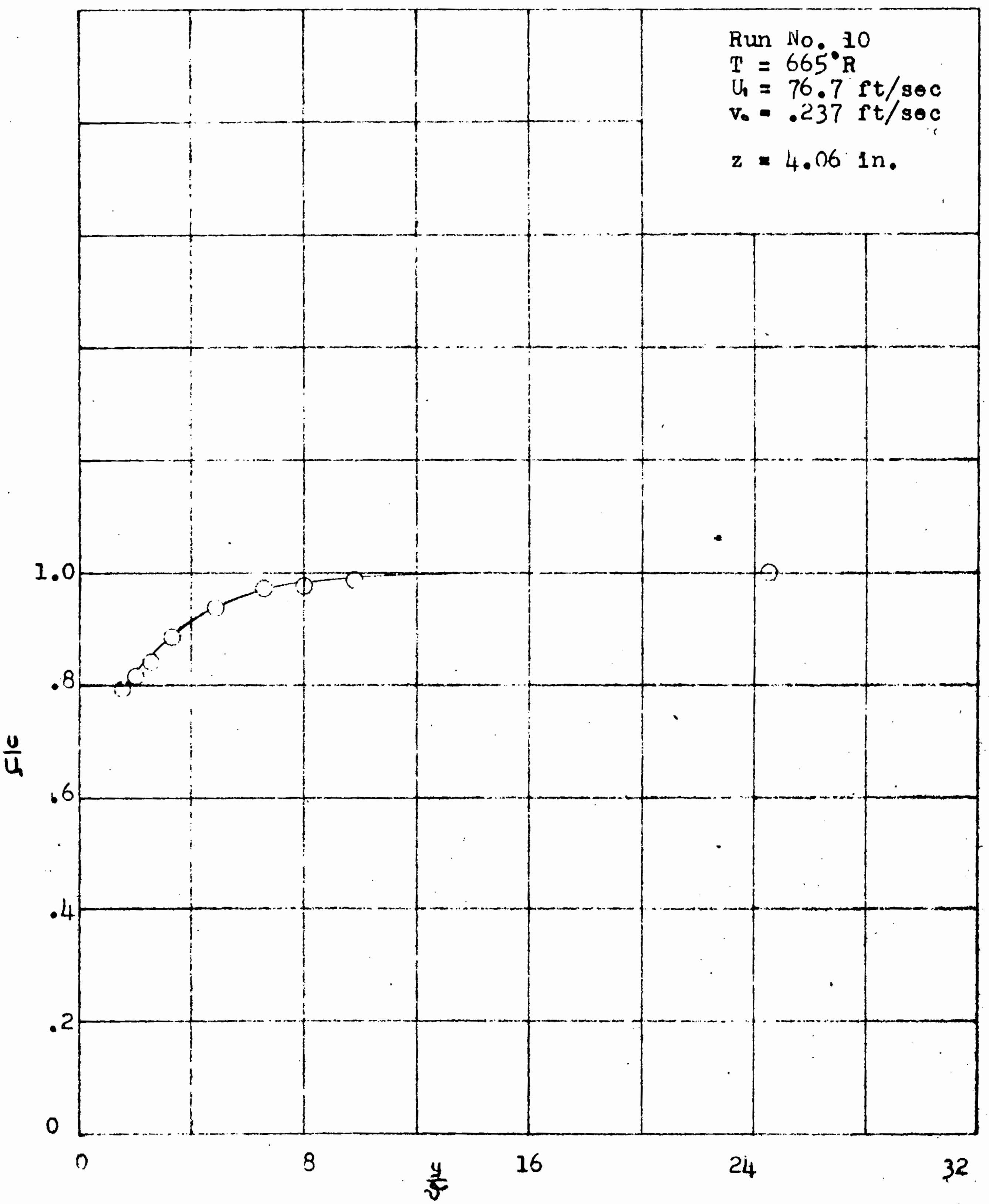

FIGURE 42. VELOCITY PROFILE

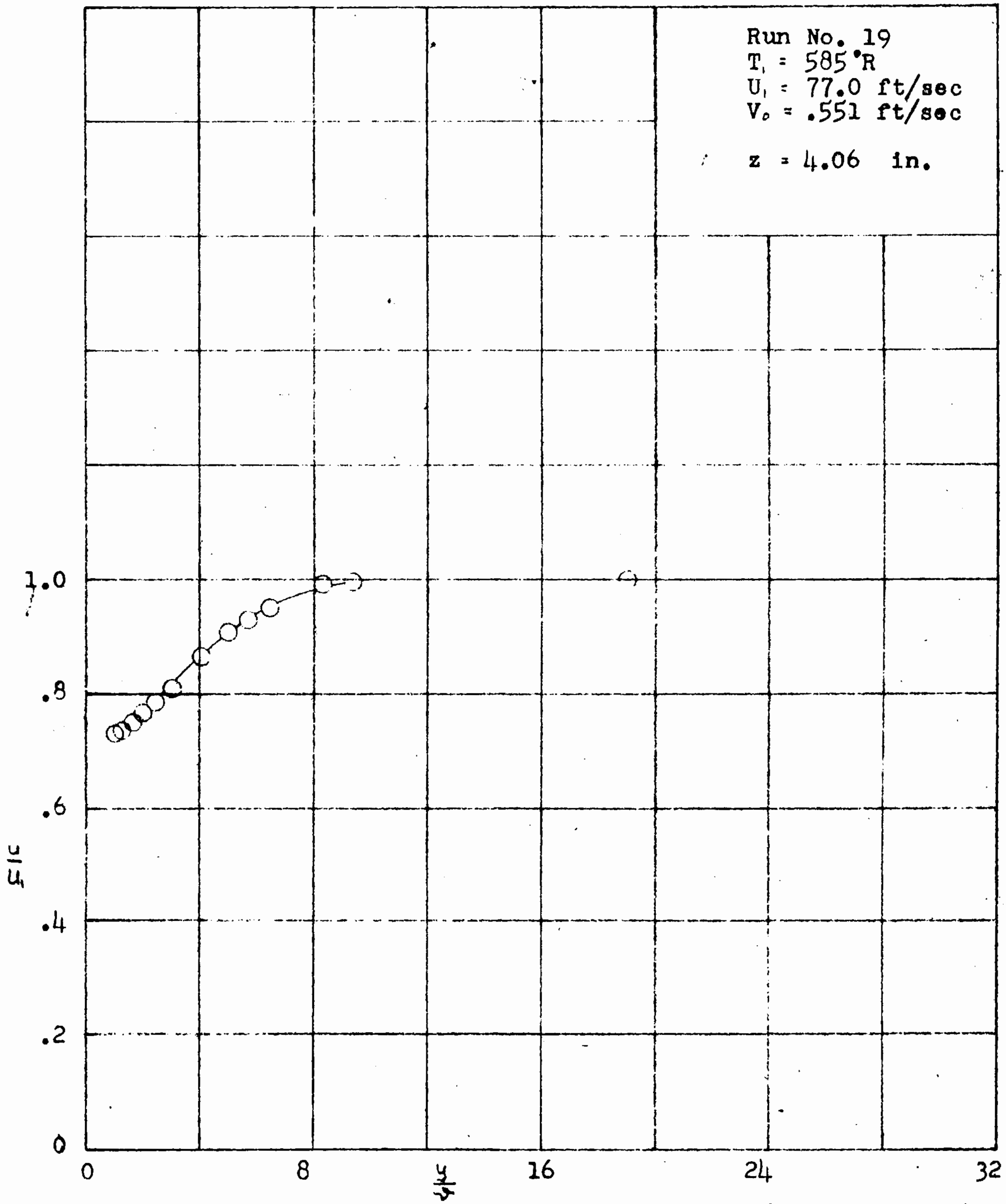

FIGURE 43. VELOCITY PROFILE

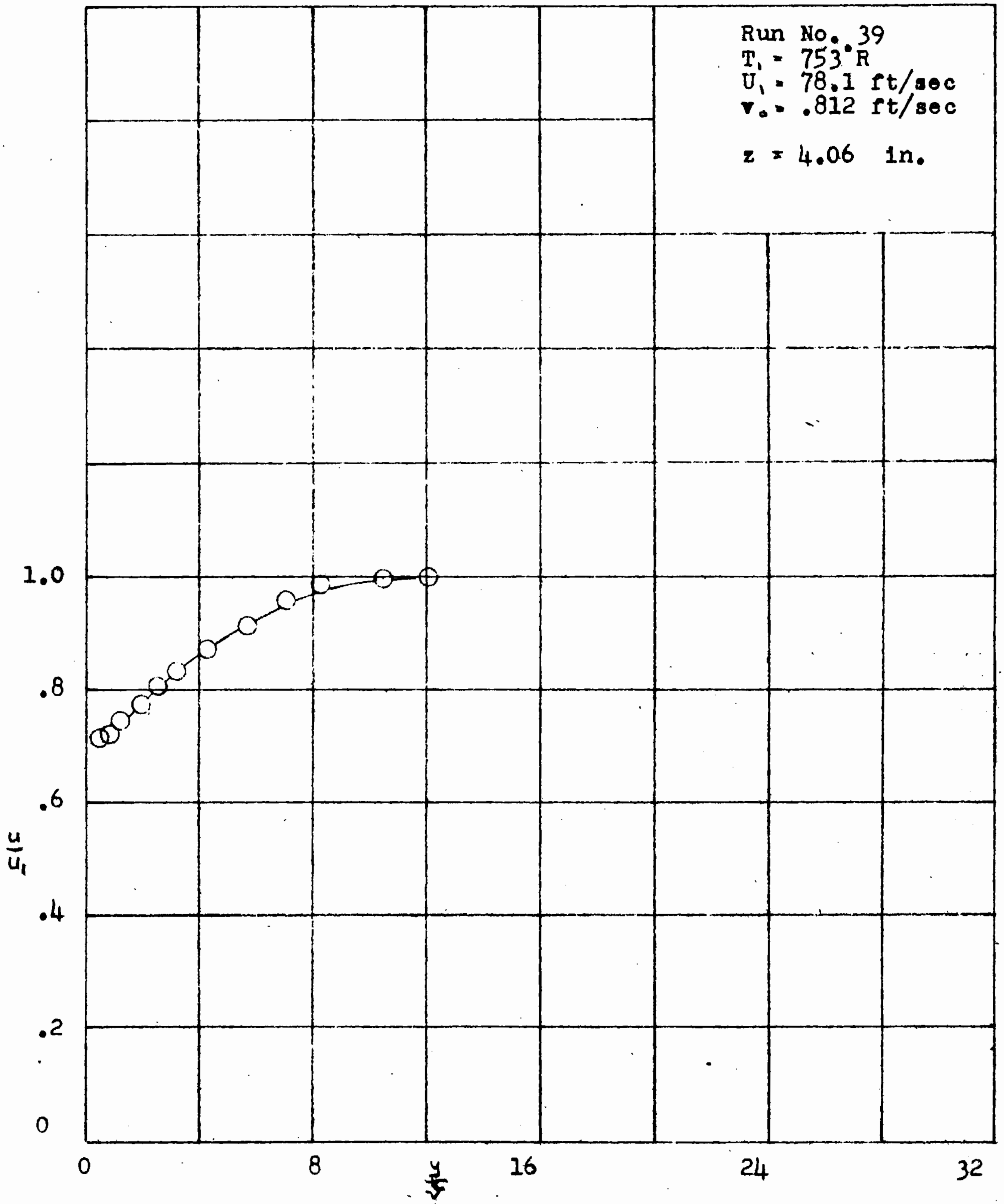

FIGURE 44. VELOCITY PROFILE

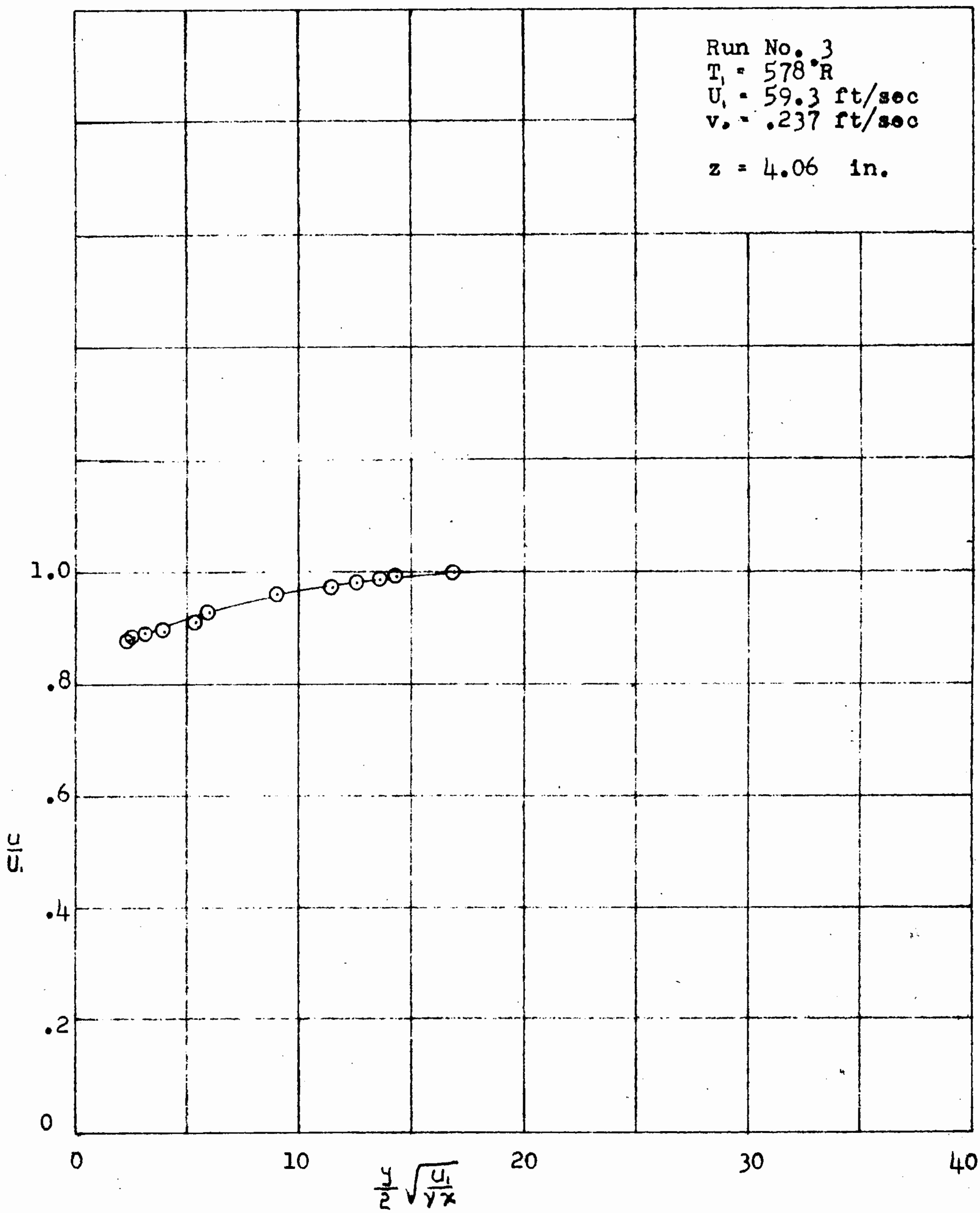

FIGURE 45. VELOCITY PROFILE

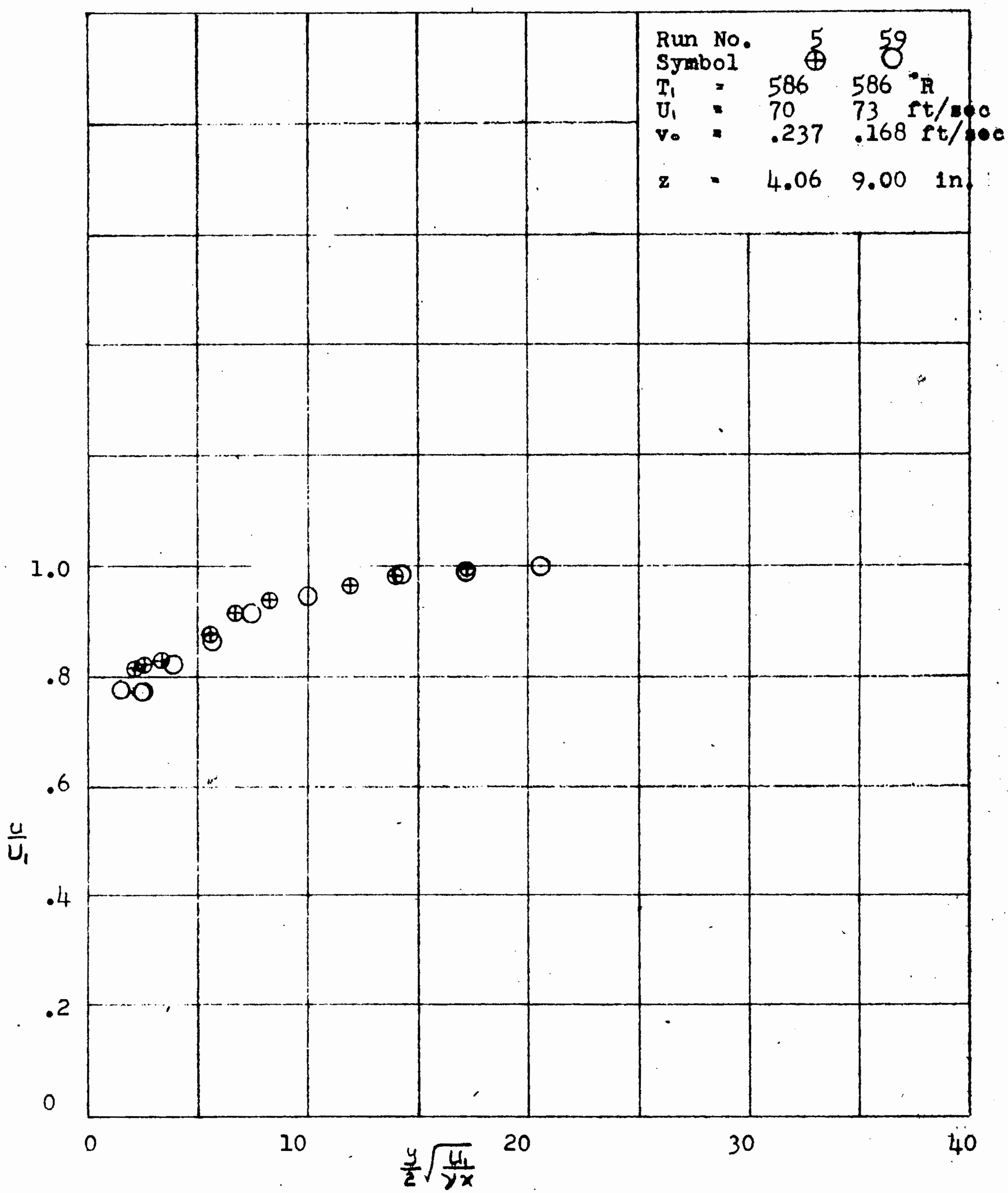

FIGURE 46. VELOCITY PROFILE

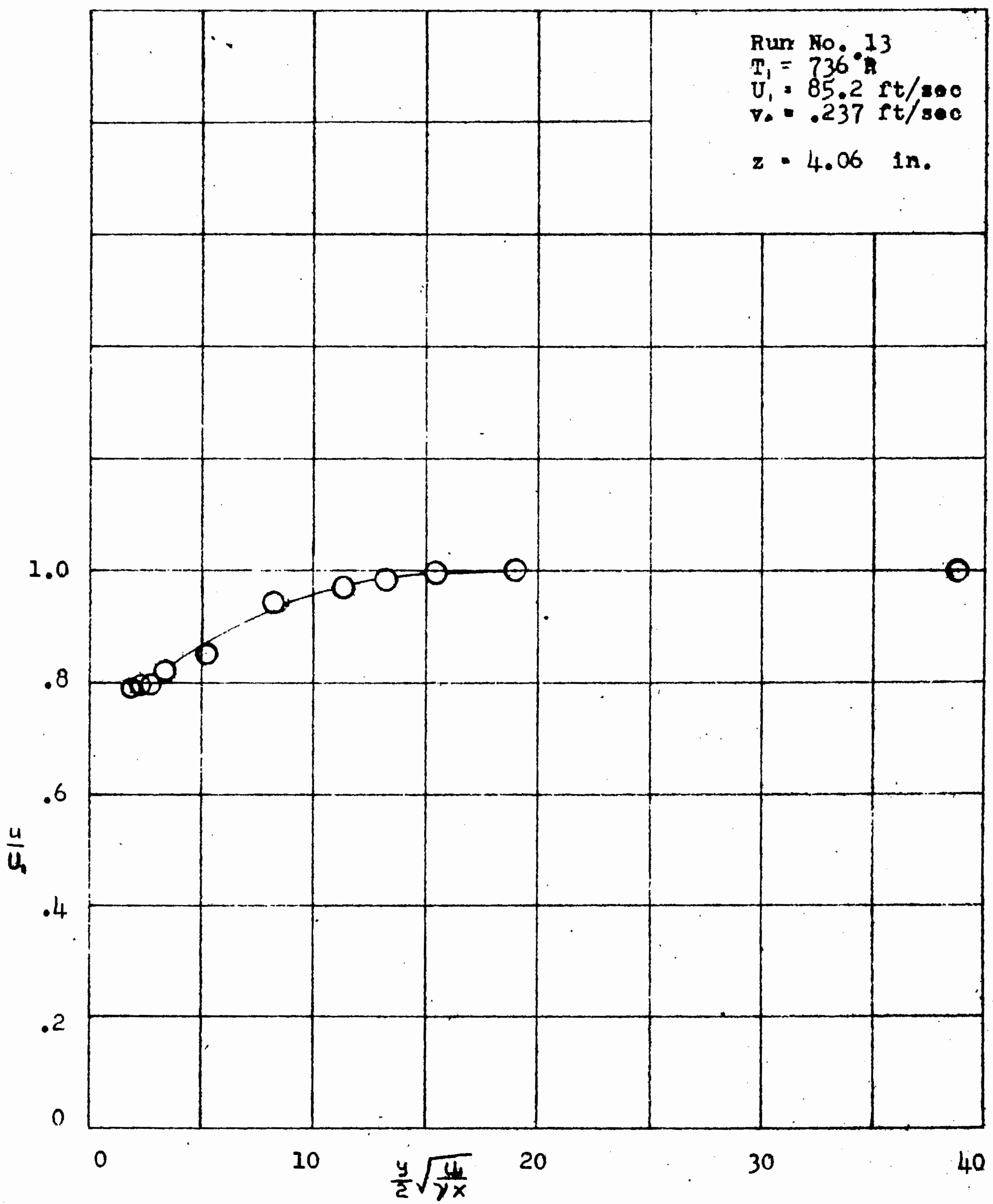

FIGURE 47. VELOCITY PROFILE

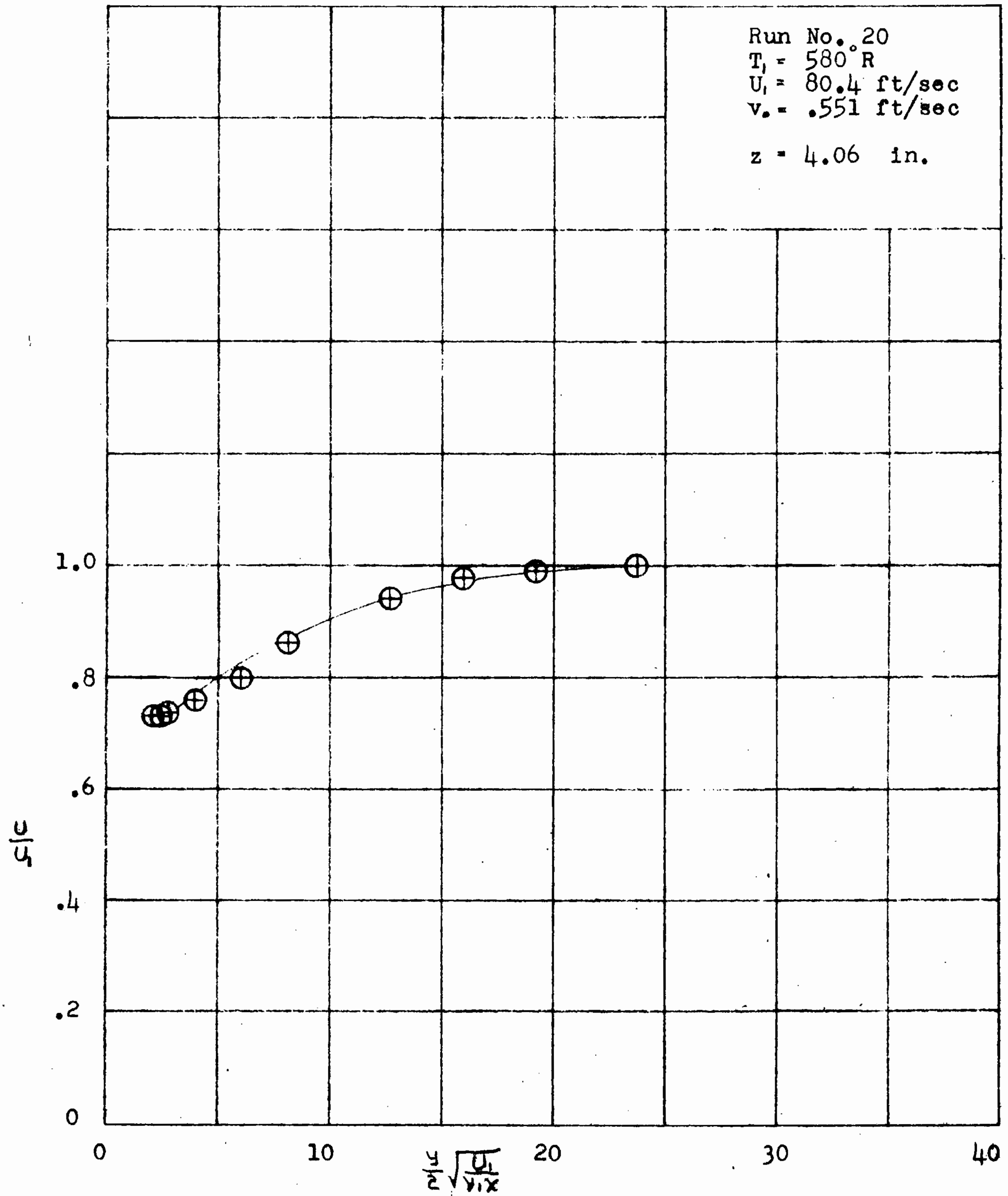

FIGURE 48. VELOCITY PROFILE

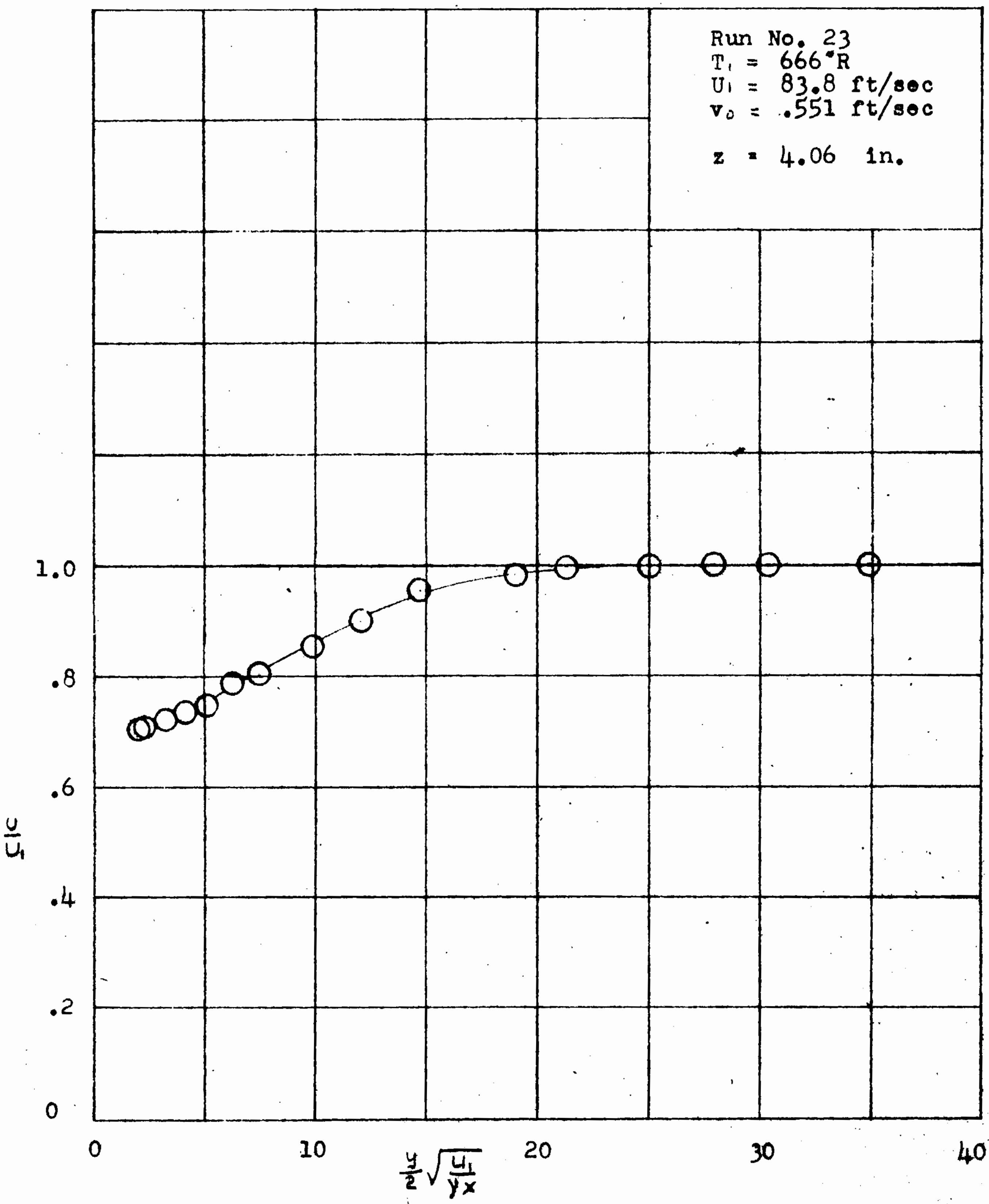

FIGURE 49. VELOCITY PROFILE

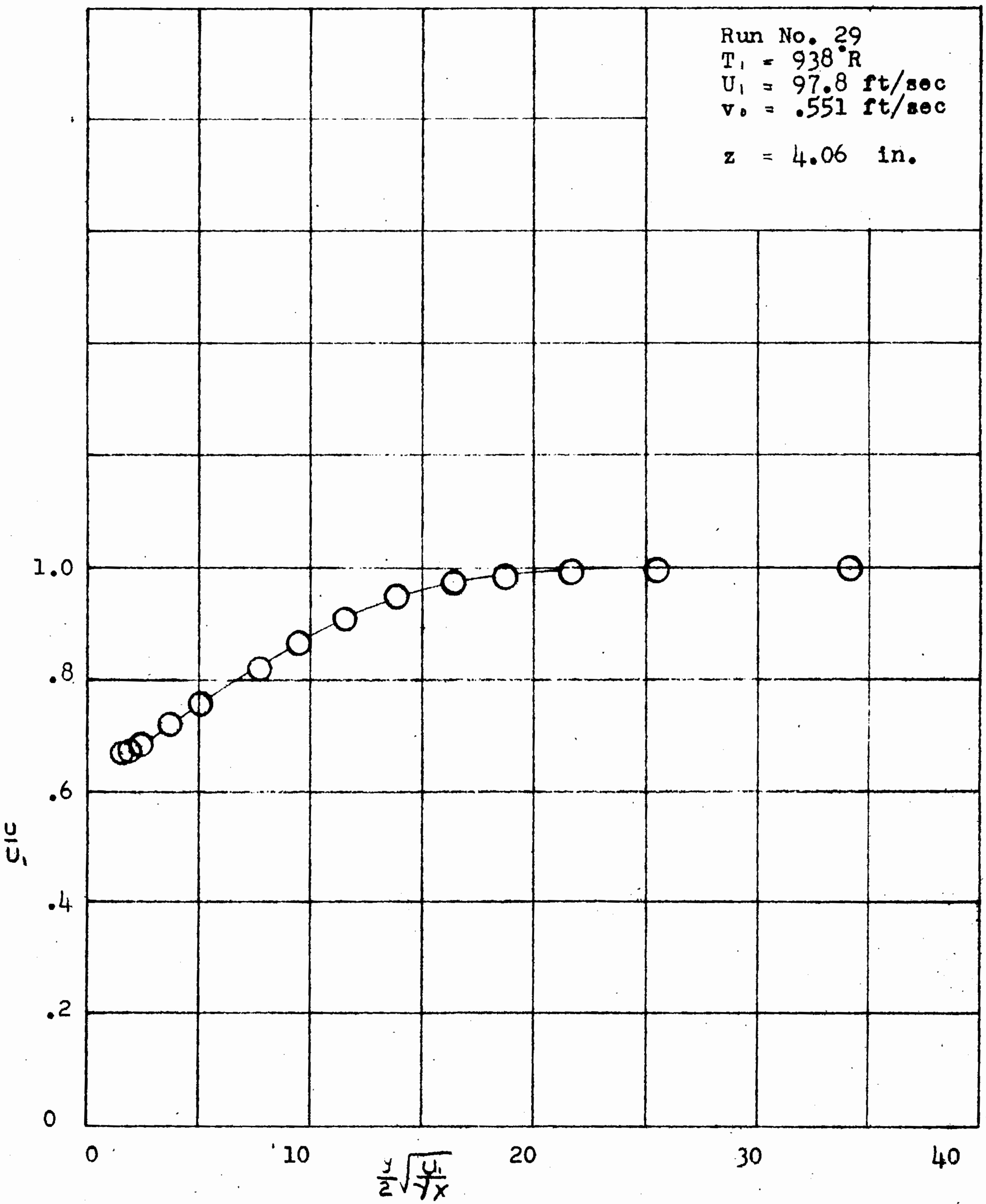

FIGURE 50. VELOCITY PROFILE

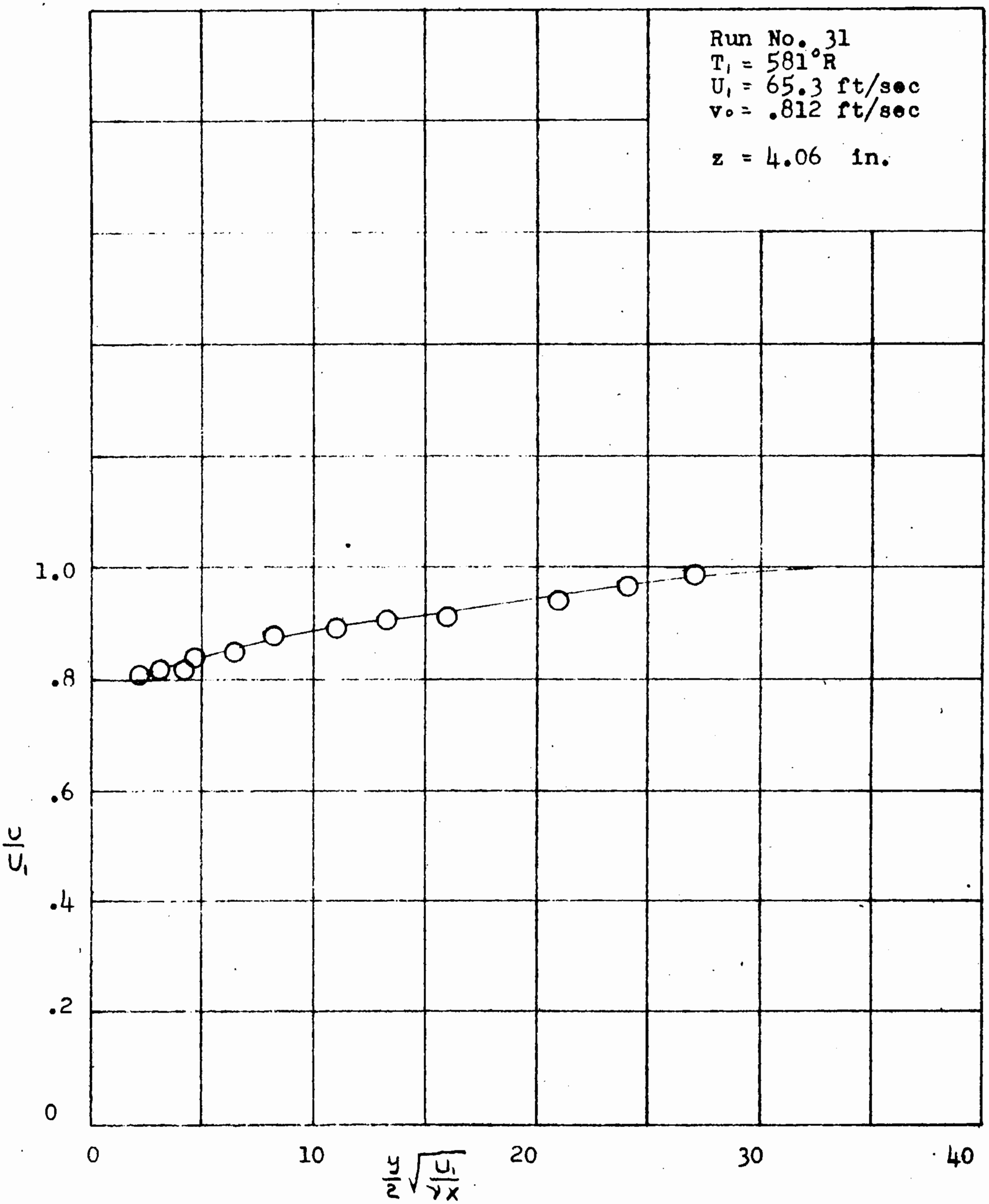

FIGURE 51. VELOCITY PROFILE

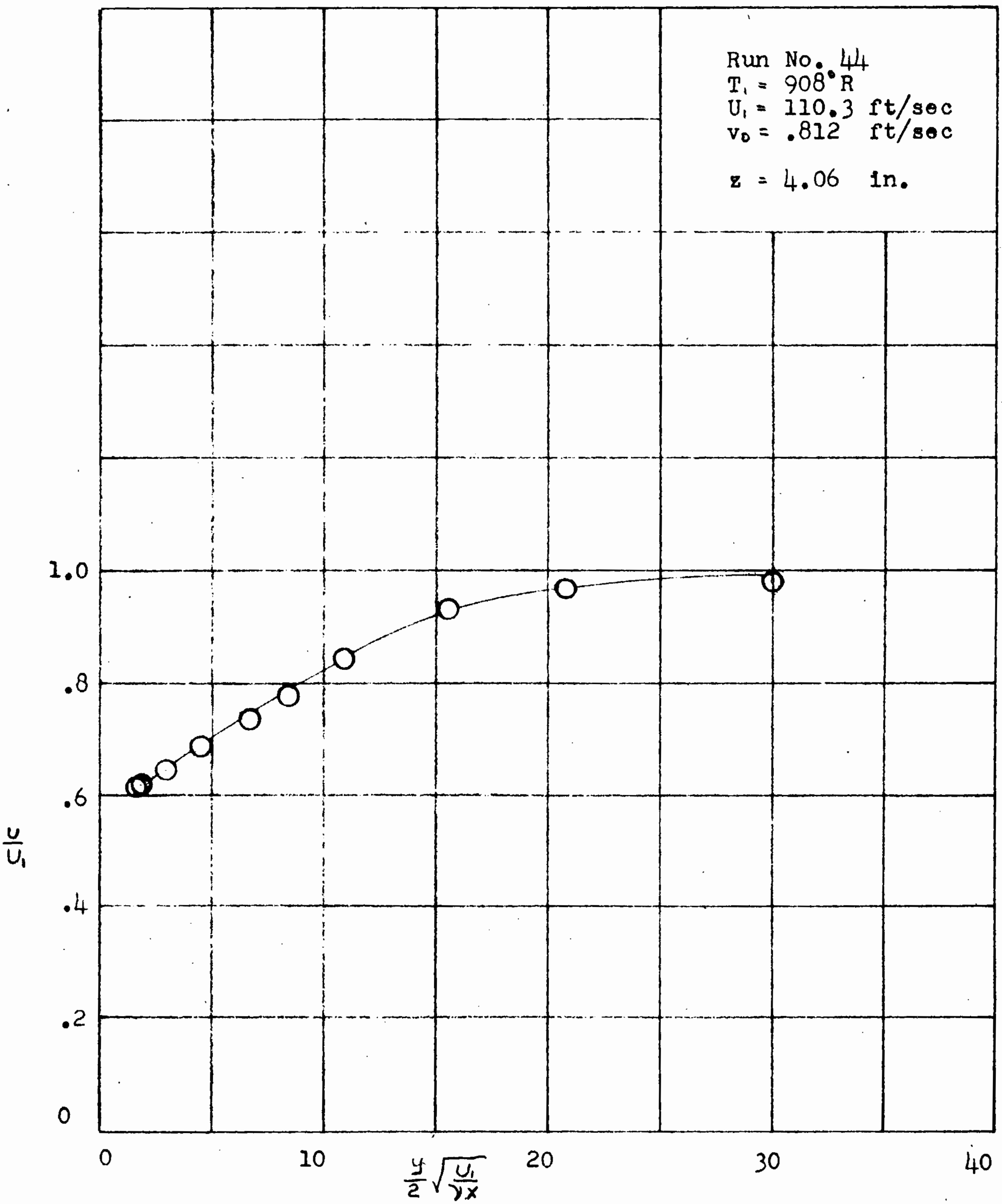

FIGURE 52. VELOCITY PROFILE

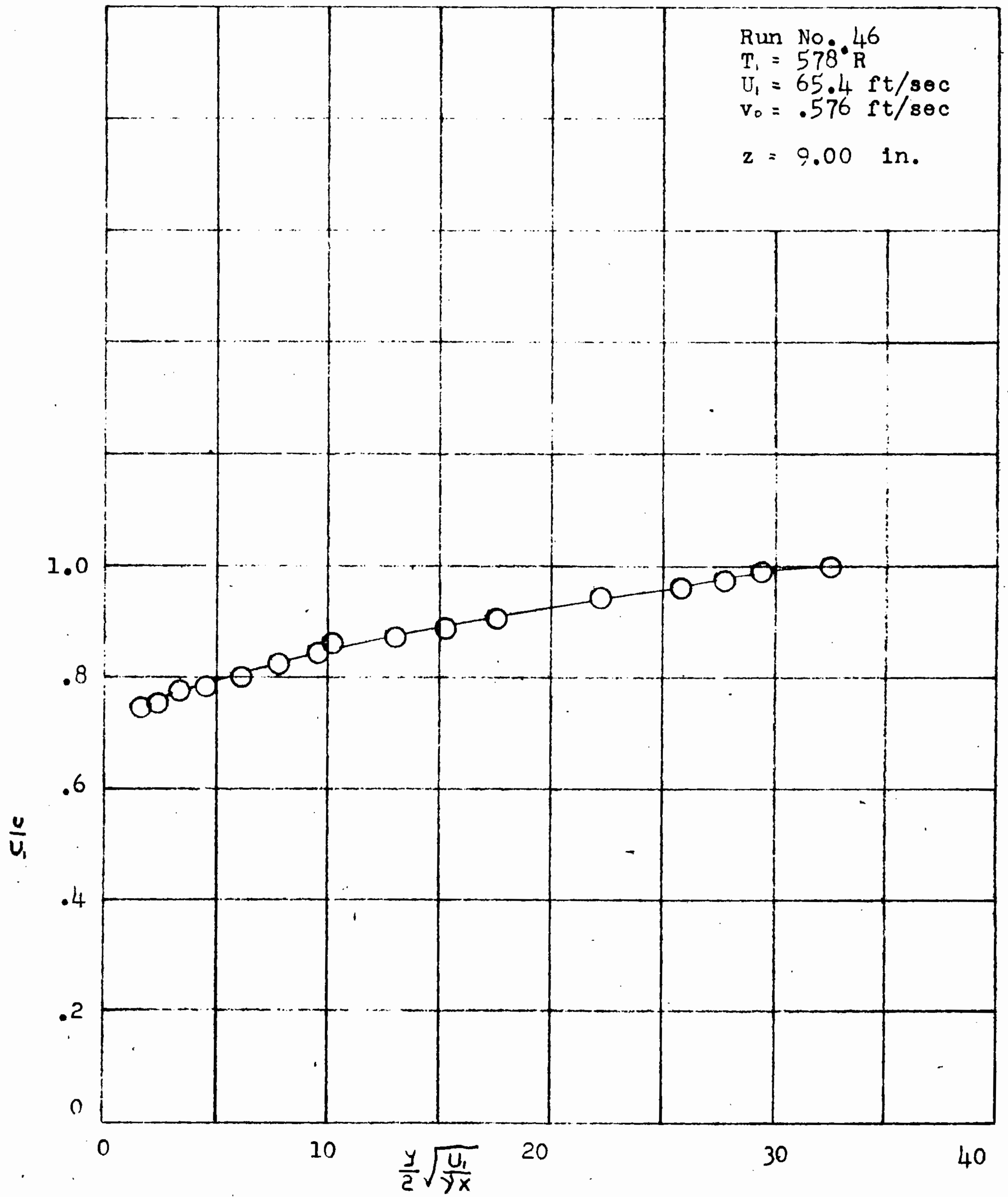

FIGURE 53. VELOCITY PROFILE

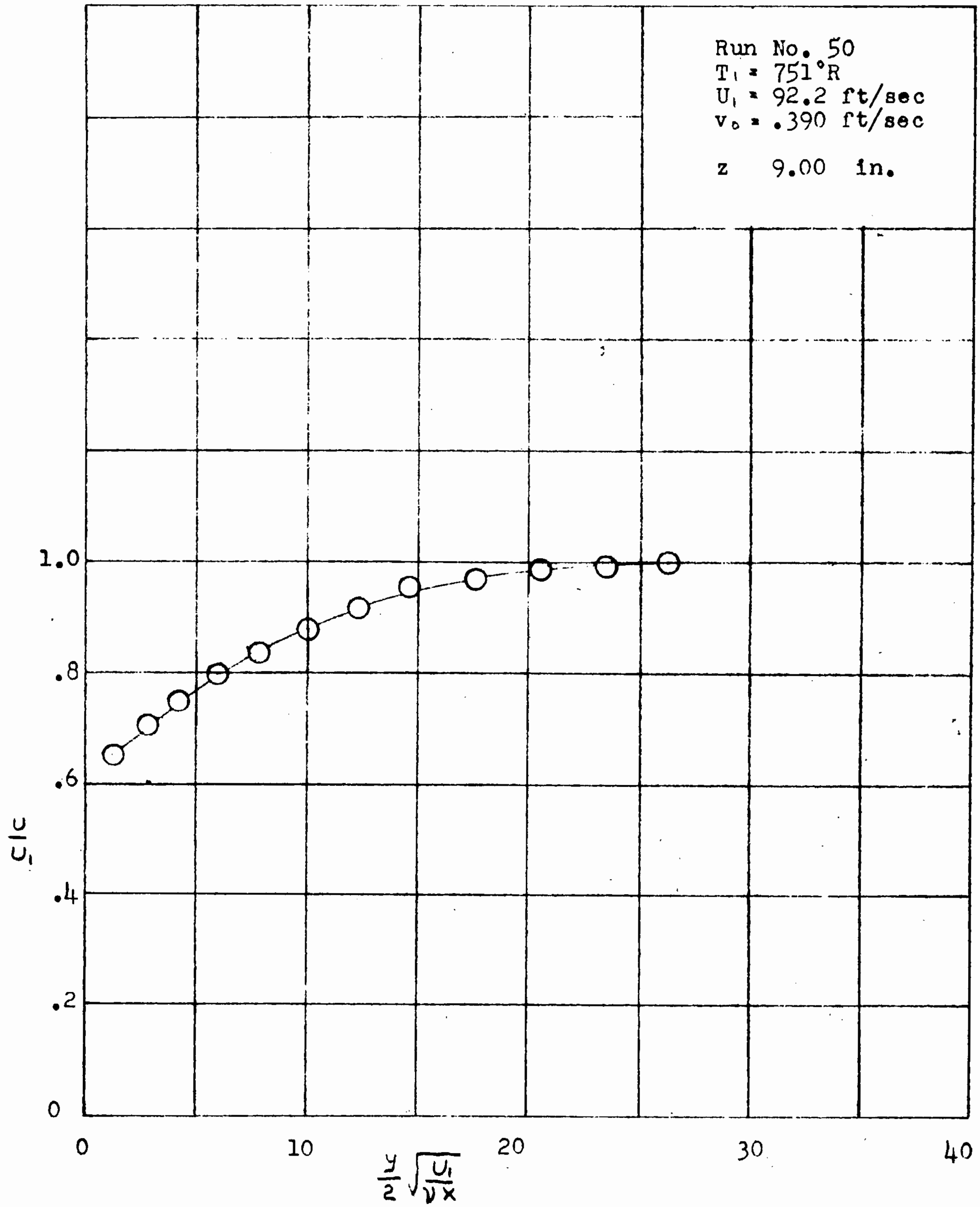

FIGURE 54. VELOCITY PROFILE

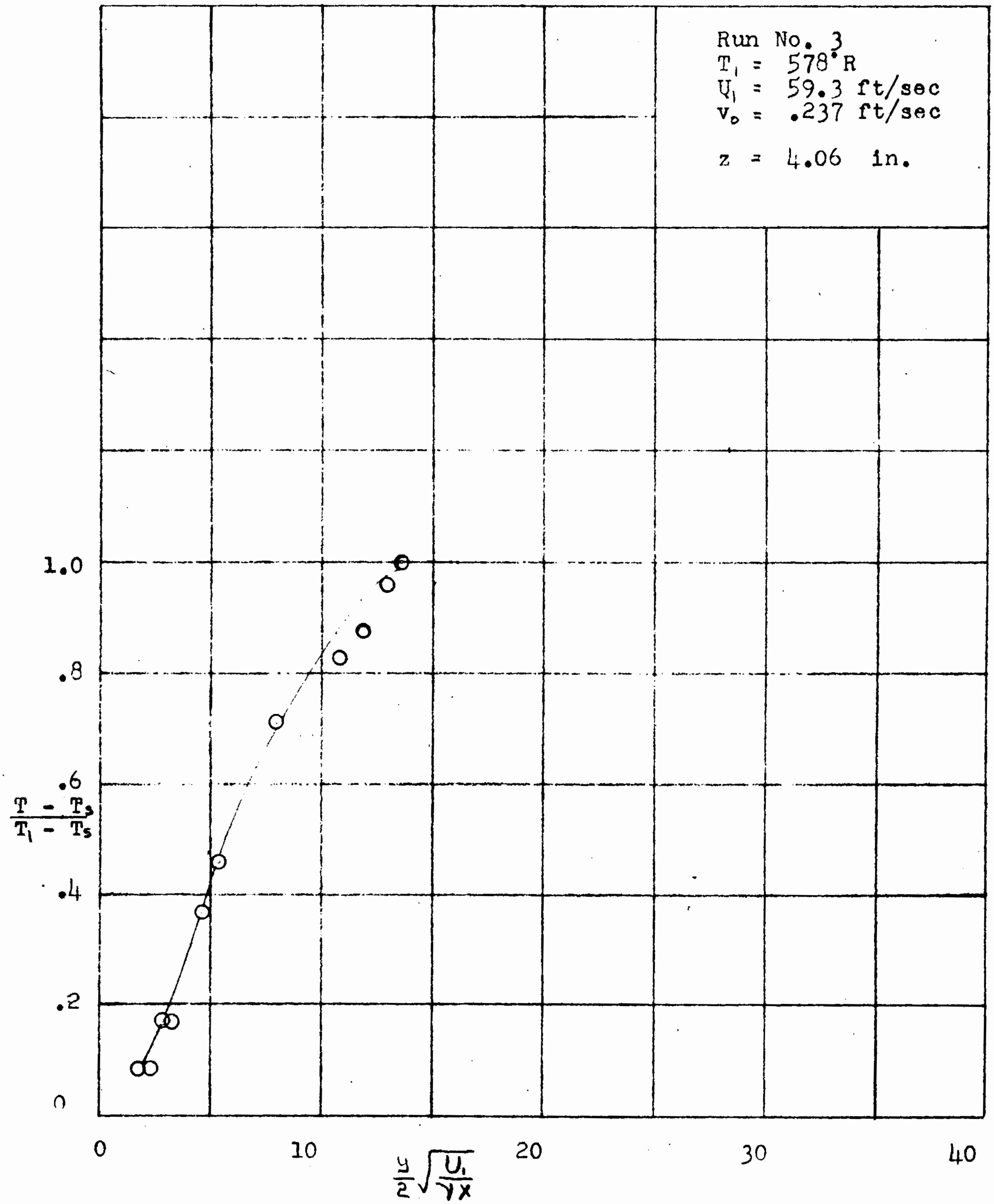

FIGURE 55. TEMPERATURE PROFILE

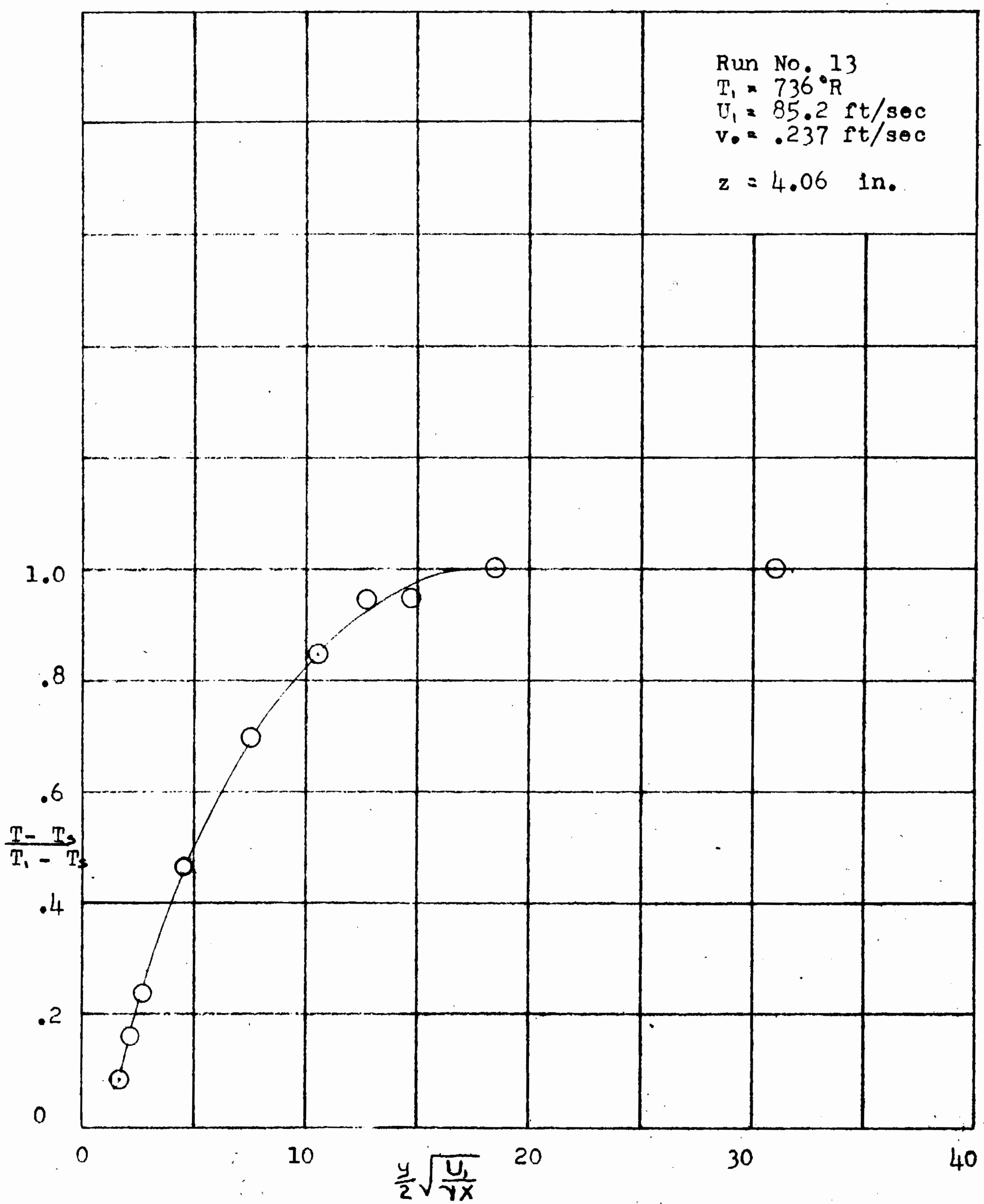

FIGURE 56. TEMPERATURE PROFILE

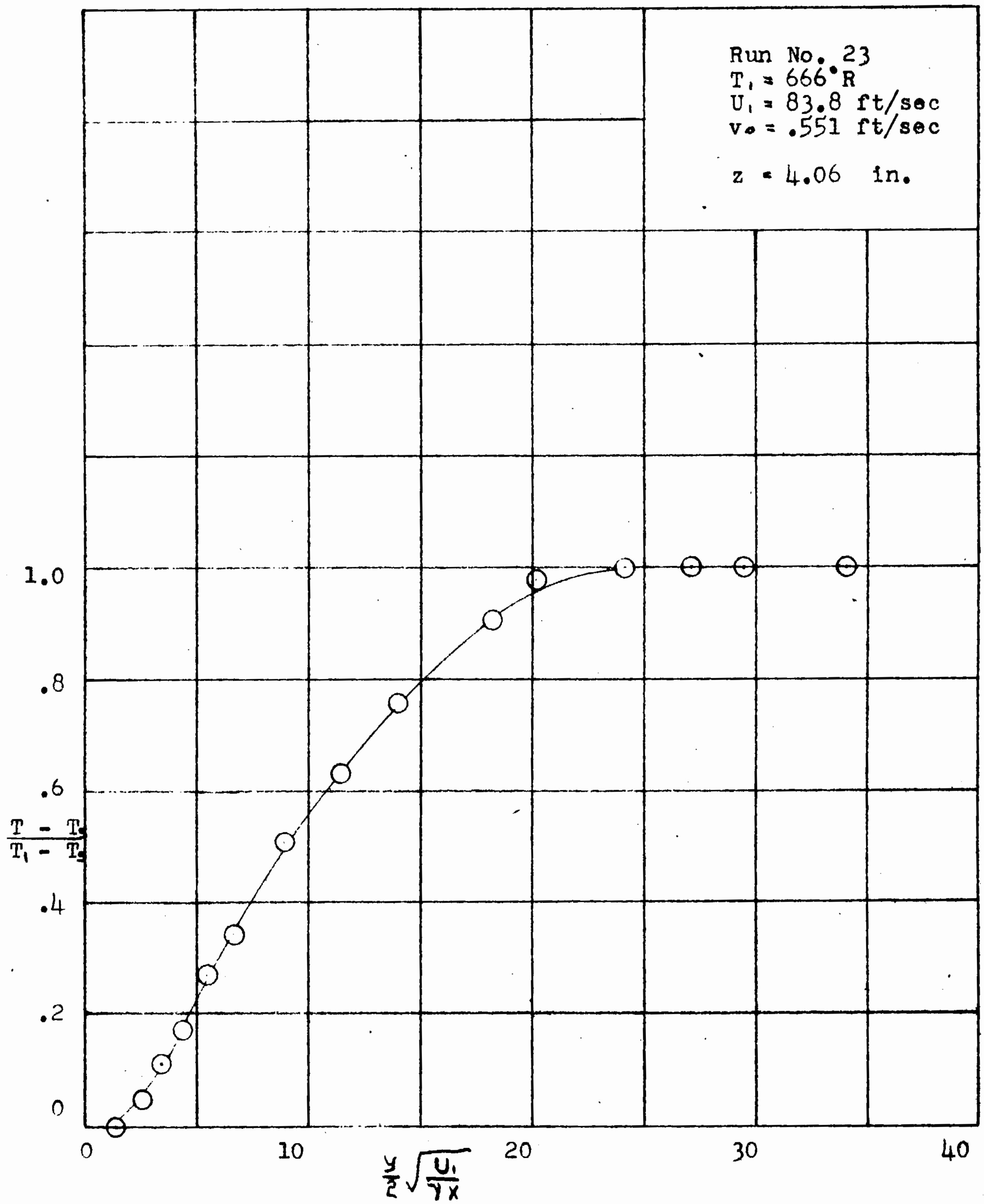

FIGURE 57. TEMPERATURE PROFILE

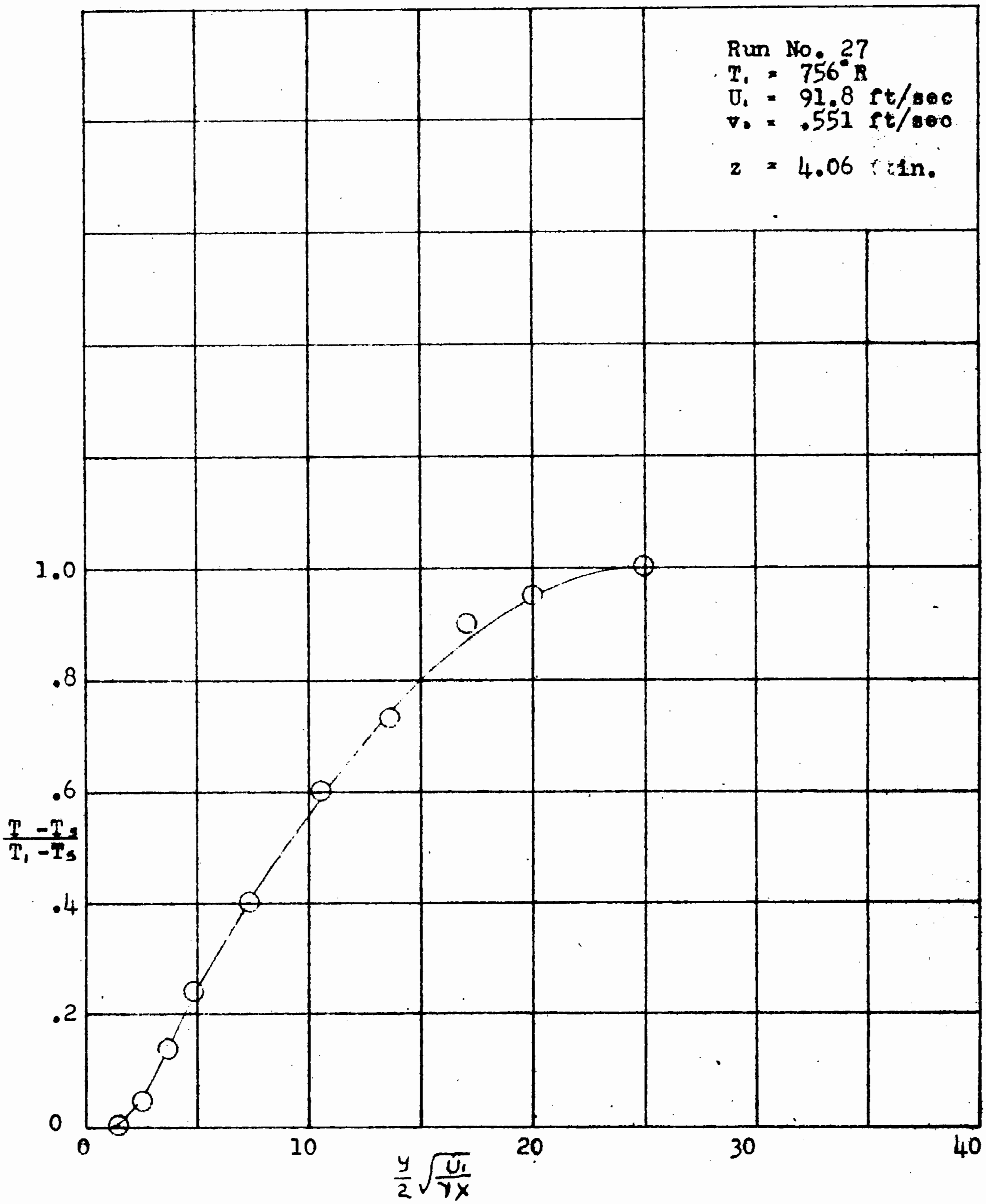

FIGURE 58. TEMPERATURE PROFILE

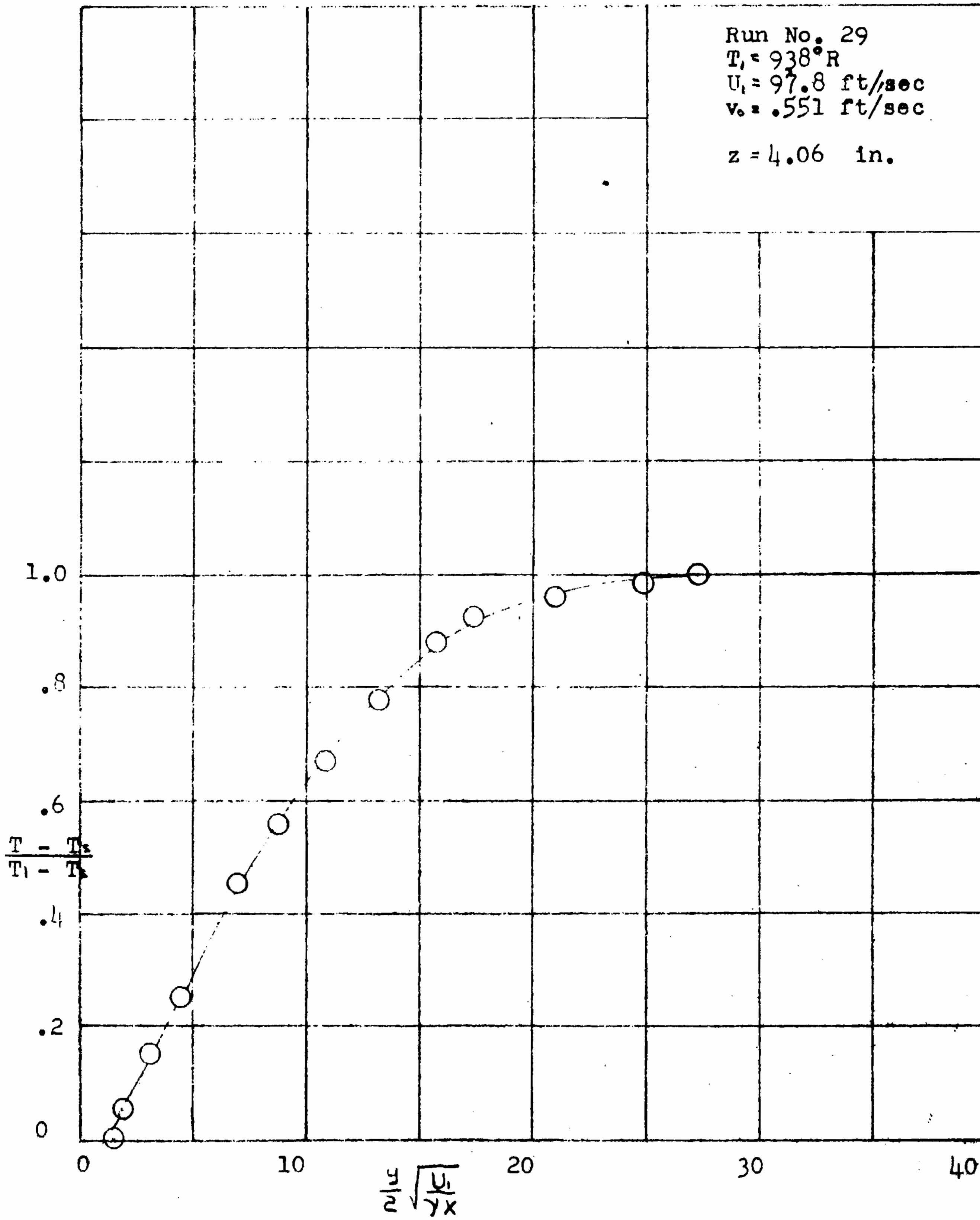

FIGURE 59. TEMPERATURE PROFILE

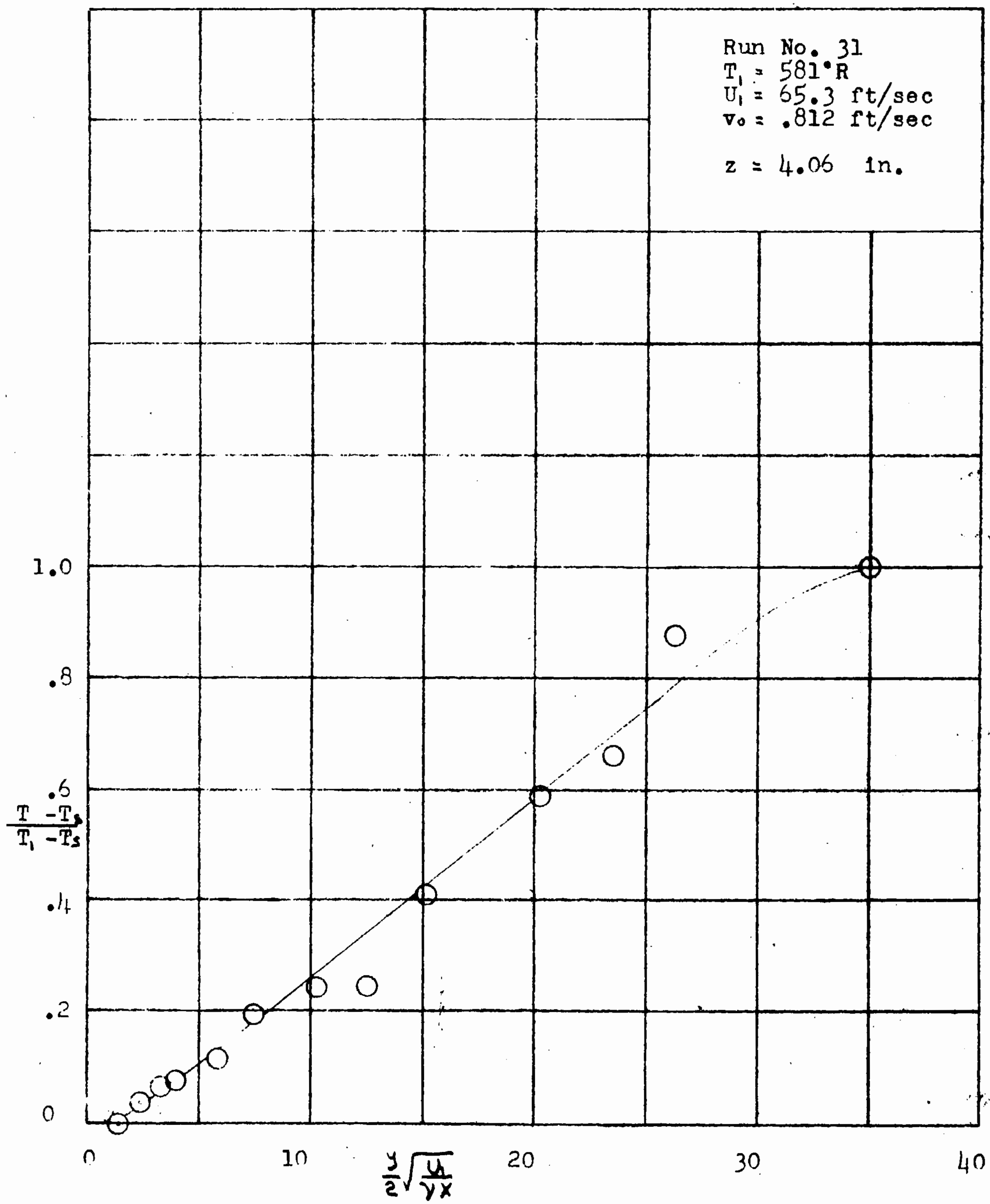

FIGURE 60. TEMPERATURE PROFILE

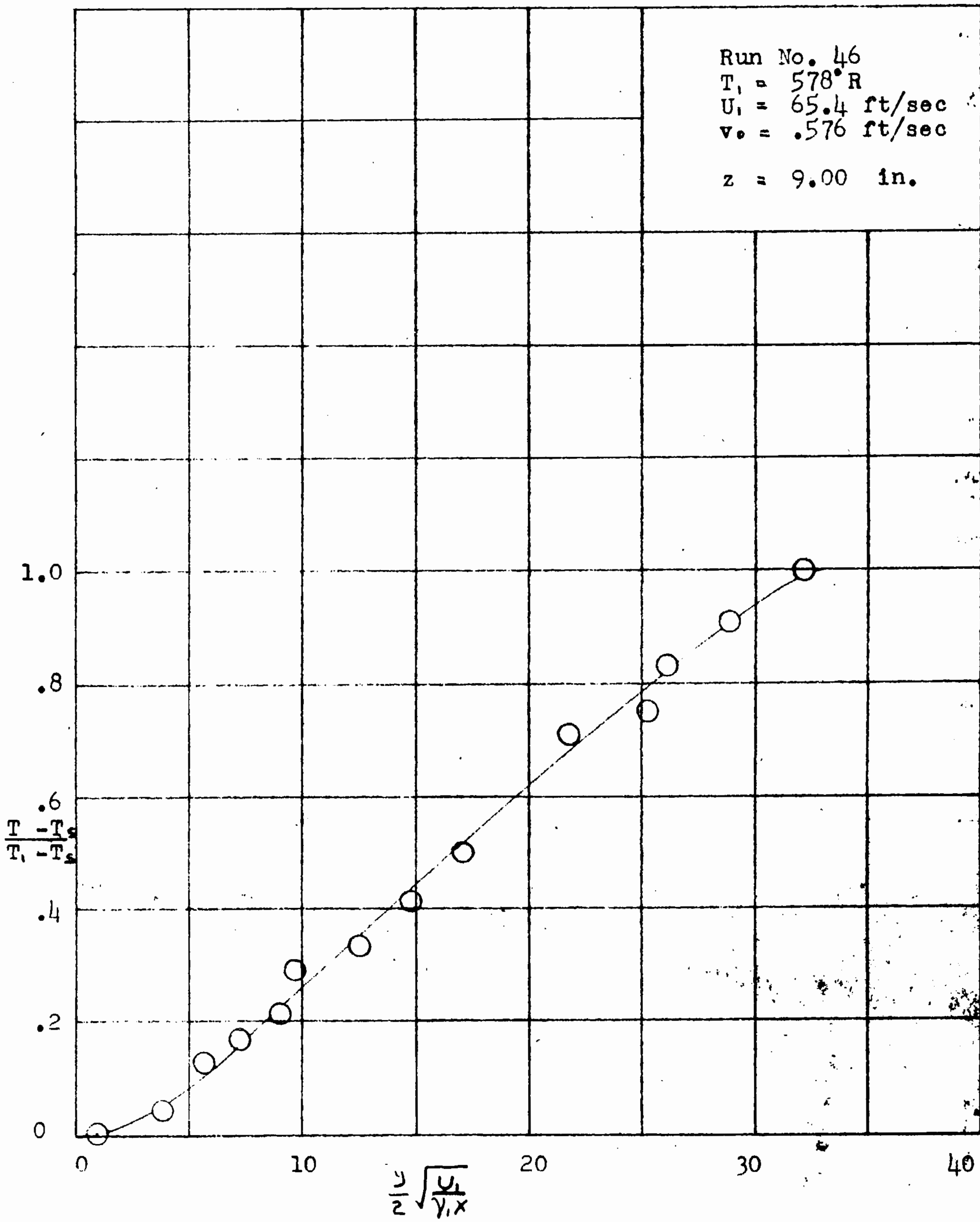

FIGURE 61. TEMPERATURE PROFILE

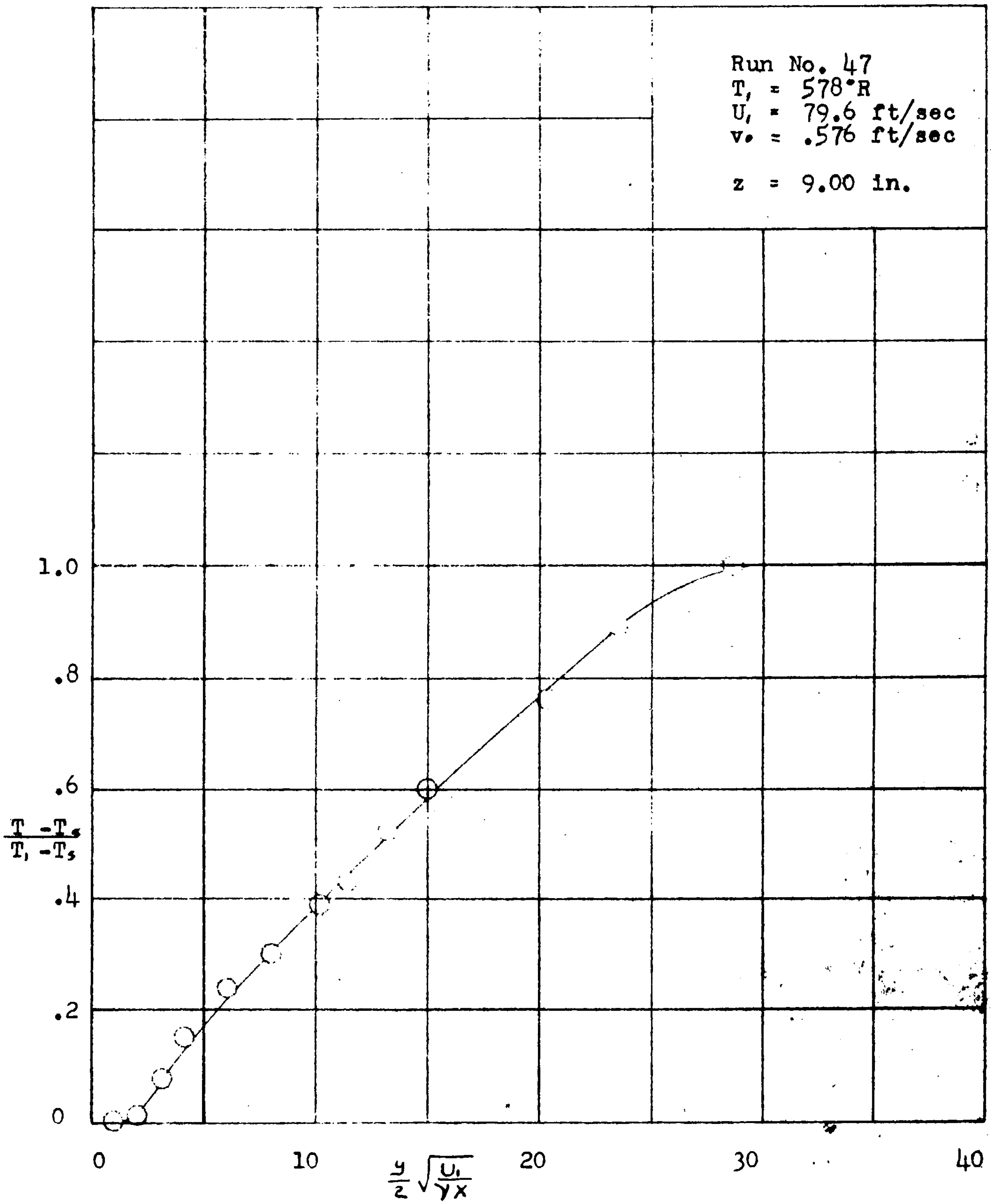

FIGURE 62. TEMPERATURE PROFILE

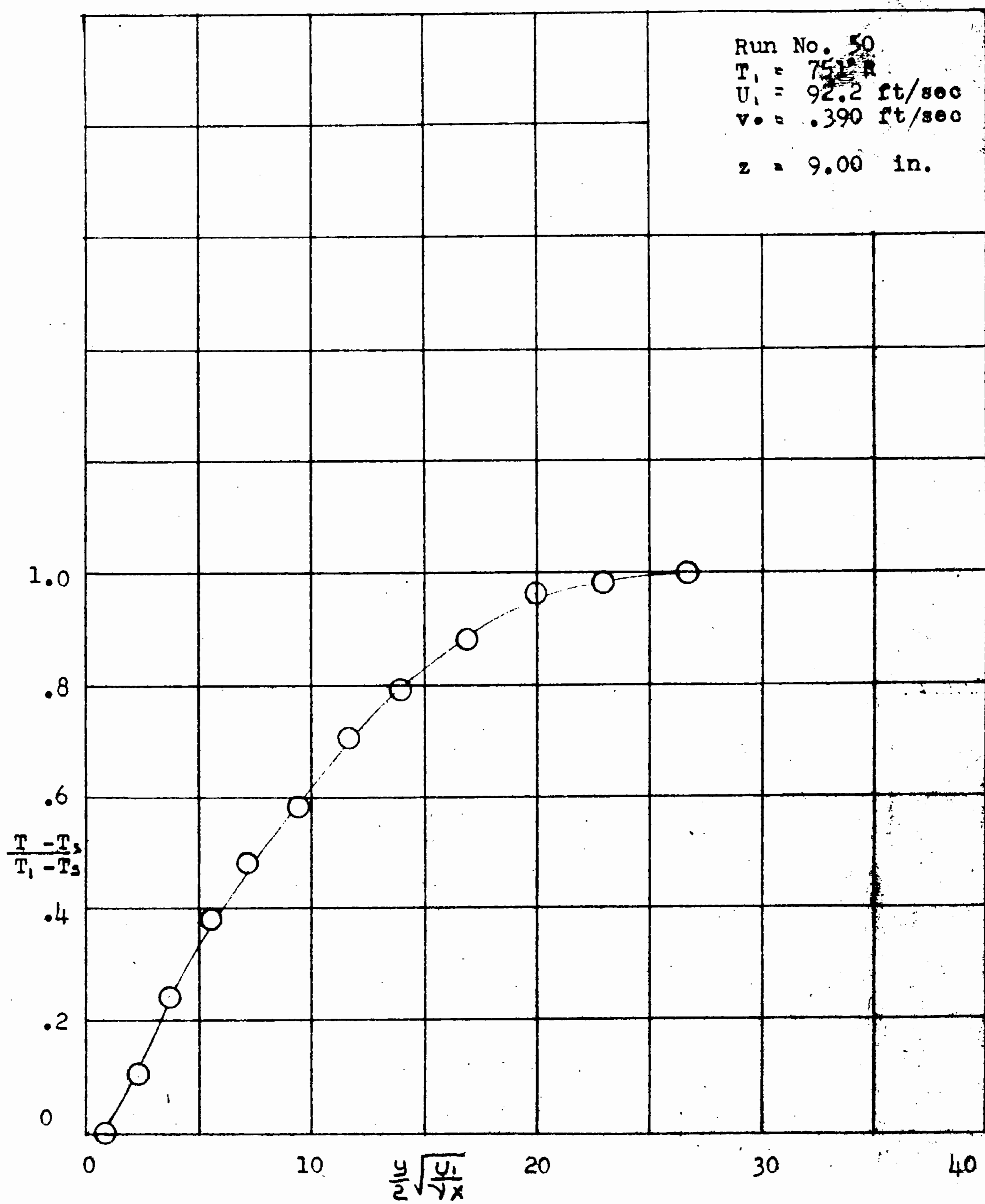

FIGURE 63. TEMPERATURE PROFILE

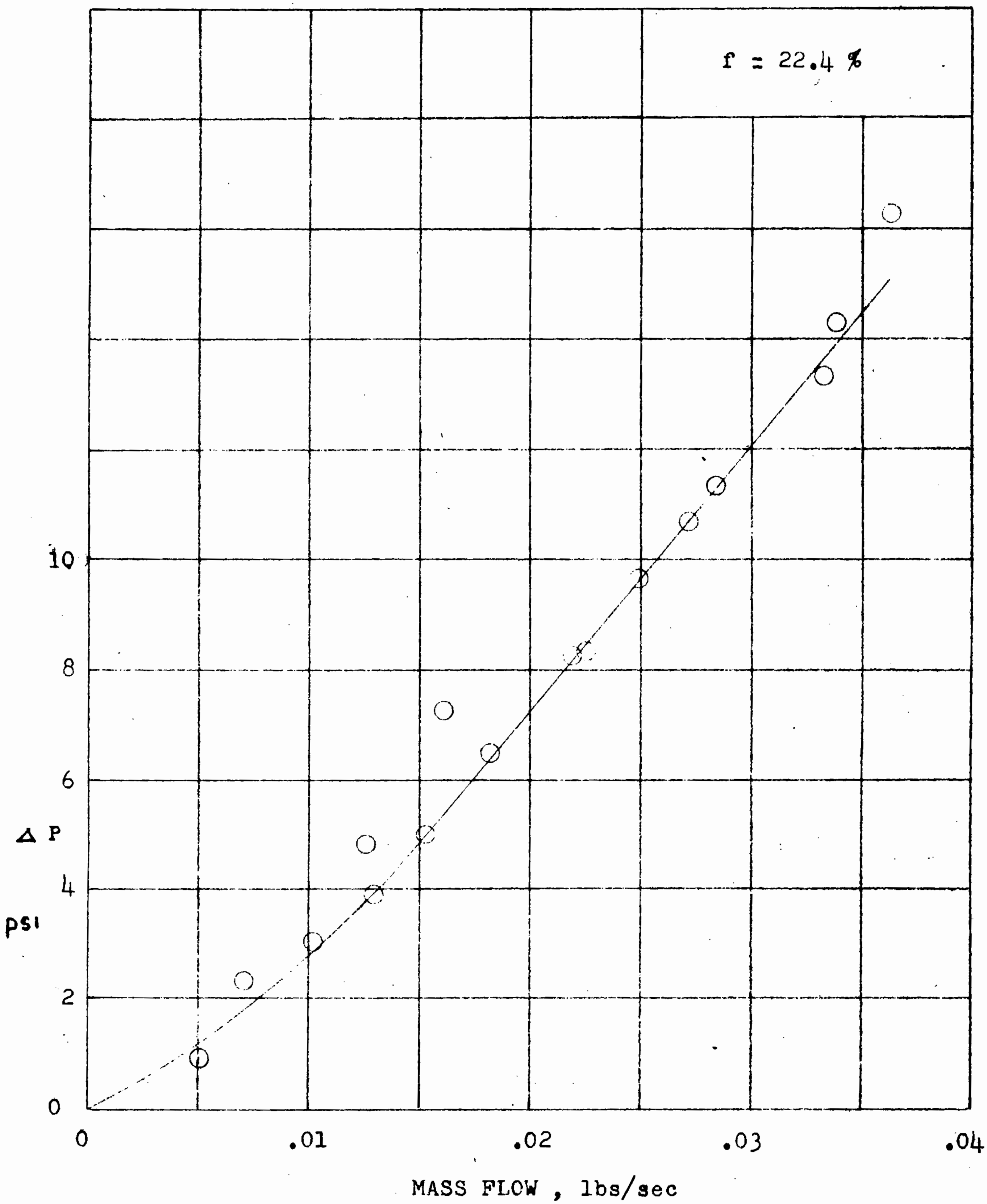

FIGURE 64. PRESSURE DROP AGAINST MASS FLOW

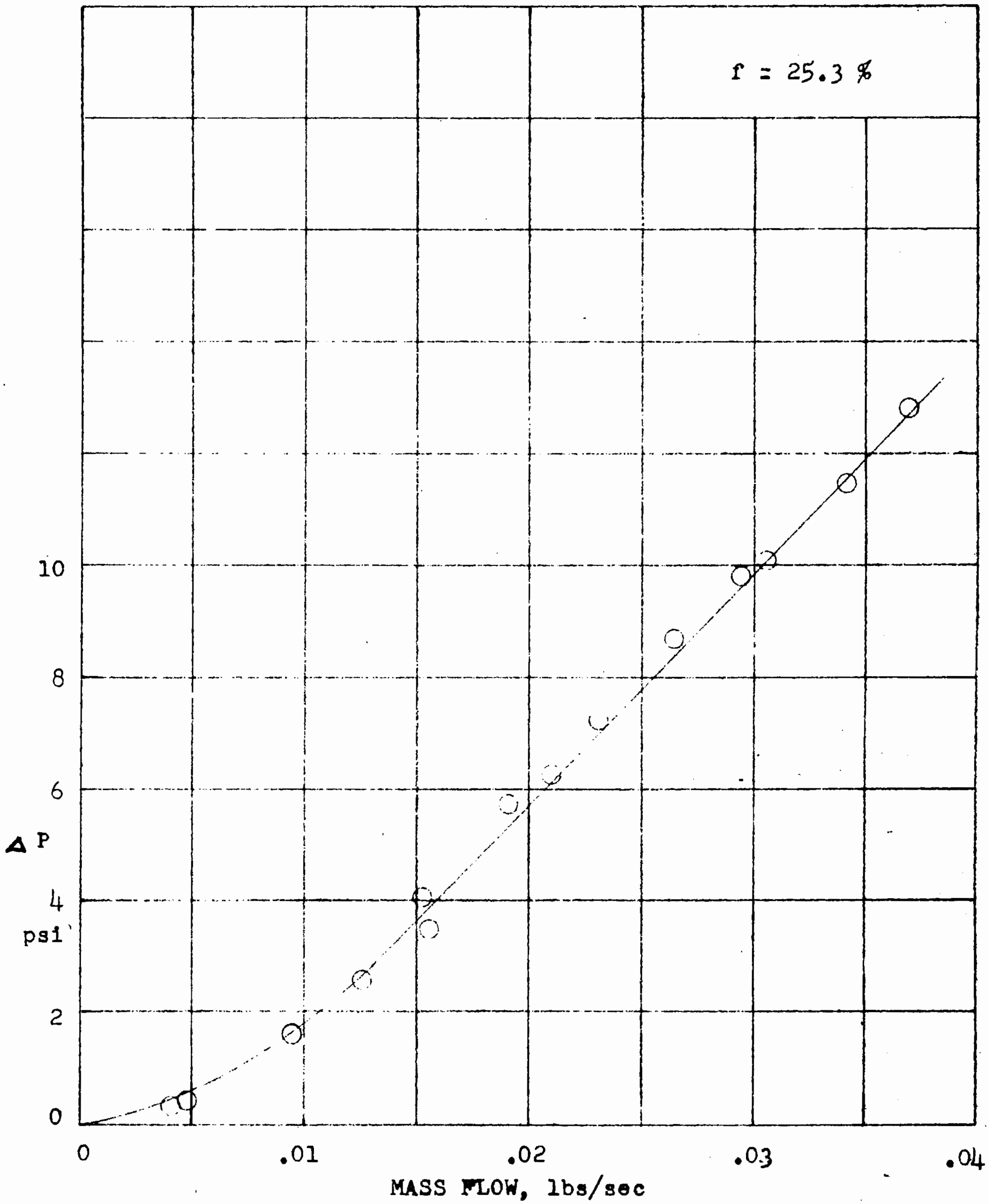

FIGURE. 65. PRESSURE DROP AGAINST MASS FLOW

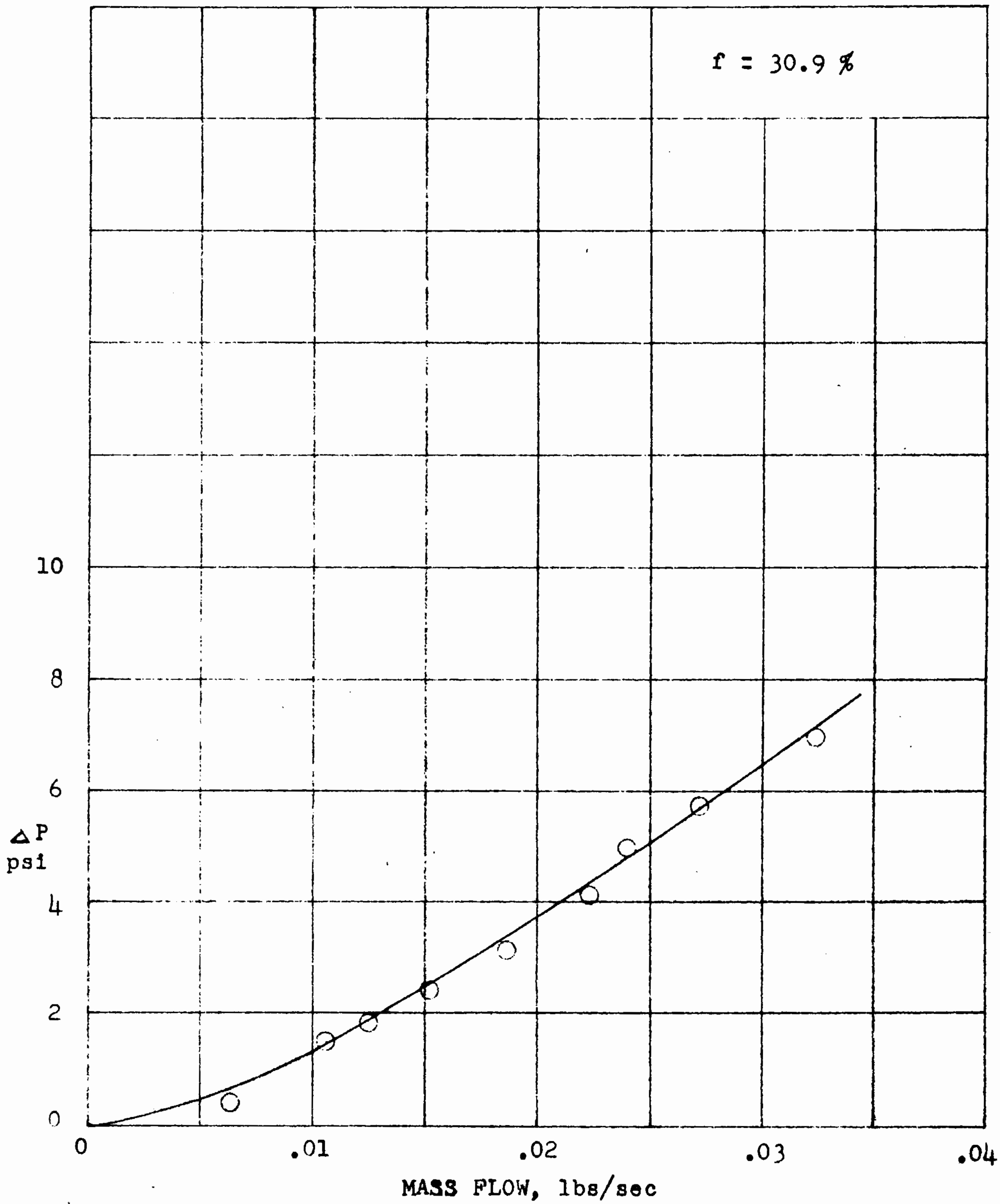

FIGURE 66. PRESSURE DROP AGAINST MASS FLOW

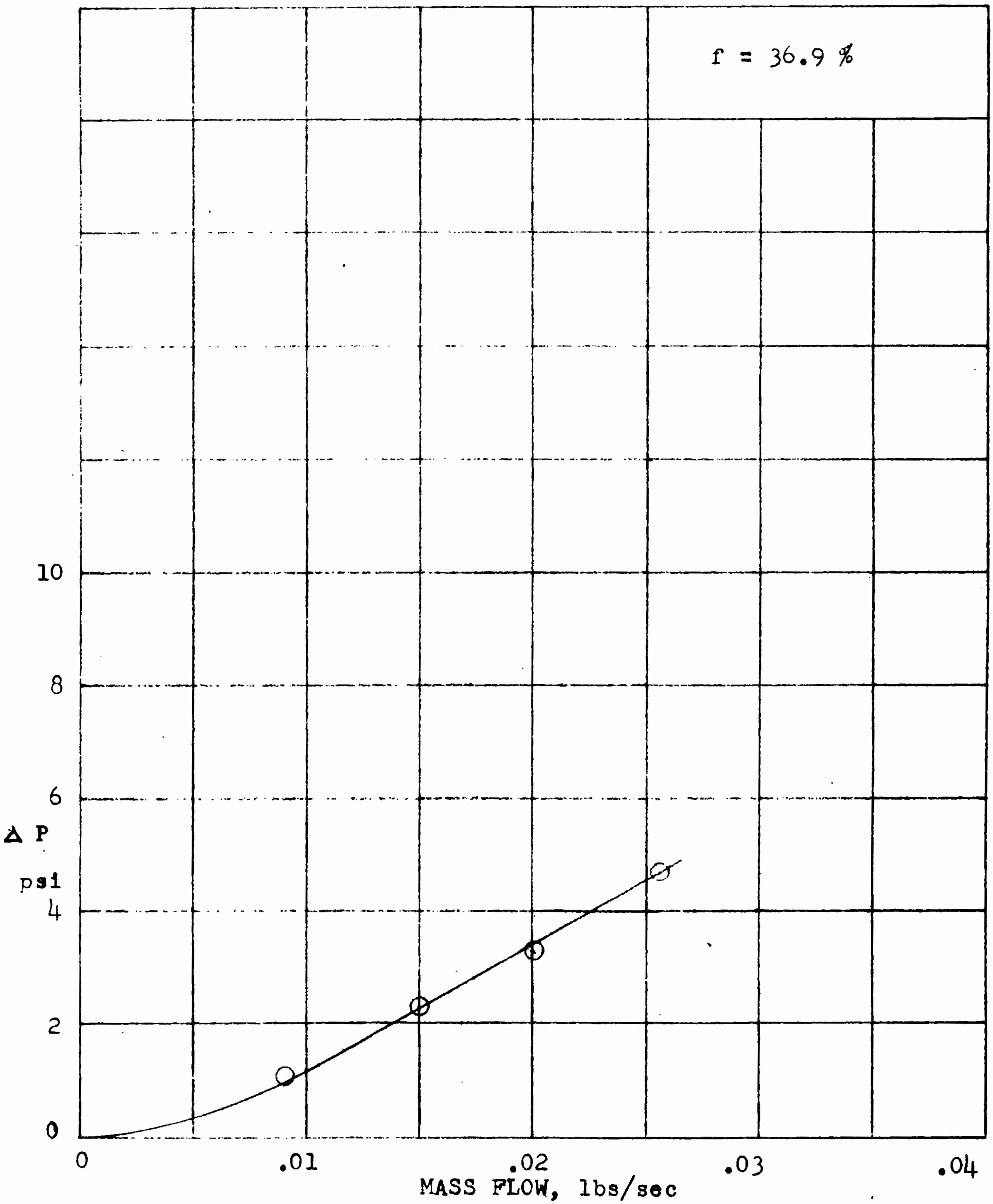

FIGURE 67. PRESSURE DROP AGAINST MASS FLOW

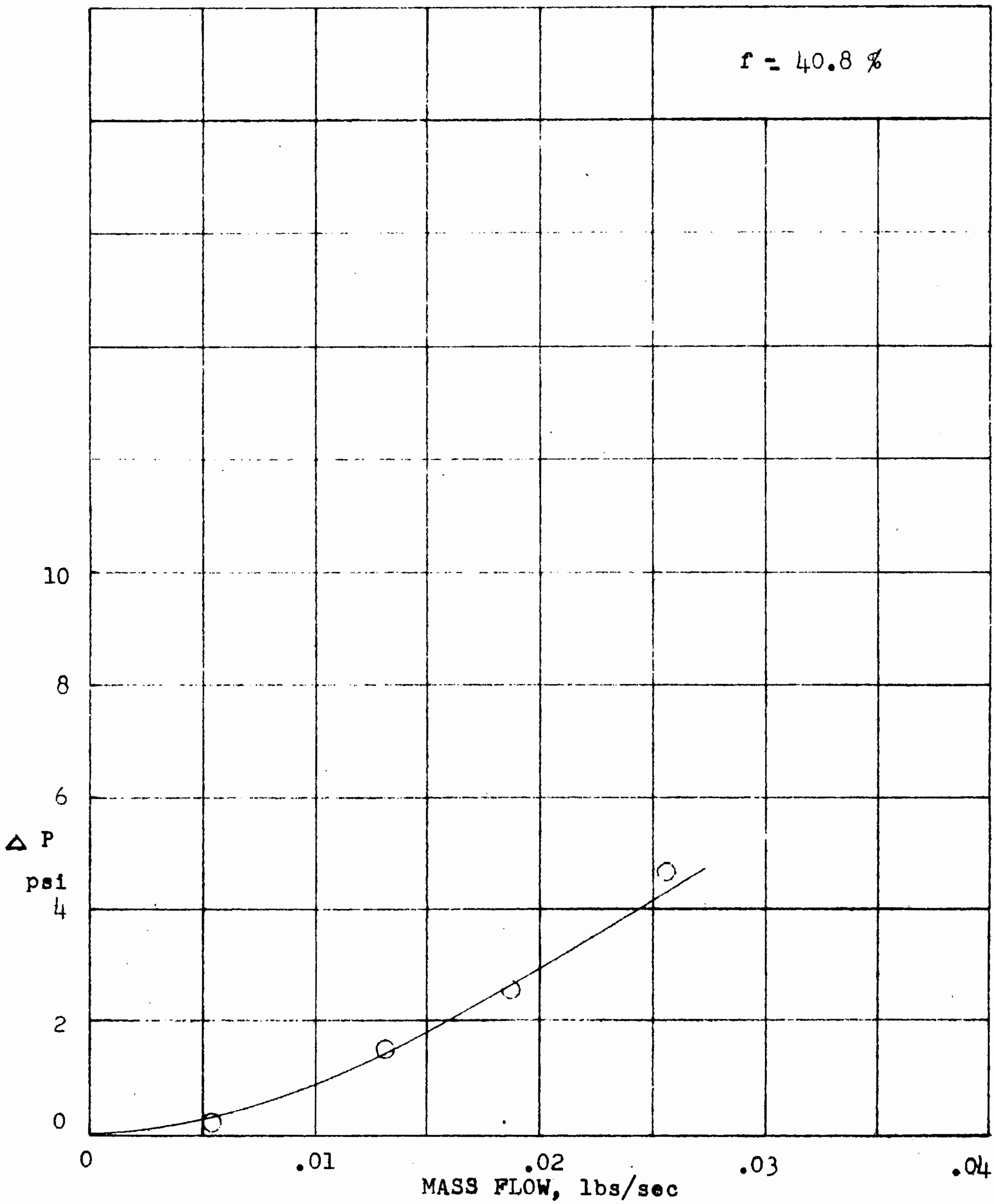

FIGURE 68. PRESSURE DROP AGAINST MASS FLOW